RECOIL DISTANCE METHOD LIFETIME MEASUREMENTS VIA GAMMA-RAY AND CHARGED-PARTICLE SPECTROSCOPY AT NSCL

By

Philip Jonathan Voss

A DISSERTATION

Submitted to
Michigan State University
in partial fulfillment of the requirements
for the degree of

DOCTOR OF PHILOSOPHY

Physics

2011

ABSTRACT

RECOIL DISTANCE METHOD LIFETIME MEASUREMENTS VIA GAMMA-RAY AND CHARGED-PARTICLE SPECTROSCOPY AT NSCL

By

Philip Jonathan Voss

The Recoil Distance Method (RDM) is a well-established technique for measuring lifetimes of electromagnetic transitions. Transition matrix elements derived from the lifetimes provide valuable insight into nuclear structure. Recent RDM investigations at NSCL present a powerful new model-independent tool for the spectroscopy of nuclei with extreme proton-to-neutron ratios that exhibit surprising behavior.

Neutron-rich ^{18}C is one such example, where a small $B(E2; 2_1^+ \rightarrow 0_{gs}^+)$ represented a dramatic shift from the expected inverse relationship between the $B(E2)$ and 2_1^+ excitation energy. To shed light on the nature of this quadrupole excitation, the RDM lifetime technique was applied with the Köln/NSCL plunger. States in ^{18}C were populated by the one-proton knockout reaction of a ^{19}N secondary beam. De-excitation gamma rays were detected with the Segmented Germanium Array in coincidence with reaction residues at the focal plane of the S800 Magnetic Spectrometer. The deduced $B(E2)$ and excitation energy were both well described by *ab initio* no-core shell model calculations.

In addition, a novel extension of RDM lifetime measurements via charged-particle spectroscopy of exotic proton emitters has been investigated. Substituting the reaction residue degrader of the Köln/NSCL plunger with a thin silicon detector permits the study of short-lived nuclei beyond the proton dripline. A proof of concept measurement of the mean lifetime of the two-proton emitter ^{19}Mg was conducted. The results indicated a sub-picosecond lifetime, one order of magnitude smaller than the published results, and validate this new technique for lifetime measurements of charged-particle emitters.

for laura

ACKNOWLEDGMENTS

This work culminates many long years of learning, preparation, frustration, and triumph and has been made possible with the assistance, guidance, and support of many individuals. My humble gratitude extends far beyond this page. If I have completed anything, it is only through Him who gives me strength.

My undergraduate experiences set me on this course. I'd like to thank the many wonderful people in the Central Michigan University Physics Department and Honors Program for all they've done. Fire up Chips! I then was fortunate to continue my education at Michigan State University, where I had the opportunity to learn under the expert instruction of many talented professors. Their commitment to education and excellence in research is inspiring.

I thank my guidance committee members for their collective role in shaping my graduate school career: Dr. B. Alex Brown, Dr. R. Sekhar Chivukula, Dr. David Morrissey, and Dr. Michael Thoennessen. In addition, the listening ear, patient consultation, and critical insight provided by Dr. Hironori Iwasaki and Dr. Thoennessen during my final months were most appreciated. My deepest gratitude goes to my graduate advisor, Dr. Krzysztof Starosta. His tutelage, guidance, and support were instrumental in spurring me forward.

My research would not have been possible without the critical support of many different groups at NSCL. The assistance and dedication of the Computer Group, the Cyclotron Operations Department, and the A1900 Fragment Separator Group was pivotal. Daniel Bazin and Dirk Weisshaar warrant special acknowledgment for their tireless work on the S800 and SeGA. I offer my many thanks to the members of the Gamma Group and collaborators from IKP Köln and LBNL who aided in experimental setup, shift-taking, and analysis discussions.

To the many friends I made—may our common bond forged over late-night study sessions and informal gatherings withstand both time and distance! My gratitude and admiration belongs to Dr. David Miller, the elder half of Team Starosta. Andrew Ratkiewicz deserves much credit for his keen insight as both a draft editor and as one never afraid to offer his opinion and counterpoint. Our discussions over coffee made me a better physicist. I must also thank my fantastic officemates both past and present. “Save Kashy!”

I will always remember my comrades of various enjoyable diversionary ploys. Thanks to the Tuesday Morning Basketball squad and Team Physics softball for slaking my competitive thirst. I am grateful for the gathering of friends on Sunday evenings at our most beloved East Lansing establishment. The Cyclotron DALMAC crew provided many blissful and spandex-clad hours pedaling through the beautiful Michigan countryside. Remember fondly the image of me rising unscathed from the ditch at least once per ride!

I am most indebted to my parents, Jonathan and Deborah Voss, for their constant love, support, and encouragement to walk my own path. The greatest debt of gratitude is owed to my beautiful wife, Laura Jean Voss. You were with me from the beginning of this long process and still are now, even as I write these very words. Your love, immense patience, and companionship helped bring me to this point. Yet our journey is just beginning...

TABLE OF CONTENTS

LIST OF TABLES

LIST OF FIGURES

Chapter 1

Introduction

The complexity of the natural world belies the fact that all tangible aspects of day-to-day life are comprised of fewer than 300 fundamental building blocks. From this relatively small basis, everything from a blade of grass to the tallest skyscraper can be constructed. These stable building blocks, called atoms, consist of a densely packed nuclear core of positively charged protons and chargeless neutrons surrounded by a cloud of negatively charged electrons. The number of protons within a nucleus determines the chemical element; fewer than 100 occur naturally on Earth.

Elements come in distinct varieties, or isotopes, that are differentiated from one another based upon the number of neutrons within the nucleus. From all possible combinations of neutrons and protons, less than 300 are found to be stable. Perhaps a more striking way to phrase this is that of the roughly 7000 [1, 2] possible combinations of protons and neutrons verified or thought to exist, all but approximately 300 undergo spontaneous radioactive decay to achieve a more stable configuration.

The study of the processes responsible for the stability of some isotopes and the radioactivity of the remainder is the fundamental pursuit of nuclear physics. The challenge to discern the properties and behavior of these microscopic objects is daunting. Typical atomic diameters are on the order of angstroms (10^{-10} m), but over 99.9% of the atomic mass resides within the nucleus with a diameter on the order of 10 femtometers (10^{-14} m). A staggering 150 million million (1.5×10^{14}) nuclei stacked one atop another are required to reach the height of an average human. This roughly corresponds to the number of football fields necessary to span the distance between our Sun and the edge of the Solar System.

Yet the current progress is equally impressive. New experimental facilities provide energetic beams of radioactive isotopes that can produce even more exotic nuclei which normally exist only in the most violent of stellar explosions. To study the properties of these exotic nuclei, state-of-the-art techniques and experimental devices have been developed. In addition, the advent of high-power computing has permitted detailed and complex theoretical calculations with ever-increasing predictive power. A small, but meaningful contribution to this progression of knowledge is presented in this work.

1.1 The Nuclear Landscape

The labeling of nuclei follows the notation ${}^{A}Z$, where the number of protons Z determines the element—denoted by a particular chemical symbol—and A is the total number of nucleons. Thus, the number of neutrons follows immediately as $N = A - Z$. A conventional arrangement of nuclei is illustrated in Fig. 1.1. Each isotope is plotted according to its unique combination of neutrons and protons. The stable isotopes comprise the “line of stability”, beyond which exist unstable, or radioactive, nuclei.

Studying the chart of nuclides depicted in Fig. 1.1 illuminates several key observations of nuclear structure. First, as noted above, the overwhelming majority of isotopes are unstable. In addition, the line of stability coincides with $N = Z$ for the lightest nuclei, but tends toward more neutron-rich ($N > Z$) isotopes for heavier systems. There, an excess of neutrons is required to bind the nucleus against the increasing Coulomb repulsive force.

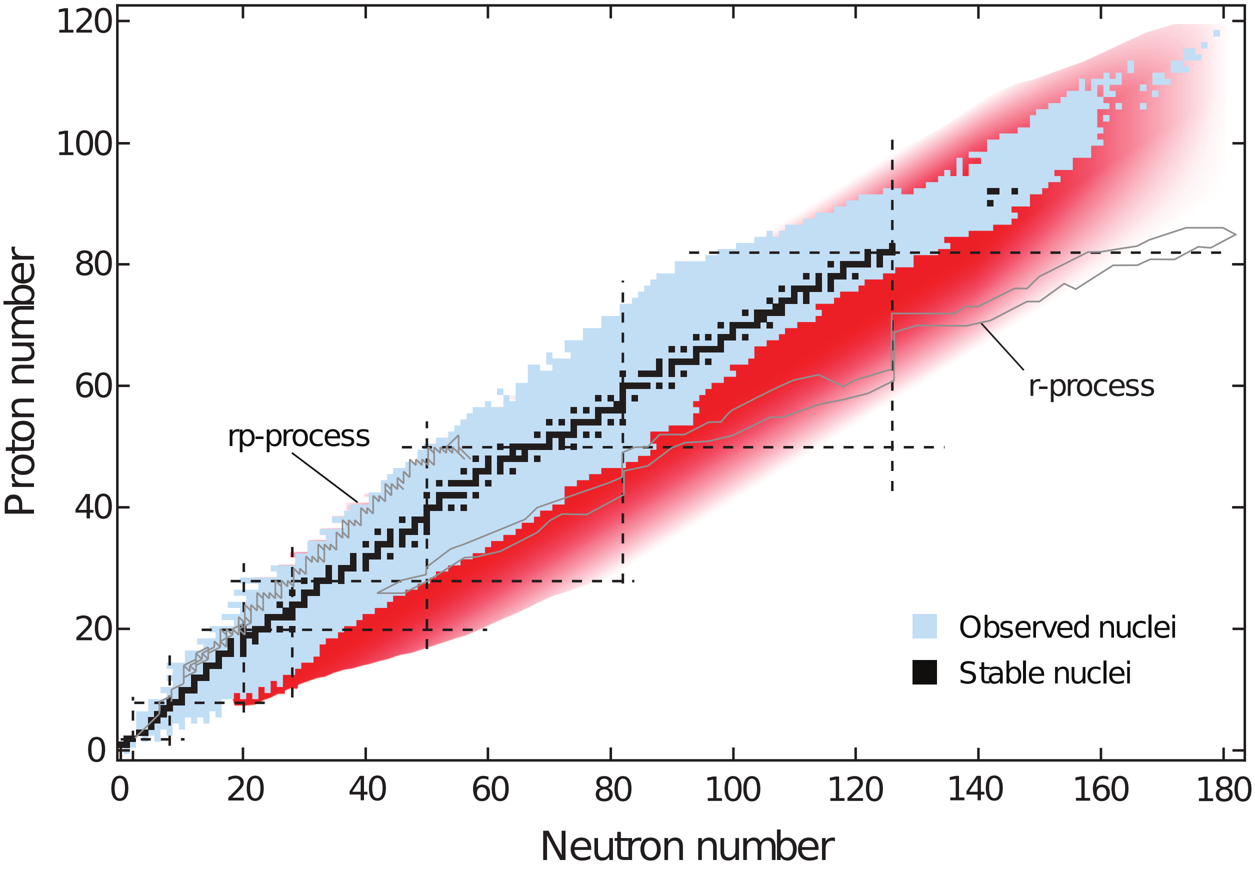

Figure 1.1: The chart of the nuclides with neutron number N along the abscissa and proton number Z along the ordinate taken from [3]. Stable isotopes are indicated with black boxes, observed radioactive nuclei in blue, and predicted unstable nuclei not yet observed in red. The dashed lines indicate magic numbers (see text). Several astrophysical processes are indicated as well. The *rp*-process shall be discussed in Subsect. 1.4.2. For interpretation of the references to color in this and all other figures, the reader is referred to the electronic version of this dissertation.

Most of the unstable isotopes to the left and right of the line of stability are bound systems of protons and neutrons, meaning the nuclear binding energy (Eq. 1.20) is a positive quantity. However, if the nucleus can become *more* bound by the transformation of a neutron into a proton or vice versa, then β^- or β^+ radioactivity may proceed via the weak force. These two decay processes correspond to the emission of an electron or a positron, respectively. Other decay processes such as the emission of a ^{4}He nucleus (α-decay) or the fission of a nucleus into two lighter nuclei are also mechanisms by which binding energy is liberated and more stable configurations are achieved. The production of radioactive isotopes beyond the proton or neutron driplines at the very limits of nuclear existence result in nuclei where the final nucleon is no longer energetically bound to the nucleus. This results in the direct emission of that unbound nucleon. Together, the various modes of radioactive decay transmute unstable nuclei back to the line of stability. Hence, in a sense, nuclear physicists practice modern-day alchemy.

Finally, the vertical and horizontal dashed lines overlayed atop the chart of nuclides in Fig. 1.1 indicate the canonical magic numbers 2, 8, 20, 28, 50 82, and 126, which occur when major nuclear shells (see Subsect. 1.2.1) are filled. Nuclei with magic numbers of protons and/or neutrons generally exhibit especially stable properties, such as increased binding and, relative to neighboring even-even nuclei, an enhanced 2_1^+ excitation energy and low transition probability $B(E2; 2_1^+ \rightarrow 0_{gs}^+)$. However, the study of exotic nuclei has demonstrated both the disappearance of magic numbers and shell gaps [4,5] and the emergence of new ones [6,7] far from stability. The migration of magicity is but one clear indicator that nuclear structure is not a constant; it can evolve dramatically as a function of isospin $T_z = \frac{1}{2}(N - Z)$.

1.2 Nuclear Structure within the Shell Model

Describing how the various facets of nuclear structure, such as stability, energy levels, and transition rates, fundamentally arise from the interactions of individual nucleons is a major goal of nuclear physics. Since the nucleus is an inherently many-body quantum mechanical system, a complete theoretical description for an A nucleon system is akin to the solution of the A-body time-independent Schrödinger equation,

$$\mathcal{H}\Psi = E\Psi. \tag{1.1}$$

The properties of the nucleus are governed by the interplay between the strong, weak, and electromagnetic forces. The exact form of the Hamiltonian $\mathcal{H}$ is not known; instead, accurate nucleon-nucleon and three-body interactions have been developed from both phenomenological and more fundamental approaches. The Argonne v_{18} [8] and CD-Bonn [9] potentials are examples of the former approach and are derived from accurate reproduction of nucleon-nucleon scattering data. Interactions derived from chiral effective field theory calculations belong to the latter approach [10]. Nuclear theoretical models built upon these realistic two- and three-body interactions successfully calculate various nuclear properties. However, calculations quickly become computationally intractable and thus approximations and truncations must be made.

In the standard shell model [11], the solution of Eq. 1.1 is simplified by splitting the nucleus into an inert core and valence nucleons. The core, typically a nearby doubly-magic nucleus, has fully-occupied single-particle levels and is treated as non-interacting. The implicit assumption is that all nuclear structure properties can be derived entirely with the valence proton and neutron particles or holes. The allowable excitations of the valence nucleons must also be truncated to abet the calculations. Together, these two simplifications preclude interactions between the core and valence particles and restrict the allowable excitations. Therefore an effective interaction must be derived from the realistic two- or three-body interactions above to account for the truncated model space.

The no-core shell model [12] (NCSM) approach expands upon this, breaking the core and including all nucleons within the calculation. Therefore, in principle, the full A-body problem can be solved with this *ab initio* approach. However, truncations on allowable excitations still must be made in the NCSM and therefore effective interactions are again required. To obtain the full model space solution, extrapolation methods are used. Extending this method to heavier nuclei is challenging. Accurate experimental data of exotic isotopes can provide important benchmark tests. The lifetime measurements of electromagnetic transitions in ^{18}C presented in Ch. 3 fulfill this role; a comparison between experiment and theory is provided in Ch. 5. In preparation, a discussion of the *ab initio* NCSM is provided below, but first a brief description of shell structure nomenclature is provided. A familiarization with terms will be useful for a shell model discussion in Subsect. 5.1.1.

1.2.1 Nuclear Shell Structure

Nucleons have an intrinsic spin $s = \frac{1}{2}\hbar$ and an orbital angular momentum $\ell = 0, 1, 2, 3, \ldots$ that is labeled spectroscopically as $s, p, d, f, \ldots$ respectively. The spin and orbital angular momentum couple to the total angular momentum $j = \ell \pm s$. Hence a complete description of the single-particle shell model orbital for a nucleon is given by $\sigma n \ell_j$, where σ denotes the type of nucleon (π for protons and ν for neutrons) and $n = 0, 1, 2, 3, \ldots$ is the principle quantum number. Nucleons obey Fermi-Dirac statistics; no two nucleons can occupy the same orbital. Rather each orbital can accommodate $2j + 1$ nucleons in different magnetic substates. Pairs of nucleons in a given j state couple to spin 0 and thus even-even nuclei have a ground state spin/parity 0^+. In contrast, odd-A nuclei have ground state spins typically determined by the unpaired nucleon.

1.2.2 *Ab Initio* No-Core Shell Model

The goal of NCSM calculations is to solve the full A-body quantum mechanical problem using realistic two- and three-body interactions such as those mentioned above [13]. A brief primer to the method is given in Ref. [14]. The NCSM model space is typically spanned by Slater determinants constructed with single-particle harmonic-oscillator (HO) basis states. The spacing between energy levels is denoted by the HO frequency $\hbar\Omega$. The model space is restricted to a maximum number of harmonic-oscillator excitations N_{max} such that all Slater determinants with an energy less than $N_{max}\hbar\Omega$ are included within the calculation.

Effective interactions are used to account for effects of configurations outside of this finite model space [12].

The use of effective interactions reproduces a subset of eigenvalues from the original two- or three-body interactions. Therefore as the model space approaches the full space ($N_{max} \to \infty$), the approximate solution approaches the exact solution of the original full interaction [13]. This convergence implies that calculations performed over several $N_{max}\hbar\Omega$ cutoffs will tend towards the full model space result and more importantly, calculations of N_{max} sequences for various $\hbar\Omega$ all must converge to the same result. The existence of a common solution for various pathways provides an asymptotic constraint for the extrapolation to the full space result.

The *ab initio* NCSM therefore provides an approach by which exact solutions of an A-body quantum mechanical problem using a realistic Hamiltonian can be obtained. The method has been successfully applied to p-shell nuclei [14], however computational limits hinder calculations for nuclei beyond $A = 16$ with sufficient N_{max} to attain accurate extrapolations. For instance, the current limit for ^{18}C calculations is $N_{max} = 6$ [15] and that of ^{16}O is $N_{max} = 8$ [16]. In these cases, reliable convergence may not be computationally tractable.

To ameliorate this, a recent extension of NCSM calculations uses the importance truncation (IT) scheme [16,17]. With this approach, a measure of the importance of individual HO basis states via perturbation theory precedes the calculation [17]. Many states contribute to a calculation with vanishingly small amplitudes; the elimination of these unimportant basis states truncates the model space while preserving the physically relevant basis states. This reduces the computational intensity and thus permits calculations to higher N_{max}, improving the accuracy of the extrapolation to the full model space result [16]. For example, IT-NCSM calculations have permitted calculations of the ground state energy of ^{16}O to $N_{max} = 22$ [16] and, as will be shown in Ch. 5, excited state properties of ^{18}C to $N_{max} = 8$.

1.3 Nucleon Knockout from Radioactive Beams

The emerging importance of powerful theoretical approaches that derive nuclear properties from the fundamental interactions of all nucleons, such as the *ab initio* NCSM, benefits from comparison to precise experimental measurements at the extremes of isospin. Such data is readily obtained with nucleon knockout reactions of radioactive beams. This technique has provided the greatest reach from the line of stability; two examples of such measurements shall be introduced in Ch. 3 and 4. Neither analyses are reaction-model dependent, therefore a brief introduction to nucleon knockout reactions will suffice.

The first step involves the production of an energetic radioactive ion beam. Two main techniques exist. The in-flight production and selection of radioactive beams is employed at NSCL and shall be described in detail in Sect. 2.2. The isotope separation on-line method is a complementary technique employed, for example, at HRIBF at ORNL and TRIUMF in Canada. There, high-energy stable beams (such as protons) impinge upon a thick production target. The subsequent spallation or fission of the target nuclei produce a variety of radioactive isotopes which upon extraction, ionization, and purification are accelerated to the experimental station.

Delivery of radioactive ion beams to experimental targets and the subsequent single-nucleon knockout reaction is a powerful spectroscopy tool for nuclear structure studies. For instance, the extraction of partial cross sections via gamma-ray tagging of final states can be used to calculate spectroscopic factors which can help infer information about the occupation of shell model single-particle orbitals [18]. For the present work, single-nucleon knockout reactions provide a simple production mechanism by which exotic nuclei can be produced and which can be well quantified within the framework of the analysis.

Single-nucleon knockout reactions are peripheral processes where a nucleon residing near the nuclear surface is removed from the incident secondary beam (of mass $A + 1$) by a light target, such as beryllium or carbon. The resulting reaction residue (of mass A and often in an excited state) emerges from the target with nearly the same velocity as that of the incoming beam [19]. Within the target, two distinct mechanisms are responsible for the removal of the nucleon [18]. In stripping reactions the energy of the removed nucleon is absorbed by the target and produces excited target states while the competing diffractive breakup involves nucleon removal mediated by scattering off a target nucleus. If, as in the studies of Ch. 3 and 4, only the heavy-ion reaction residue is observed, the total single-particle knockout cross section can be approximated by the sum of these two components. The relative contribution of each mechanism is of little consequence for the present works.[1]

The energetic beams produced at NSCL are ideal for studies involving nucleon removal from exotic beams. In particular, they permit the use of thick targets which enhance experimental luminosities despite low secondary beam rates and knockout cross sections. In addition, the energetic residues are strongly kinematically forward-focused in the laboratory frame, preventing significant acceptance loss issues within tracking detectors [23]. This ensures that event-by-event particle tagging can proceed to produce high signal-to-noise spectra. These features were imperative for the lifetime measurements reported in this work.

1.4 Köln/NSCL Plunger Lifetime Measurements

The direct one-proton knockout reaction of an intermediate energy radioactive ^{19}N secondary beam at NSCL populated excited states in ^{18}C. After the reaction, the de-excitation gamma radiation was observed with the Segmented Germanium Array. Via the Recoil Distance Method (RDM) with the Köln/NSCL plunger, the lifetime of the $2_1^+ \rightarrow 0_{gs}^+$ electric quadrupole transition was measured. In addition, a lifetime upper limit was extracted for a

---

[1] Lifetime measurements of electromagnetic transitions similar to that reported in Ch. 3 do not explicitly require nucleon knockout reactions for excited-state production; Coulomb excitation on heavier targets has been effectively used as well [20–22].

higher-lying excited state feeding the 2_1^+ state. The importance of lifetime studies such as these to the basic understanding of the nucleus is introduced in Subsect. 1.4.1. The experimental technique and devices are introduced in Ch. 2, while a detailed discussion of the data and analysis is found in Ch. 3. The results and comparisons to theoretical calculations are presented in Ch. 5.

A modified Köln/NSCL plunger was utilized for the two-proton decay lifetime measurement of ^{19}Mg. This exotic proton emitter was produced by the one-neutron knockout reaction of a ^{20}Mg secondary beam on a carbon plunger target. A thin silicon detector mounted downstream of the target recorded the energy loss signature of reaction and heavy-ion decay residues. From these energy loss spectra, the ^{19}Mg ground state two-proton decay lifetime was measured. The measurement served as a proof of concept for "particle plunger" RDM lifetime measurements which may prove especially important for nuclear astrophysics calculations in the proton-rich region of the nuclear landscape. This importance is expanded upon in Subsect. 1.4.2. The specific details of the technique are provided in Ch. 2 and the data and analysis are presented in Ch. 4. The results are discussed and compared to the previous measurement, and subjects for future investigation are given in Ch. 5.

1.4.1 Lifetime Measurements of Electromagnetic Transitions

RDM lifetime measurements provide a non-intrusive and model-independent probe by which the detection of electromagnetic radiation elucidates information on the nuclear charge distribution. Such an electromagnetic probe is desirable as it only weakly perturbs the system—nucleon motion is governed by the strong force which dominates the electromagnetic force at such short distances. Furthermore, the technique is versatile; any excited state population mechanism can be used with RDM measurements to probe nuclear charge and current distributions without destroying the state of the system. This method is entirely complimentary to hadron inelastic scattering probes which deduce information on nuclear matter distributions. Thus the study of electromagnetic transitions is key to understanding the nucleus and can provide stringent tests of various and sometimes competing theoretical nuclear structure calculations.

The nuclear electric and magnetic fields are produced by the distribution of charges and currents within the nucleus. The multipole expansion of these fields separates the contributions of individual multipole moments based upon their characteristic radial dependence (r^x). For instance, the electric monopole moment is just the $1/r^2$ field due to the net charge. The $1/r^3$ and $1/r^4$ electric fields are the dipole and quadrupole moments, respectively. The magnetic field multipoles behave in a similar fashion except that the monopole moment vanishes as no individual magnetic charges have been found in nature. The first non-vanishing term is the $1/r^3$ magnetic dipole moment and arises from electric current moving in a circular loop.

Therefore measuring the various electromagnetic moments of a nucleus tells us about the distribution of the nuclear charge and current. In particular, the detection of electric quadrupole ($E2$) radiation in even-even nuclei probes the collective structure of nuclear excitations. In a collective picture, the coherent behavior of all nucleons collectively influences nuclear structure. The degree of this collective behavior is quantified by the reduced transition probability matrix element $B(E2)$. This important experimental measurement is directly obtained from lifetime measurements of $E2$ transitions.

The following discussion reflects, in a simplified manner, the spirit of the nuclear structure texts of Ref. [24, 25]. The extent to which the charge distribution of a nuclear state $|A\rangle$ deviates from spherical symmetry is given by the static quadrupole moment

$$eQ = \langle A| \, \mathcal{M}_{E2} \, |A\rangle, \tag{1.2}$$

where $\mathcal{M}_{E2}$ is the electric quadrupole operator. eQ thus represents the diagonal elements of the matrix linking all possible initial and final quantum mechanical states via the more general electric quadrupole tensor operator, $\mathcal{M}_{E2,\mu}$. The non-diagonal elements represent $E2$ transitions between different states; studying these transitions sheds light on the quadrupole deformation of the nuclear charge distribution.

Mathematical Formulation

Electromagnetic nuclear decays are spontaneous photon emissions via the interaction of a nucleus with an external electromagnetic field and are mediated by the four vector $(\phi, \mathbf{A})$. The scaler and vector potentials, ϕ and $\mathbf{A}$, couple to the nuclear charge density ρ and current density $\mathbf{j}$, respectively. The expansion of the scaler field for a collection of A particles into a summation of electric multipoles yields

$$\phi(\mathbf{r}) = \sum_{j}^{A} \frac{e_j}{|\mathbf{r} - \mathbf{r}'_j|} = \sum_{\lambda\mu} \frac{4\pi}{2\lambda+1} \frac{1}{r^{\lambda+1}} Y^*_{\lambda\mu}(\Omega)\mathcal{M}_{E\lambda,\mu} \tag{1.3}$$

where the electric multipole moment $\mathcal{M}_{E\lambda,\mu}$ is a spherical tensor of multipolarity λ and is given by

$$\mathcal{M}_{E\lambda,\mu} = \sum_{j}^{A} e_j r_j^{\lambda} Y_{\lambda\mu}(\Omega_j). \tag{1.4}$$

In a similar manner, the magnetic multipole moment of multipolarity λ is given by

$$\mathcal{M}_{M\lambda,\mu} = \sum_{j}^{A} \left[g_j^s \mathbf{s}_j + \frac{2}{\lambda+1} g_j^l \mathbf{l}_j \right] \cdot \nabla \left[r_j^{\lambda} Y_{\lambda\mu}(\Omega_j) \right]. \tag{1.5}$$

In Eq. 1.3, 1.4, and 1.5, $Y_{\lambda\mu}(\Omega)$ are spherical harmonics of multipolarity λ with projection $\mu = -\lambda, -\lambda+1, \ldots, \lambda-1, \lambda$ and Ω_j, e_j, $g_j^{s,l}$, and $\mathbf{s}_j$ and $\mathbf{l}_j$ represent the coordinates on the unit sphere (θ, ϕ), the electric charge, the spin and orbital gyromagnetic ratios, and angular momentum operators of the j^{th} nucleon, respectively.

These electromagnetic multipoles act as quantum mechanical tensor operators on states in a nucleus. Considering the simple case of a system containing a nucleus in an external electromagnetic field, the initial state $|i\rangle$ can be represented by the nucleus in its excited state and the photon vacuum electromagnetic field. The final state $|f\rangle$ is thus the nucleus in its ground state with one photon of energy E_γ in the electromagnetic field. The transition between these two states is described by one or more of the above multipoles with the appropriate selection rules (discussed in Appendix A). The interaction between the nucleus and electromagnetic field is weak and thus a perturbative treatment of the decay yields the transition probability per unit time

$$\begin{aligned} T_{fi}^{\sigma\lambda\mu} &= \frac{2}{\epsilon_0 \hbar} \frac{\lambda+1}{\lambda[(2\lambda+1)!!]^2} \left(\frac{E_\gamma}{\hbar c}\right)^{2\lambda+1} \left|\langle f|\,\mathcal{M}_{\sigma\lambda,\mu}\,|i\rangle\right|^2 \\ &\equiv \kappa \left|\langle f|\,\mathcal{M}_{\sigma\lambda,\mu}\,|i\rangle\right|^2 . \end{aligned} \tag{1.6}$$

Here, σ, λ, and μ denote the electric or magnetic character of the multipole, the multipolarity, and the projection, respectively. The initial and final states are characterized by their respective quantum numbers such that for a state a, $|a\rangle = |\xi_a, J_a, M_a\rangle$ where J_a and M_a are the total angular momentum and angular momentum projection of the state and ξ_a are the remaining quantum numbers necessary to describe the state.

For the present work, the initial and final magnetic substates are not measured. Thus averaging over the initial substates M_i and summing over the final substates M_f and all multipolarity projections μ leads to the new expression

$$\begin{aligned} T_{fi}^{\sigma\lambda} &= \frac{1}{2J_i+1} \sum_{M_i M_f \mu} T_{fi}^{\sigma\lambda\mu} \\ &\equiv \kappa B(\sigma\lambda; \xi_i J_i \to \xi_f J_f), \end{aligned} \tag{1.7}$$

where $B(\sigma\lambda; \xi_i J_i \rightarrow \xi_f J_f)$ is the reduced transition probability given by

$$B(\sigma\lambda; \xi_i J_i \rightarrow \xi_f J_f) \equiv \frac{1}{2J_i + 1} |\langle \xi_f J_f || \mathcal{M}_{\sigma\lambda} || \xi_i J_i \rangle|^2. \tag{1.8}$$

The reduced transition probability arises from the application of the Wigner-Eckart Theorem. The derivation is beyond the scope of this work; it is sufficient to note that the theorem reduces the original matrix element to a form independent of the projection quantum numbers while retaining the physical information to be extracted from the observable. The dependence of the matrix element on the magnetic projection numbers are concentrated into Clebsch-Gordan coefficients.

For the $2_1^+ \rightarrow 0_{gs}^+$ transition in ^{18}C, the $E2$ gamma ray is the experimental observable from which the lifetime is extracted. From this lifetime, the value of the reduced quadrupole transition strength $B(E2; 2_1^+ \rightarrow 0_{gs}^+)$ can be calculated by the inverse relationship between the lifetime and transition rate of Eq. 1.7

$$\begin{aligned} \tau(2_1^+ \rightarrow 0_{gs}^+) &= \frac{1}{T_{2_1^+ \rightarrow 0_{gs}^+}} \\ &= \left[\frac{1}{75\epsilon_0 \hbar} \left(\frac{E_\gamma}{\hbar c} \right)^5 B(E2; 2_1^+ \rightarrow 0_{gs}^+) \right]^{-1}. \end{aligned} \tag{1.9}$$

Quantifying Nuclear Collectivity

Equation 1.9 provides the link between the experimentally measured lifetime and the reduced quadrupole transition strength. This $B(E2)$ value is a model-independent measure of the degree of quadrupole collectivity in even-even nuclei. In particular, it can be associated with nuclear shape deformation.

Following the liquid drop model, the quadrupole deformation of the nuclear radius about the average value R_0 is given by

$$R(\Omega) = R_0 \left[1 + \sum_{\mu} \alpha_{2,\mu} Y_{2,\mu}(\Omega) \right], \tag{1.10}$$

where $\alpha_{2,\mu}$ are shape variables describing the deformation of the nucleus. If the laboratory-fixed coordinate system is arbitrarily rotated by some choice of angles $\Omega' = (\theta', \phi')$, the intrinsic nuclear shape does not change. All that changes is how the shape is oriented with respect to the new set of coordinates. In particular, the original spherical function $Y_{2,\mu}(\Omega)$ will form new combinations of $Y_{2,\mu}(\Omega')$ with new coefficients $\alpha'_{2,\mu}$. Since neither the shape nor the experimental observable changes by this coordinate rotation, it is convenient to work in a body-fixed coordinate system where the symmetry axis of the nucleus forms one of the major coordinate axes. In this body-fixed frame, the quadrupole deformation of the nuclear radius is expressed in a similar manner to Eq. 1.10,

$$R(\Omega') = R_0 \left[1 + \sum_{\mu} a_{2,\mu} Y_{2,\mu}(\Omega') \right], \tag{1.11}$$

where the new deformation shape variables $a_{2,\mu}$ are linear combinations of the original variables $\alpha_{2,\mu}$ with coefficients reflecting the rotational angles from the laboratory-fixed to body-fixed frames. Inserting the expressions for the $\lambda = 2$ spherical harmonics, the deformation then becomes

$$\begin{aligned} \frac{R(\Omega') - R_0}{R_0 \sqrt{\frac{5}{4\pi}}} &= a_{2,0} \left(\frac{3}{2} \cos^2 \theta' - \frac{1}{2} \right) \\ &+ \sqrt{\frac{3}{2}} \sin \theta' \cos \theta' \left(a_{2,-1} e^{-i\phi'} - a_{2,1} e^{i\phi'} \right) \\ &+ \sqrt{\frac{3}{8}} \sin^2 \theta' \left(a_{2,2} e^{2i\phi'} + a_{2,-2} e^{-2i\phi'} \right). \end{aligned} \tag{1.12}$$

Since the nuclear shape is invariant under coordinate rotations, it is reasonable to expect the 5 deformation shape variables ($a_{2,\mu}$ for $\mu = -2, -1, 0, 1, 2$) can be reduced to 2 invariant shape variables. Indeed, in the body-fixed frame the reflection about the equatorial plane changes the polar angle from θ' to $\pi - \theta'$ while leaving ϕ' unchanged. Thus $\cos\theta'$ switches sign and to preserve the invariance of the deformation about this symmetry reflection,

$$a_{2,1} = a_{2,-1} = 0. \tag{1.13}$$

Furthermore, reflection about the vertical plane changes the azimuthal angle from ϕ' to $-\phi'$ while leaving θ' unchanged. Such a reflection will switch the $a_{2,2}$ and $a_{2,-2}$ terms in Eq. 1.12 and thus keeping the shape invariant under this symmetry reflection requires

$$a_{2,2} = a_{2,-2}. \tag{1.14}$$

Hence two invariant shape variables remain: $a_{2,0}$ and $a_{2,2}$. These are commonly expressed by the deformation parameter β and the non-axiality parameter γ (which quantifies the departure from cylindrical symmetry) as

$$a_{2,0} = \beta \cos\gamma, \quad a_{2,2} = \frac{1}{\sqrt{2}}\beta \sin\gamma. \tag{1.15}$$

The deformation parameter β quantifies the departure from nuclear sphericity. For the limiting case of a rotating ellipsoid (with axial symmetry), it can be directly related to the measured $B(E2)$ value with the additional assumptions that the deformation is both small in magnitude and static (without vibration).

$$B(E2; 2_1^+ \rightarrow 0_{gs}^+) = \frac{1}{5}\left[\frac{3}{4\pi} Z e R_0^2 \beta\right]^2. \tag{1.16}$$

Final Remarks

The preceding discussion illuminates the important role of lifetime measurements in quantifying nuclear collectivity. The reduced quadrupole transition strength is inversely proportional to the measured lifetime and from the $B(E2)$ value, the degree of nuclear deformation can be quantified. A customary way to indicate this is the ratio between the experimental $B(E2)$ value and the single-particle estimate,

$$B(E2)/B_W(E2). \tag{1.17}$$

Here, the single-particle transition strength estimate $B_W(E2)$ is taken from Eq. A.3. A large value for this ratio (∼10) indicates collective behavior while a value much closer to unity suggests behavior associated with closed-shell nuclei, such as doubly-magic ^{16}O, ^{40}Ca, and ^{48}Ca which all have ratios of roughly 3 or smaller.

On a final note, an empirical approach within the liquid drop model to quantify global $B(E2)$ systematic trends for even-even nuclei [26] has found

$$E(2_1^+) \cdot B(E2; 2_1^+ \rightarrow 0_{gs}^+) \propto Z^2 A^{-2/3}. \tag{1.18}$$

Hence the general expectation is that the $B(E2)$ will be inversely proportional to the 2_1^+ excitation energy. For neutron-rich carbon isotopes, the 2_1^+ excitation energy of the $N = 8$ nucleus ^{14}C drops dramatically from approximately 7.0 MeV to 1.8 and 1.6 MeV for ^{16}C and ^{18}C, respectively. Accordingly, the $B(E2)$ for ^{16,18}C is expected to be much larger than the ^{14}C value of 3.74 e^{2}fm^4 [27]. However, as reported in Ref. [28, 29] and later in Ch. 3, the $B(E2)$ values are observed to remain relatively constant with that of ^{14}C. This deviation from systematic behavior may indicate a shift in quadrupole excitation mechanisms and illustrates the particular importance of lifetime measurements for probing nuclear behavior

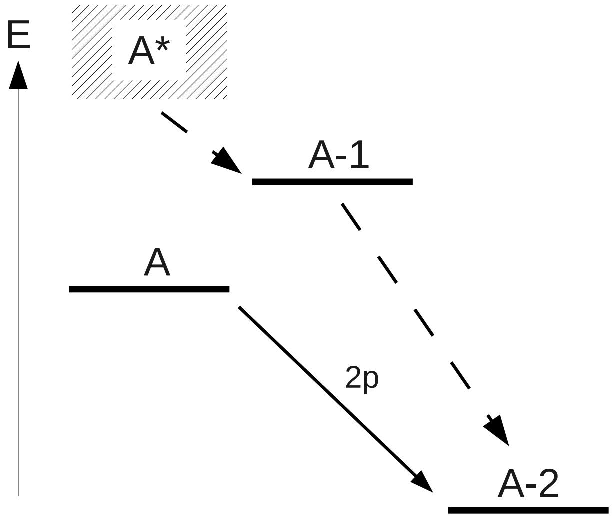

Figure 1.2: The pairing contribution to the nuclear binding energy lowers the ground state energy of the two-proton emitter $A = (Z, N)$ with respect to that of the $(Z-1, N)$ system. Thus the nucleus decays via simultaneous $2p$ emission (solid arrow) directly to the ground state of the $(Z-2, N)$ daughter. Sequential $1p$ emissions (dashed arrows) via the unbound intermediary $(Z-1, N)$ daughter is possible from resonances within the continuum of the parent $(Z, N)^*$.

rather than relying solely upon energy systematics from in-beam gamma-ray spectroscopy.

1.4.2 Lifetime Measurements of Proton Radioactivity

The simultaneous emission of two protons is the most recently discovered nuclear decay mechanism. This exotic decay mode was first discussed in the seminal work of Ref. [30]. Two-proton radioactivity only exists for even-Z nuclei where nuclear pairing of the valence protons energetically prevents single-proton emission. Though the parent is bound to $1p$ decay, it is unbound to $2p$ decay because of the symmetry energy and Coulomb interaction [31]. A schematic of this scenario is presented in Fig. 1.2. True two-proton emission must also proceed from narrow nuclear ground states; broad resonant states of neighboring nuclei beyond the dripline can overlap, resulting in an ambiguity between simultaneous $2p$ decay and sequential $1p$ emissions.

Likely candidates for two-proton radioactivity were theoretically identified between $26 \leq$

$Z \leq 36$, where the Coulomb barrier would yield narrow ground states decaying with observable lifetimes [32, 33]. Two-proton radioactivity was later measured and confirmed for ^{45}Fe [34–36] and ^{54}Zn [37]. These measurements yielded lifetimes of several milliseconds, well within the reach of implantation-type experiments [37] or the optical time projection chamber method [36].

In contrast, the lower Coulomb and centrifugal barriers of lighter elements result in much faster proton radioactivity. Indeed, a lifetime on the order of picoseconds was reported in Ref. [38] for the two-proton decay of the ^{19}Mg ground state. The result was found to be in agreement with quantum mechanical calculations treating the $2p$-decay precursor as a three-body composite of two independent protons and a ^{17}Ne core [39]. Such experimental verification is important because simpler lifetime calculations, based upon a semi-classical treatment of a tunneling diproton (^{2}He nucleus), predicted lifetimes much shorter than those experimentally measured as discussed in Ref. [35, 40].

The fast proton radioactivity of ^{19}Mg provides an ideal testing ground for a new lifetime measurement technique for proton emitters beyond the dripline. The technique is based upon the well-established Recoil Distance Method; details are given within Ch. 2 while the data and analysis are presented in Ch. 4. This proof of concept experiment yielded an independent lifetime measurement of ground state proton emission in ^{19}Mg. The method complements the other established techniques for lifetime studies at the proton dripline [36–38,41] and affords sensitivity for precision lifetime measurements of both $1p$ and $2p$ decays in the picoseconds range. These studies, interesting in their own right, are also of interest for nuclear astrophysics. Proton decay is the inverse reaction of radiative proton capture; such processes play a vital role in galactic proton-rich nucleosynthesis. Furthermore, as the following discussion illustrates, the proton-decay lifetimes can provide important constraints on mass models and proton-capture rates vital to the stellar isotopic synthesis calculations.

Importance for Nuclear Astrophysics

If the heaviest isotopes to exist in nature belonged to the iron group ($A \approx 56$), our knowledge of stellar nucleosynthesis would be nearly complete. Hydrogen core burning via the pp-chains and CNO cycles produces an abundance of helium. After the hydrogen is exhausted, helium burning commences via the triple alpha process. Once the helium is exhausted, the burning proceeds more and more rapidly through carbon, neon, oxygen, and finally silicon. Here nucleosynthesis ends as the resulting iron group nuclei are the most tightly bound in nature and further fusion reactions are generally endothermic. References [42] and [43] provide a detailed overview of these processes.

Yet the existence of the stable isotopes from iron to uranium has spurred the development of a small arsenal of nucleosynthesis processes complimentary to stellar burning. Among these are the slow and rapid neutron capture processes and the proton capture process. These three, first postulated in the late 1950s [44], are responsible for the stellar production of almost all stable isotopes beyond iron.

Several well-documented instances where nucleosynthesis calculations underproduce specific nuclei with respect to solar abundances may indicate the need for even more processes. Such a suggestion was prompted by the underproduction of ^{92,94}Mo and ^{96,98}Ru [45] and several isotopes of Sr, Y, and Zr [46]. An attractive mechanism to ameliorate this underproduction was the neutrino p-process [47]. Occurring in the neutrino-/antineutrino-rich environment of Type II core-collapse supernovae, the νp-process initially drives supernovae ejecta proton rich by neutrino capture $\nu_e + n \rightarrow p + e^-$. This facilitates the production of proton-rich isotopes via (p, γ) reactions in a manner identical to the rp-process [48, 49]. In later stages, the reaction flow stalls at waiting-point nuclei (such as ^{64}Ge, ^{68}Se, and ^{72}Kr) due to a combination of long β^+ decay half-lives and small proton-capture rates. To produce heavier nuclei, these waiting points must be bridged. This is accomplished with (n, p) reactions in the νp-process, where antineutrino capture on the proton-rich ejecta, $\bar{\nu_e} + p \rightarrow n + e^+$, increases

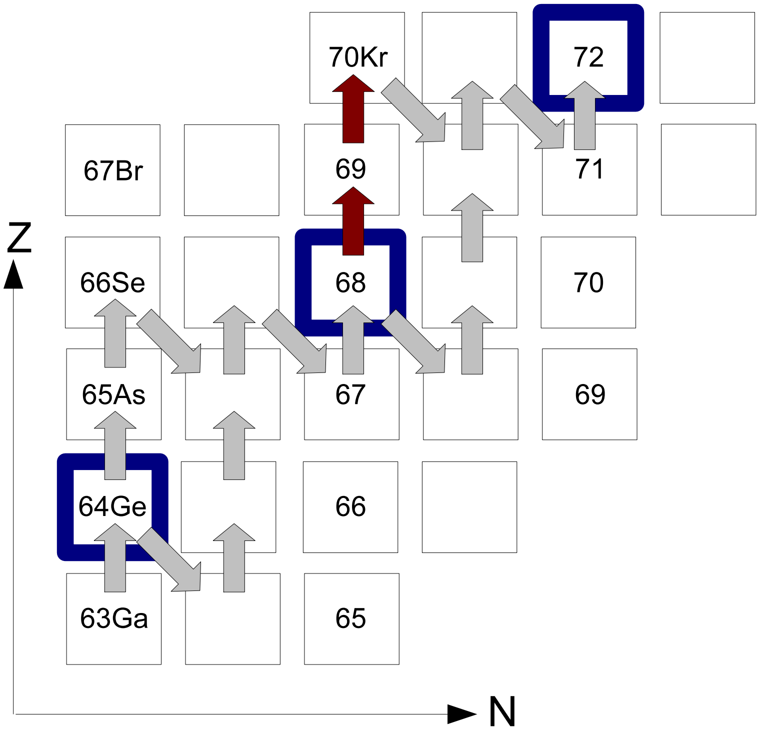

Figure 1.3: Reaction flow of the *rp*-process for a portion of the nuclear chart during a Type I x-ray burst. Reaction flows indicating proton captures and β^+ decays (gray arrows) were taken from Fig. 1 of Ref. [51]. The red arrows indicate the possible two-proton capture of ^{68}Se which may bridge this long-lived waiting point.

the abundance of free neutrons. The waiting points can be bypassed in the *rp*-process via $(2p, \gamma)$ reactions which effectively jump over the unbound $(Z + 1)$ isotone [49, 50]. Figure 1.3 illustrates a small portion of the *rp*-process reaction flow and the possible importance of two-proton capture in bridging waiting-point nuclei.

The role of the νp-process in galactic chemical evolution and its uniqueness from the *rp*-process in explosive environments ultimately depends upon the models' success of reproducing observed abundances [52,53]. Both calculations involve proton-capture rates that are sensitive to temperature, density, composition, and (most critically) masses [49, 53]. From the masses, one- and two-proton separation energies (S_p and S_{2p}) can be calculated; their importance in nucleosynthesis calculations is illustrated in the following brief derivation.

Mathematical Formulation

For simplicity, consider the one-proton capture reaction between two nuclei,

$$1 + p \to 2 + \gamma. \tag{1.19}$$

The binding energy can be calculated directly if nuclear masses are known via

$$B(Z, N) = \left(Zm_p + Nm_n - m_{nuc}\right) c^2. \tag{1.20}$$

After setting the speed of light to unity, the binding energy difference between the two nuclei is given by

$$\begin{aligned} B(Z+1, N) - B(Z, N) &= \left((Z+1)m_p + Nm_n - m_2\right) - \left(Zm_p + Nm_n - m_1\right) \\ &= m_p + m_1 - m_2. \end{aligned} \tag{1.21}$$

This is simply the Q-value of the reaction and corresponds to the energy of the photon in Eq. 1.19. If instead a photon of that same energy impinges upon nucleus 2, the reverse reaction of Eq. 1.19 would occur. Thus the Q-value is equal in magnitude, but opposite in sign, to the one-proton separation energy ($Q = -S_p$).

The proton-capture cross section σ (in units of area) is given by

$$\sigma = \frac{\mathcal{N}/t}{[N_p/(t \cdot A)]N_1}. \tag{1.22}$$

The numerator is the number of reactions per time and the denominator contains the proton current density $j_p = N_p/(t \cdot A)$ and number of target nuclei N_1. Rearrangement yields an expression for the number of capture reactions per unit volume and time,

$$\frac{\mathcal{N}}{V \cdot t} = \sigma N_1 \frac{N_p}{V \cdot A \cdot t} = \sigma(v) v \frac{N_1}{V} \frac{N_p}{V}. \tag{1.23}$$

Here, the velocity dependence of the cross section has been introduced. In the stellar environment, the protons and target nuclei have some distribution of relative velocities. This distribution can be described by the probability function $P(v)$ such that $P(v)dv$ is the probability that the relative velocity is between v and $v + dv$. After absorbing the volume terms into N_i, which should now be understood to be number densities, the reaction rate can be expressed as

$$r \equiv N_1 N_p \int_0^\infty \sigma(v) v P(v) dv \equiv N_1 N_p \langle \sigma v \rangle . \tag{1.24}$$

The reaction rate per particle pair, $\langle \sigma v \rangle$, contains the nuclear physics information and in most cases can be calculated assuming a Maxwell-Boltzmann velocity distribution.

With the help of Eq. 1.24, the destruction rate of the target nucleus can be written as

$$\begin{aligned} \frac{dN_1}{dt} &= -r = -N_1 N_p \langle \sigma v \rangle \\ &\equiv -\lambda_p N_1. \end{aligned} \tag{1.25}$$

The establishment of local equilibrium between the proton-capture (with decay constant λ_p) and photodisintegration (with decay constant λ_γ) implies

$$\begin{aligned} 0 &= r_{1+p\rightarrow 2+\gamma} - r_{2+\gamma\rightarrow 1+p} \\ &= N_1 N_p \langle \sigma v \rangle - \lambda_\gamma N_2. \end{aligned} \tag{1.26}$$

Therefore the Saha equation can be used to describe the equilibrium abundance ratios,

$$\frac{N_2}{N_1 N_p} = \frac{\langle \sigma v \rangle}{\lambda_\gamma} = \alpha exp\left(-\frac{S_{1p}}{kT}\right). \tag{1.27}$$

The constant α contains terms related to the particles' normalized partition functions, masses, and spins. What is important here is the exponential dependence on the one-proton separation energy. Further details are provided in Ref. [54].

With the machinery and definitions in hand, consider the sequential one-proton captures from a waiting-point nucleus. One such example was illustrated with red arrows in Fig. 1.3 for ^{68}Se. The two relevant reactions are

$$\begin{aligned} 1 + p &\rightarrow 2 + \gamma \\ 2 + p &\rightarrow 3 + \gamma. \end{aligned} \tag{1.28}$$

If the first proton capture is in statistical equilibrium with photodisintegration, Eq. 1.26 and 1.27 can be used to express the equilibrium abundance of nucleus 2 as

$$N_2 = N_1 N_p \frac{\langle \sigma v \rangle}{\lambda_\gamma} = \alpha N_1 N_p exp\left(-\frac{S_{1p}}{kT}\right). \tag{1.29}$$

The rate of two $1p$ captures can be expressed in terms of the probabilities per unit time of the one-proton capture from nucleus 2 or the sequential captures from nucleus 1 as

$$r_{1\rightarrow 3} = N_2 \lambda_p^{'} = N_1 \lambda_{2p}, \tag{1.30}$$

where N_i are the equilibrium abundances of nucleus $i = 1, 2$. Thus the probability of capturing two protons per unit time λ_{2p} can be written with the help of Eq. 1.29 as

$$\lambda_{2p} = \frac{N_2}{N_1}\lambda_p^{'} = \alpha N_p exp\left(-\frac{S_{1p}}{kT}\right)\lambda_p^{'}. \tag{1.31}$$

Using Eq. 1.25 to substitute the reaction rate per particle pair for $\lambda_p^{'}$, the final expression for the destruction rate λ of the waiting-point nucleus is

$$\lambda = \lambda_\beta + \alpha N_p^2 exp\left(-\frac{S_{1p}}{kT}\right)\langle\sigma v\rangle_{(Z+1,N)}\,. \tag{1.32}$$

The beta-decay rate has been included to illustrate the two competing mechanisms by which the effective waiting-point lifetime is set.

From the exponential dependence on the proton separation energy evident in Eq. 1.32 it is clear that nuclear masses play a vital role in characterizing nucleosynthesis pathways by altering the effective waiting-point lifetimes. Correspondingly, much experimental effort has been devoted to measuring relevant masses with high precision (see, for example, the works of Ref. [55, 56]). Reliable nucleosynthesis network calculations require input parameters well grounded upon experimentally measured quantities in order to accurately model observed stellar abundances. In this manner, competing models can be vetted against one another.

Yet despite the utmost importance of accurate mass measurements, nuclei near or beyond the proton dripline suffer from both low production rates and short lifetimes [55]. For these nuclei, proton separation energies are not directly tractable from mass measurements and therefore calculations or extrapolations must be used. One such method calculates the difference in binding energy (rather, the Coulomb displacement energy) between mirror-pair nuclei. If the mass of the more neutron-rich nucleus is known, the mass of its proton-rich mirror pair can be extracted from the binding energy difference calculation with an error of roughly 100 keV [32, 33]. Proton separation energies along the dripline can also be obtained from lifetime measurements of the proton emitters, as discussed below.

Application of Proton Decay Lifetime Measurements

Proton decay lifetime measurements are a valuable resource by which unknown masses (and thus separation energies) can be experimentally constrained. Thus lifetime data is invaluable to galactic nucleosynthesis calculations. The simplest, and correspondingly the most rudimentary, link between the measured proton decay lifetime and separation energy is given within the framework of the semiclassical Wentzel, Kramers, and Brillouin (WKB) approximation. An example of constraining the proton separation energy from a one-proton decay lifetime measurement is given in Ref. [57]. There, the non-observation of ^{69}Br set a half-life upper limit of 24 ns and constrained the nucleus to be unbound by at least 500 keV, consistent with a recently measured one-proton separation energy of $S_p = -785$ keV [58].

A detailed derivation of the WKB approximation is beyond the scope of this work. Furthermore, the calculation for two-proton decay is based upon the emission of a diproton which is certainly an oversimplification. As mentioned at the beginning of this section, a more appropriate quantum mechanical description is necessary for accurate predictions. Nonetheless, a brief WKB discussion shall suffice to illuminate the point that decay lifetimes are intimately linked to decay (separation) energies. Heuristically, this correlation is obvious—the proton, despite having a positive S_p is trapped within the Coulomb and centrifugal barrier of the nucleus and therefore takes a finite amount of time to tunnel outside.

The two-proton decay lifetime can be written approximately as

$$\hbar\tau^{-1} = \Gamma_{2p} \propto exp\left(-2\int_{r_{in}}^{r_{out}} \sqrt{\frac{2\mu}{\hbar^2}\frac{m^*(r)}{m}\left|Q_{2p} - V(r)\right|}\right) dr. \tag{1.33}$$

Here, r_{in} and r_{out} are the classical turning points, μ is the reduced mass, $m^*(r)/r$ is the proton effective mass inside the nucleus, and $V(r)$ is some central potential. More details are provided in Ref. [59]. A similar discussion is found in [33]. There, it is noted that the largest uncertainty in estimating the lifetime is the two-proton Q-value. For instance, for $Q \sim 500$ keV, an uncertainty of ±100 keV results in a range of calculated lifetimes of nearly six orders of magnitude. It should be noted that by Eq. 1.33, an accurate experimentally measured lifetime can pinpoint the separation value. However, at such accuracy the uncertainties introduced by the simplified WKB diproton calculation and variations in both the potential $V(r)$ used and pre-factors not explicitly shown in the equation will dominate.

Though the WKB approximation provides a clear link between proton-decay lifetimes and separation energies, it is too simplistic of a model. Besides only considering the emission of a diproton, the calculations are only done at $E = Q_{2p}$ and therefore exclude the relative motion of the protons after tunneling through the barrier. These shortcomings are noted in Ref. [40, 60], where a more complex three body quantum mechanical calculation of the two-proton decay is discussed. This more realistic approach yields narrower proton decay widths than the diproton two-body WKB models, which leads to longer lifetimes in better agreement with various experimental observations. Such calculations significantly narrow the possible lifetimes within a given Q-value window (Ref. [39] provides an example).

Lifetime measurements are also useful for probing the validity of neutron-deficient nuclear models. From a spectroscopic S-factor, defined as the ratio between calculated and measured lifetimes, model deficiencies can be spotted. For example, large deviations of S from unity can indicate the presence of nuclear structure effects not explicitly accounted for in the model, such as deformation [61]. Indeed, deformation was suggested from the two-proton emission study of ^{94m}Ag, evidenced by a strong correlation between the emitted protons [62].

The study of proton emitters is therefore integral for the development of accurate elemental synthesis processes and reliable nuclear structure models along the proton dripline. The body of work presented in Ch. 4 and 5 introduces a new measurement technique by which the lifetime of such exotic decays can be studied.

Chapter 2

Experimental Methods

2.1 Introduction and Overview

Experiments conducted at the National Superconducting Cyclotron Laboratory (NSCL) study the properties of exotic nuclei that exist for only fleeting moments before decaying. They develop new production methods and measurement techniques necessary to explore nuclear structure at the extremes of isospin. Shedding light on the behavior of the most rare isotopes requires meticulous planning and the successful coupling of several state-of-the-art experimental devices. A succinct overview of the experimental procedure for a typical unstable beam experiment at NSCL follows immediately; the individual experimental techniques and devices utilized for the presented studies, along with the calibration routines and data analysis tools are then discussed in greater detail. While it should be noted that some experiments make direct use of stable primary beams or use experimental equipment in novel ways (see Ref. [63, 64] for examples), the following discussion is generalized for secondary beam experiments involving the production of short-lived nuclear states via nucleon knockout or Coulomb excitation and the subsequent study of the reaction products.

NSCL uses the fast-beam fragmentation method for isotope production and as such, every experiment begins with stable and electrically neutral atoms which must be ionized and accelerated to relativistic speeds near $0.5c$, where $c = 3 \times 10^8$ m/s is the speed of light in vacuum. These high-energy projectiles ($\sim$ 150 MeV/u) bombard a thick production target where all isotopes lighter than the projectile beam are produced via fragmentation. The production of isotopes can be treated with a variety of statistical models. Reference [65] and references therein provide more details and also describe other radioactive ion beam production methods such as fusion, fusion-evaporation, spallation, and neutron-induced fission. From the fragmentation remnants, a radioactive secondary beam is selected and delivered to the experimental target where the isotope of interest (perhaps in an excited state) is produced via single-step nucleon knockout or Coulomb excitation reactions. In order to ascertain the nature of the reaction in the target, both the incoming beam and the outgoing reaction residue must be properly identified. The incoming beam components can be separated by their time of flight between two scintillator detectors placed in the beam line upstream[1] of the experimental target. The reaction residues are identified on an event-by-event basis by their time of flight and energy loss signatures obtained from a spectrometer placed downstream of the experimental target.

For experiments such as the presented study of ^{18}C in Ch. 3, the excited nucleus emerges from the target and de-excites via photon emission. The gamma-ray energy, angular distribution, and emission point all contain vital information about the nucleus in its excited state and therefore photon detection is crucial. The Segmented Germanium Array (SeGA) [66], with up to eighteen high-purity segmented germanium crystals, serves this purpose and provides acceptable detection efficiency and good energy resolution. The isotope of interest may also decay by charged-particle emission if the excited state lies above the particle separation energy threshold. This is the case for the presented work on ^{19}Mg in Ch. 4, which lies

---

[1] The use of "upstream" and "downstream" is a customary practice and denotes relative position with respect to the propagation direction of the radioactive beam.

beyond the proton dripline and therefore decays by proton emission. In this scenario, the proton decay can be studied from reaction- and decay-residue energy loss information in charged-particle detectors.

In both cases, the desired experimental signal is masked by other events in the detectors from the presence of other reaction channels or decays and ambient background sources of radioactivity. Two actions reduce these sources of background in the experimental spectra. First, the experimental electronics can be triggered only when the corresponding reaction residue is detected downstream of the detector setup. This reduces background events from decays occurring naturally in the experimental vault. In addition, software gates on the appropriate incoming and outgoing experimental channels can be applied during data analysis to eliminate background events from unwanted contaminants and reaction residues. The reduction of experimental background improves the signal-to-noise ratio and is crucial for the success of experiments involving weak secondary beam intensities, small experimental cross sections, and low detection efficiencies.

It is therefore clear that experiments such as the presented studies of ^{18}C and ^{19}Mg require many different experimental devices—from beam production to reaction residue identification—to provide optimal beam current and purity, clean reaction residue separation, and high signal-to-noise experimental spectra. The following sections provide detailed descriptions of each of these components in the experimental device chain.

2.2 Radioactive Ion Beam Production

Both experiments were performed at the Coupled Cyclotron Facility (CCF) [67] at the National Superconducting Cyclotron Laboratory located on the campus of Michigan State University. Bringing the experiments to successful completion at NSCL required the coupling of several experimental components to produce and accelerate the primary beams and subsequently select and purify the radioactive secondary beams. Figure 2.1 provides a succinct summary of these components at the end of the section.

2.2.1 Primary Beam Ion Source

The primary beams accelerated by the CCF are comprised of stable ions. There are three ion sources at NSCL: the Superconducting-Electron Cyclotron Resonance ion source (SC-ECR) [68], the Advanced Room Temperature Ion Source (ARTEMIS) [69], and the Superconducting Source for Ions (SuSI) [70, 71]. All three ion sources operate on the principle of electron cyclotron resonance; a gas of the desired element is confined in a magnetic bottle and ionized by bombardment with electrons accelerated in a microwave radiation field. After ionization, the ions are extracted by a large electric field gradient of up to 30 kV and delivered to the K500 cyclotron. In the simplest case, the desired stable beam is a naturally occurring gas and can be directly injected into the magnetic bottle. If the desired element is a metal, an oven is used to heat the metal and the resulting gaseous vapor is injected into the magnetic bottle.

Both experiments utilized the SC-ECR ion source, from which high stable beam currents at low charge states were extracted. The stable beam injected into the K500 cyclotron for the ^{18}C experiment was ^{22}Ne^{4+} and therefore neutral Ne gas was used. For the ^{19}Mg experiment, ^{24}Mg^{5+} was injected into the K500 cyclotron and therefore the source oven was used to vaporize a sample of solid Mg.

2.2.2 Primary Beam Acceleration and Fragmentation

The K500 and K1200 cyclotrons of the CCF are responsible for the acceleration of the stable primary beams for experiments at NSCL. Inside each cyclotron, a strong magnetic field constrains the ion path to a circle whose radius increases with increasing ion velocity. The cyclotrons are isochronous; their RF driving frequency remains constant while the magnetic field strength increases with the ions' orbital radius to account for relativistic effects. An alternating electric field applied to three fan blade shaped "dees" provides the accelerating potential at a fixed frequency near 23 MHz. The ions are extracted from each cyclotron once their orbital radius can no longer be constrained internally. The maximum extraction energy for a proton (in MeV) is designated by the "K" value of each cyclotron. For heavier ions, the kinetic energy at extraction scales with Q^2/A as can be seen by equating the Lorentz and centripetal forces in the non-relativistic limit and solving for the velocity.

$$Bqv = \frac{mv^2}{r} \tag{2.1}$$

Here, $q = Qe$ where Q is the net charge number of the ion and e is the unit of electric charge. From Eq. 2.1 the Q^2/A dependence of the extraction energy is obtained.

$$E = \frac{1}{2}mv^2 \propto Q^2/A \tag{2.2}$$

Equation 2.2 suggests that to obtain the highest energy beams, only fully-stripped ions should be accelerated. Indeed, the primary beams of ^{22}Ne and ^{24}Mg mentioned above are light enough that they can be fully-stripped. However, the most intense beams from the SC-ECR are produced at low charge states. To balance the need for primary beams of high intensities and high energies, the K500 and K1200 cyclotrons are coupled. High intensity and low charge state stable ions are vertically injected from the SC-ECR into the K500 cyclotron, accelerated to approximately 0.15c, and then sent to the K1200 cyclotron. At the entrance of the K1200, the beam passes through a thin carbon foil where the remaining electrons are stripped allowing for maximum acceleration. For the presented experiments, the fully-stripped primary beams of ^{24}Mg^{12+} and ^{22}Ne^{10+} were accelerated to 170 and 120 MeV/u, corresponding to velocities of 0.53c and 0.46c, respectively.

After the production and acceleration of the primary beam, radioactive ions are produced by fragmentation as the beam impinges upon a thick production target located at the object position of the A1900 Fragment Separator [72]. For the ^{18}C and ^{19}Mg experiments, 1763 and 1081 mg/cm^2 beryllium targets were used, respectively. Most primary beam particles pass through the beryllium production target without undergoing any reactions. When reactions do occur, the beam particle is fragmented into many pieces. These reaction byproducts include every isotope lighter than the original primary beam. The radioactive secondary beam must then be separated from this collection of fragments.

2.2.3 Fragmentation Separation for Secondary Beams

The A1900 Fragment Separator is responsible for magnetically selecting the desired secondary beam from the fragmentation residues. The A1900 consists of several large-bore magnets: four 45° dipole bending magnets interspersed between a collection of 24 focusing quadrupole magnets. The magnetic field strength of the dipole magnets can be individually tuned such that the trajectory of the desired secondary beam follows the magnets' radius of curvature whereas unwanted fragmentation contaminants are either bent too much or too little and are not accepted in the next section of beam line. Isotopes are deflected according to their magnetic rigidity, $B\rho$, which from Eq. 2.1 is given as

$$B\rho = \frac{m}{q}v = \frac{A}{Q}\frac{u}{e}v, \tag{2.3}$$

where the radius of curvature of the magnet $r = \rho$ and u is the atomic mass unit.

The magnetic filtering still allows the transmission of beam contaminants with similar momentum-to-charge ratios as that of the desired radioactive beam due to the large momentum acceptance of the A1900 (up to $\Delta p/p = 5.5\%$). Yet the beam components will be spatially separated in the dispersive plane. To take advantage of this, three momentum apertures are installed at each image position (Image 1, 2, and 3) between dipole magnet pairs. A final mass aperture is installed at the A1900 focal plane. These adjustable slits restrict the space available for the beam to pass through. Additional separation is provided by an aluminum energy-degrading wedge installed between the second and third dipole magnets. The wedge—actually a curved foil of uniform thickness—provides a varying effective thickness profile in the dispersive direction, thus preserving the spectrometer's achromaticity [73]. Each beam component undergoes electronic stopping through the wedge and incurs a unique energy loss, $-dE/dx \propto Q^2$, given by the Bethe formula [74] as

$$-\frac{dE}{dx} = \frac{4\pi e^4 Q^2}{m_e v^2} NZ[ln\frac{2m_e v^2}{I(1-\beta^2)} - \beta^2]. \tag{2.4}$$

In the above expression, v and eQ are the velocity and charge of the fully-stripped ion beam, N and Z are the number density and the atomic number of the energy loss wedge, m_e is the rest mass of the electron, I is the average excitation potential of the wedge material, and β is the fraction of the beam velocity with respect to the speed of light, $\beta = v/c$. Appropriately tuning the two dipole magnets downstream of the wedge provides further separation of beam contaminants since their individual energy loss through the wedge results in contaminant-specific rigidities.

The final cocktail beam, comprised of the secondary radioactive beam of interest and any remaining contaminants, then emerges from the A1900 and is delivered to the experimental setup. Figure 2.1 illustrates the idealized situation where only the desired secondary beam emerges from the A1900. Differentiation among the remaining beam components is provided by time of flight measurements made by two thin plastic scintillators with respect to the experimental trigger. One scintillator is installed at the A1900 focal plane and the other is located near the experimental setup. For the presented studies, the cocktail beams were delivered to the secondary fragmentation target of the Köln/NSCL plunger [75] located at the

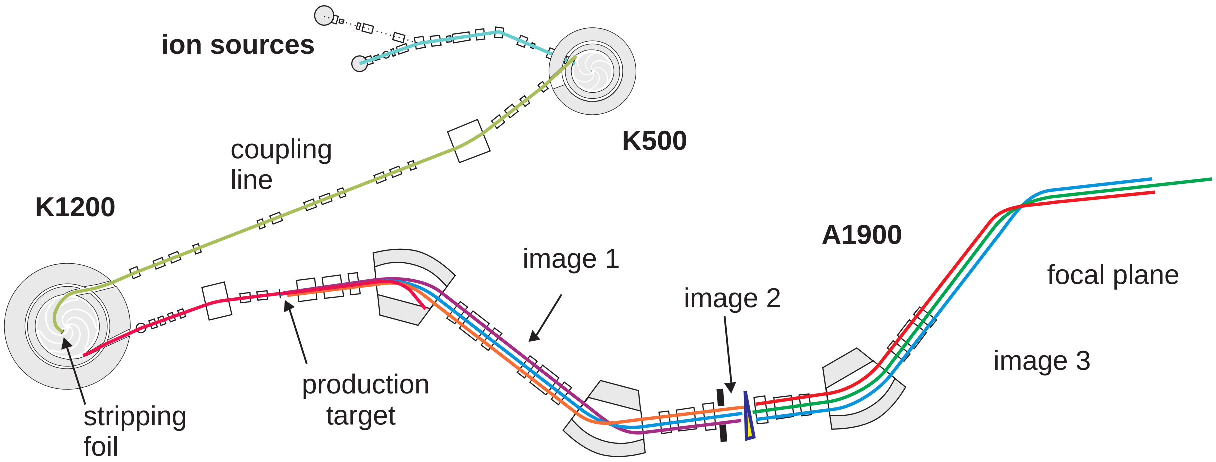

Figure 2.1: The various radioactive secondary beam production devices. The stable ion primary beam (cyan) is injected into the K500 from the SC-ECR ion source, accelerated, and sent to the K1200 (olive). The accelerated primary beam (magenta) impinges upon the production target and the fragments are separated according to their momentum-to-charge ratios (purple, blue, and orange). Energy loss through the aluminum wedge at Image 2 changes the rigidity of the beam (red, green, and blue) and only the desired secondary beam (green) is transmitted after passing through an aperture at the focal plane.

target position of the S800 Magnetic Spectrometer [76] and the time of flight was measured between the scintillators at the A1900 focal plane and S800 object position.

2.3 Experimental Technique and Devices

The presented works involved detecting short-lived radioactive isotopes and their decays. The experiments were designed to extract information on exotic nuclei existing far from the line of stability; ^{18}C is only four neutrons removed from ^{22}C, the heaviest carbon isotope, and ^{19}Mg lies beyond the proton dripline. For experiments involving such exotic nuclei, event rates are quite low and therefore the capability to detect both decays and reaction residues must be maximized. This involves using several detection systems concurrently to obtain highly selective data. For example, SeGA experiments have low in-beam gamma-ray detection efficiencies (on the order of a few percent) and it becomes vitally important to accurately

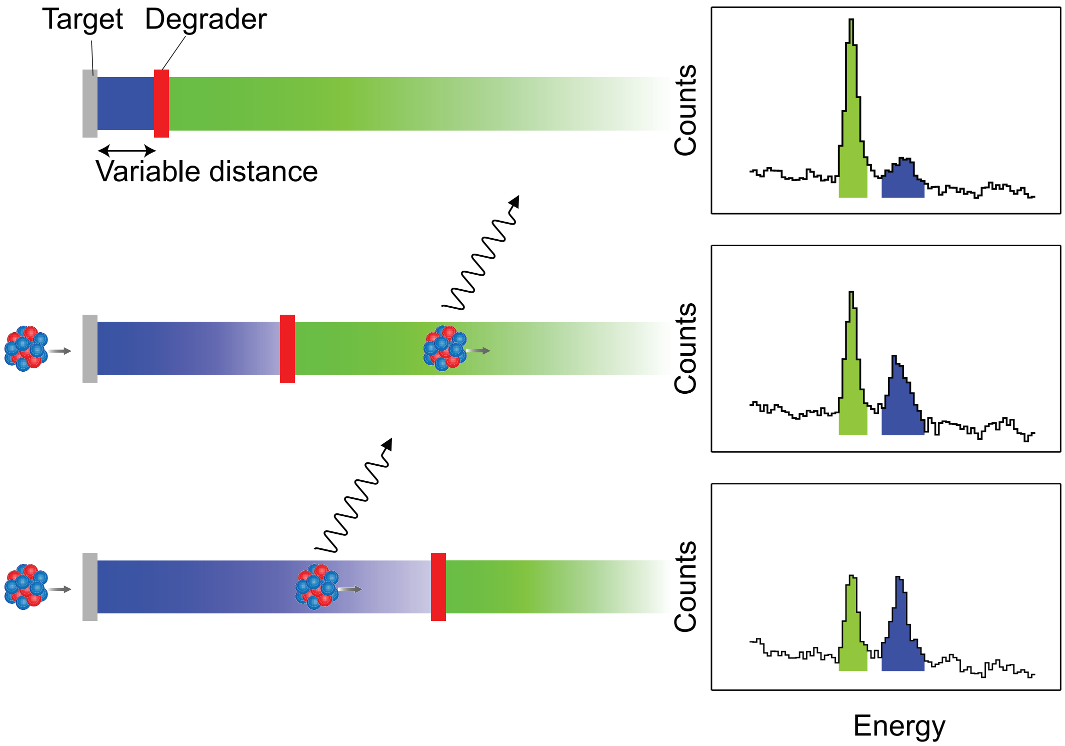

Figure 2.2: Schematic of the Recoil Distance Method for gamma-ray spectroscopy lifetime measurements taken from [3]. The intensity ratio of the two detected photopeaks varies as the distance between the target and degrader is increased. See text for details.

ascertain the origin of each detected decay to cull useful experimental information from the large swath of background signals. The successful event reconstruction in the presented experiments was made possible with event-by-event particle identification and tracking in the large-acceptance, high-efficiency S800 Magnetic Spectrometer, which facilitated the use of particle-specific software gating in the analysis to produce high signal-to-noise spectra.

2.3.1 The Recoil Distance Method

The two experiments used variants of the Recoil Distance Method (RDM). This experimental technique is described in general in Ref. [77]; the implementation optimized for intermediate energy radioactive isotope beams at NSCL is discussed in Ref. [20]. For RDM lifetime measurements via gamma-ray spectroscopy (as depicted in Fig. 2.2), an excited nuclear state emerges from the target (gray) and decays by gamma-ray emission either before (blue) or after (green) passing through the reaction residue velocity degrader (red). Neglecting nuclear recoil, the energy of the gamma ray in the rest frame[2], E_{rest}, is simply the energy level spacing between the initial and final states. The resulting gamma-ray energy in the laboratory frame, E_{lab}, is Doppler shifted according to the velocity of the excited nucleus at the point of gamma-ray emission, $\beta = v/c$, and the laboratory angle of emission relative to the beam velocity vector, θ, and is given by

$$E_{lab} = E_{rest} \frac{\sqrt{1-\beta^2}}{1-\beta\cos\theta}. \tag{2.5}$$

The observed gamma-ray energies in the laboratory frame must be Doppler corrected (or reconstructed) back to the rest frame to obtain an accurate description of the excited level structure of the nucleus of interest. For the presented lifetime study of the $2_1^+ \rightarrow 0_{gs}^+$ transition in ^{18}C, the average beam velocity downstream of the plunger degrader, β_{slow}, and the angle between the beam axis and the line segment connecting the target position of the S800 with the center of the SeGA segment in which the gamma-ray was detected, θ_{lab}, were inserted into Eq. 2.5 solved for E_{rest}. The Doppler correction therefore took the form

$$E_{rest} = E_{lab} \frac{1-\beta_{slow}\cos\theta_{lab}}{\sqrt{1-\beta_{slow}^2}}. \tag{2.6}$$

Appendix B provides a detailed derivation of the relativistic Doppler effect of Eq. 2.5 and a discussion of both the photopeak Doppler broadening and uncertainty of the Doppler reconstructed gamma-ray energy due to experimental uncertainties in Eq. 2.6.

---

[2] This work shall denote the two inertial reference frames as “rest” and “laboratory” frames. In the rest frame, the emitted gamma radiation energies would be detected just as they would if originating from a radioactive source at rest in the experimental setup. The laboratory frame is the experimental frame of reference, where relativistic effects of beam velocities around 0.3c are observed and must be accounted for.

After Doppler reconstruction, the gamma-ray energy spectrum exhibits two photopeaks with different energies corresponding to decays upstream and downstream of the plunger degrader. The intensity ratio of the two photopeaks will vary as a function of the lifetime, τ, and target-degrader distance, d. In the limits of very large or short distances compared to the transit of the reaction residue in one lifetime, $d >> \gamma v \tau$ or $d << \gamma v \tau$, only one photopeak will be detected.[3] From the experimental gamma-ray lineshapes at various distances, the excited state lifetime is obtained by fitting simulated lineshapes and minimizing the resulting χ^2 as a function of lifetime.

For RDM lifetime measurements via charged-particle spectroscopy, the degrader is replaced with a silicon double-sided strip detector (DSSD) which provides Z identification of the reaction and decay residues from energy loss measurements. To obtain the lifetime, the intensity of the energy loss peak of the nucleus of interest is monitored as a function of target-detector distance. To distinguish the experimental energy loss signal from contaminant isotopes with the same Z, and thus according to Eq. 2.4 the same energy loss, DSSD spectra are collected in coincidence with reaction residues detected in the S800. For two-proton decay studies, software particle gates on the ${}^{A-2}(Z-2)$ daughter nucleus in the S800 therefore unambiguously identify the nucleus of interest ${}^{A}Z$ from isotopic contaminants in the DSSD.

The essence of RDM lifetime measurements is to take advantage of the relationship between distance, velocity, and time. Nuclear states with short lifetimes ($\sim$ 1 ps) require very fast clocks ($\sim$ 1 THz) and excellent resolution for traditional lifetime measurements and are prohibitively difficult. The RDM technique translates the difficult study of very fast

---

[3] This neglects the impact of excited-state production in the plunger degrader. For very large distances compared to the nuclear transit, all excited states produced in the plunger target will decay upstream of the degrader. Thus the presence of a second photopeak at such large distances is indicative of excited-state production in the degrader and the subsequent gamma-ray decay further downstream. Determining this “production yield ratio” and its impact on the lifetime analysis is discussed in Ch. 3.

decay events with clocks into the study of decay spectra differences over very short, yet macroscopic, distances. For example, at typical NSCL secondary beam velocities of $0.3c$, an exotic isotope that decays 10 ps after its production will have traversed 1 mm. Therefore with an accurate knowledge of the beam velocity and the precise control over distances provided by the Köln/NSCL plunger, the lifetimes of very short-lived states can be accurately determined.

2.3.2 The Köln/NSCL Plunger

The Köln/NSCL plunger device was employed for the presented RDM measurements. The device offers precise control of the distance between an experimental target and velocity degrader or silicon DSSD. Such precise control over short distances, as mentioned above, is required to probe picosecond-lived nuclear states. The distance is manipulated by a set of plunger-mounted Exfo Burleigh Inchworm Motors. This motion system consists of three piezoelectric transducer (PZT) ceramic actuators. PZT materials exhibit crystal expansion along a linear axis in the direction of an applied electric field. A solid-state motion device consisting of PZT materials is thus very practical due to the lack of rotational motion and the absence of mechanical gears or hydraulic lines. Therefore, the system exhibits very precise and uniform one dimensional motion without mechanical vibrations or drift. Figure 2.3 illustrates the simple concept of the plunger PZT motor system. Two outer components act as clamps along the axis of motion while a central component acts as the linear expansion or contraction motor. All three components are physically connected to one another, but have individually applied bias voltages. By repeating the pattern of actions in Fig. 2.3, the motor can in principle progress forward or backward indefinitely. In the plunger setup, the degrader[4] is mounted to a fixed position and the target is mounted to the PZT motor. Therefore the motion of the target is restricted to a region less than 5 cm wide bounded by

---

[4] Or DSSD—the information in the following two subsections applies equally to the plunger for gamma-ray spectroscopy and the particle plunger for charged-particle spectroscopy.

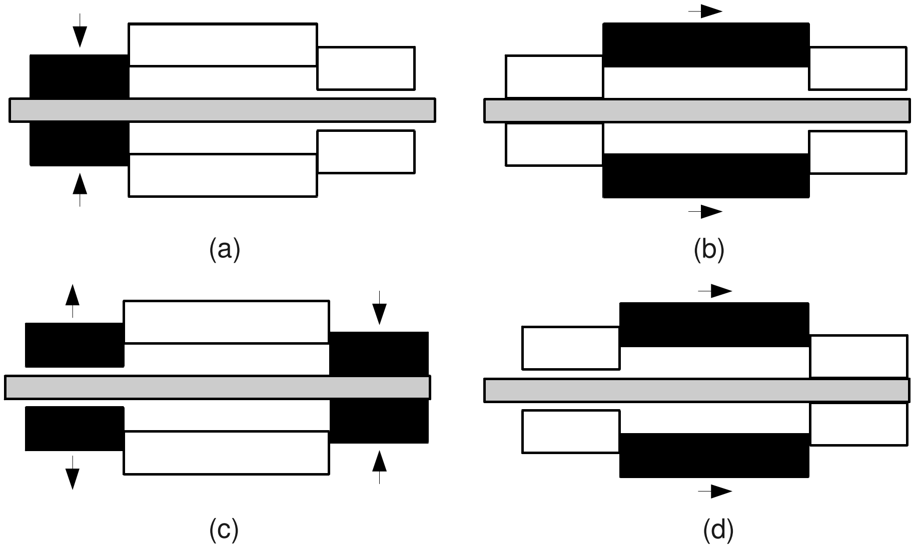

Figure 2.3: An illustration of the four actions required to increment the position of the plunger target. The rear PZT actuator clamps to the axis shaft (a), allowing the central PZT actuator to expand (b). To retract back to its original length, the front actuator clamps to the axis shaft while the rear shaft unclamps itself (c). Finally, the central PZT component can retract to its original length (d). Repetition of this sequence advances the target.

the initial position of the motor shaft and the fixed degrader. Within this region, the target can be moved in sub-micron steps in both directions.

Separation Distance Calibration

The distance between the plunger target and degrader is monitored and controlled by the accompanying Inchworm Control System, which consists of computer hardware and software, device controllers, and signal cables to connect the hardware to the PZT motors. The system measures relative distances. To obtain absolute distance measurements, the hardware must be calibrated to a zero-distance offset prior to plunger insertion into the beam line.

A proper zero-distance offset calibration first requires the parallel alignment of the target and degrader. This alignment is typically done by eye, since the human eye can discern separations of 50 μm or better. The plunger is placed on a large and clean white surface and illuminated from above with a bright light. The target and degrader are brought very

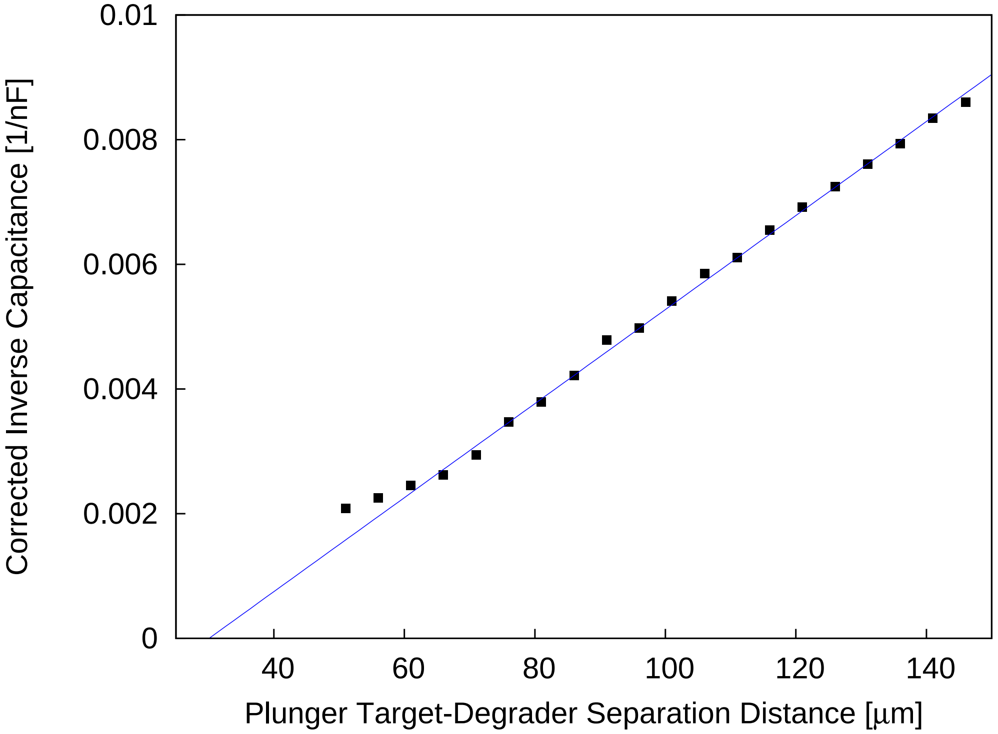

Figure 2.4: The inverse capacitance corrected for a measured stray capacitance of 1 pF is plotted against the relative distance between the plunger target and degrader. In this sample measurement, the extrapolated linear behavior of $1/C$ vs D indicates an offset from true zero of approximately 30 μm. Other measurements attained an offset closer to 10 μm.

close together and parallel alignment is achieved by adjusting the tension on a spring-screw system which affixes the target and degrader mounts to the plunger's support structure. Done carefully, a very narrow and uniform region of white will emerge between the two foils.

Once the target and degrader are parallel, capacitance measurements are taken as a function of distance to calibrate the zero-distance offset. Since the capacitance is inversely proportional to the distance between two parallel plates, the inverse capacitance should linearly decrease to zero with decreasing target-degrader distance. However, mechanical contact from imperfect parallel alignment or target/degrader surface imperfections is made prior to achieving true zero and the linearity vanishes.

Figure 2.4 illustrates sample zero-distance offset calibration data. An extrapolation of the data points beyond the breakdown in linearity observed at approximately 60 μm provides the zero-distance offset. With care, the extrapolated distance offset calibration can be observed closer to 10 μm. This suggests a maximum calibrated distance error on the order of 10 μm. For the presented works, such a small error of the calibrated distance is insignificant. For the ^{18}C study, data were collected at much larger distance increments (many hundreds of microns) whereas only data from the shortest distance were used in the analysis of ^{19}Mg. Furthermore, the thick targets used in both experiments result in an uncertainty in the knockout reaction location of several hundred microns, providing the dominant contribution to the uncertainty in the distance determination.

Plunger Alignment

After proper zero-distance plunger calibrations for both presented experiments, the device was mounted in the plunger beam pipe, which has a diameter to match the remainder of the S800 beam line, but is customized with positioning set screws and electrical feedthroughs for remote manipulation of the target-degrader distance. The setup is illustrated in Fig. 2.5. Care was taken to mount the plunger into the beam pipe so that the upstream face of the degrader was aligned with the geometrical center of SeGA at the target position of the S800.[5] Furthermore, the plunger's cylindrical symmetry axis was fixed to coincide with that of the beam pipe in order for the beam to pass unobstructed through the center of the plunger and impinge upon the center of the target and degrader.

For proper positioning, a mock-up plunger was constructed with the same outer diameter and length as the plunger and a thin aluminum cap imprinted with a crosshair reticle affixed

---

[5] A Cartesian coordinate system for the experimental setup has its origin at the S800 target position. The positive z-axis corresponds to the direction of beam travel. The positive x-axis corresponds to the dispersive direction of the beam (rather, the direction the beam is bent by the S800 dipole magnets) which is pointing straight up (against gravity). The y-axis is mutually orthogonal to the other two and therefore points perpendicular to the beam line and parallel to the floor.

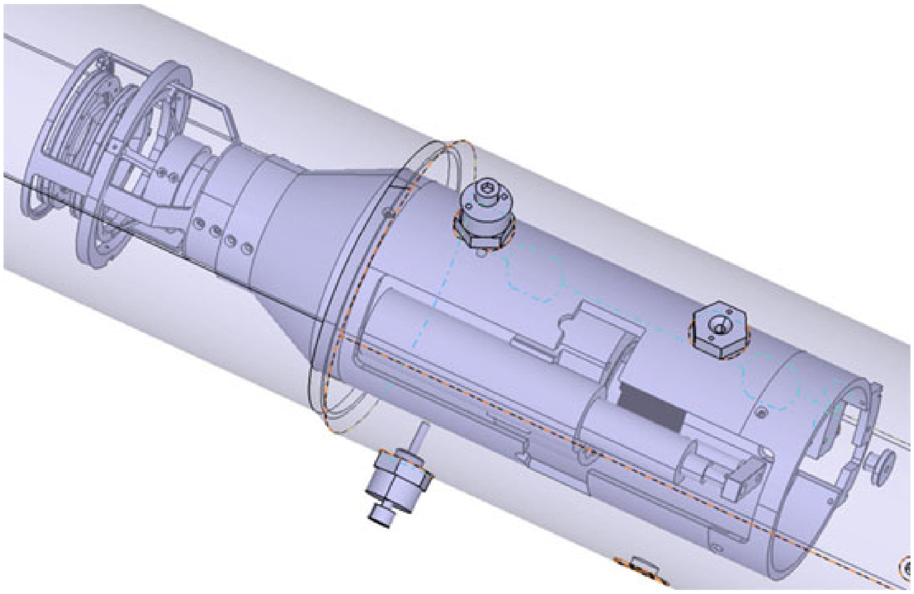

Figure 2.5: The Köln/NSCL plunger mounted in the plunger beam pipe. The beam passes through the center of the plunger, from the lower right to upper left of the figure, and impinges upon the target and degrader which are mounted by support rings on the downstream edge of the device. The prominent cylinder on the plunger body is the PZT Inchworm motor housing.

to its downstream edge. The mock-up was inserted into the beam pipe such that the aluminum cap was aligned at $z = 0$ mm and the distance from the lip of the beam pipe to the upstream edge of the mock-up was noted. With the z position fixed, a surveyor's telescope placed between the two quadrupole magnets of the S800 analysis line was centrally aligned with the beam axis using a crosshair reticle on the downstream edge of the final quadrupole magnet. This reticle target was removed and the telescope was refocused onto the mock-up's crosshair reticle. Then, the plunger beam pipe positioning set screws were adjusted so that the mock-up plunger was secure on all sides and aligned with the beam axis. With the final alignment set, the top positioning set screws were loosened, the mock-up was retracted, and the Köln/NSCL plunger was inserted and secured into its aligned position.

With the plunger installed and aligned, the PZT motor controls were connected through the beam pipe feedthroughs to the external hardware system that was installed near the beam line in the experimental vault. The Köln/NSCL plunger target-degrader distance was manipulated remotely during the experiment via a coaxial cable link between the hardware in the vault and a controller computer in the Data-U.

Specifics for Gamma-Ray Spectroscopy

The Köln/NSCL plunger was designed for RDM lifetime measurements at NSCL where the state of interest is produced from the secondary beam on the plunger target via single-step knockout reactions or Coulomb excitation [20–22, 78, 79]. For knockout reaction studies, carbon or beryllium foils are used for the experimental target and heavier metals, such as gold, tantalum, or indium, are used for the degrader. For Coulomb excitation measurements, a large target Coulomb field is necessary and therefore high-Z foils such as niobium or tungsten are used. Regardless of the reaction mechanism employed for the production of excited states, the chosen foil thickness and degrader material depend upon several experimental considerations.

The most important consideration is preserving the ability to resolve the two photopeaks resulting from decays before and after the plunger degrader. The energy difference is due to the Doppler effect (Eq. 2.5); for fixed SeGA angles, the choice of degrader material and thickness dictates the change in beam velocity and thus the photopeak energy separation. Another consideration is optimizing the target thickness. The target must be thin enough that at the 0 μm distance the excited state can fully emerge from the target and slow in the degrader before decaying. Conversely, the target must be thick enough for an acceptable production yield of the state of interest. To balance these competing needs, proper experimental planning is crucial. This need has been met with a Monte-Carlo simulation package that will be discussed in Subsect. 2.4.2.

As the experiment progresses, gamma-ray spectra are collected at several plunger target-degrader distances. For the analysis, the most important piece of information that comes directly from the plunger is this distance. If the zero-distance offset calibration was done carefully, then the distance information is quite accurate since the Burleigh Inchworm PZT motor system makes relative moves from one distance to the next with sub-micron accuracy. The actual distance is therefore simply read as the relative distance minus the calibrated offset. More importantly, there is no mechanical drift. Temperature fluctuations can have a minimal impact on the target-degrader distance, and though this can be automatically monitored and corrected by the Burleigh Inchworm system, the effect was considered negligible.

Specifics for Charged-Particle Spectroscopy

The modified Köln/NSCL plunger was designed for RDM lifetime investigations of particle-decaying isotopes by replacing the degrader with a silicon energy loss detector. The presented ^{19}Mg two-proton decay lifetime measurement therefore serves as a proof of concept for the charged-particle RDM, or particle plunger, lifetime measurement technique. Despite the various difficulties encountered in the preparation and execution of the experiment that are mentioned below, the successful lifetime measurement as presented in Ch. 4 validates this experimental method and warrants future work and improvements. The difficulties mentioned serve as guidance for future particle plunger experiments.

For the ^{19}Mg two-proton decay lifetime measurement, two Micron Semiconductor silicon DSSDs were purchased (thicknesses of 140 and 300 μm), each with an active area of 50 mm x 50 mm and electronically segmented into 16 strips vertically on the upstream face and horizontally on the downstream face with a pitch of 3.125 mm. Manufacturing issues prevented the delivery of the thinner DSSD and delayed the delivery of an operational thicker DSSD until the day before the experiment. The DSSD silicon wafer was affixed to a ceramic mount such that the upstream face of the wafer and the plunger target could be brought together without the ceramic mount interfering.

The plunger PZT motor control signals are a source of electrical noise. Therefore the

DSSD was mounted to the plunger support with electrically insulating nylon screws and spacers. Nonetheless, significant noise was observed in the detector when the external plunger control hardware was connected to the beam pipe. Therefore all supporting plunger electronics were kept off except when the target-DSSD distance needed to be changed.

It is important to note that the exposed DSSD and ceramic mount are quite fragile and therefore great care is necessary when aligning the plunger with the S800 target position and ensuring its parallel alignment to the beam axis. The positioning set screws and a stopper block meant to lock the z-axis position of the plunger protrude inside of the beam pipe. Sufficient care was not exercised after the experiment; upon extraction from the beam pipe, a corner of the ceramic mount was fractured, severing several strip-to-pin connections and preventing post-experimental source calibrations from being made. Instead, the characterization and calibration of the DSSD during the analysis was done with unreacted beam data.

The detector was biased to its depletion voltage of 80 V and the leakage current was noted on a run-by-run basis to monitor beam damage. A small increase in leakage current—insufficient to result in performance degradation—was observed. To bias the detector and extract the energy loss, strip identification, and timing information from the DSSD, a section of beam pipe was modified with a vacuum-tight 34-pin ribbon cable feedthrough. The detector signals were extracted via ribbon cable through the feedthrough and were passed to a simple ground signal splitter board. This board replicated the two ground signals from the DSSD (one from each face) into two sets of sixteen. From the splitter board, two ribbon cables each transmitted 16 signal-ground input pairs to a MultiChannel Systems preamplifier. The two preamplifier modules had inverted and non-inverted signal output options to allow the signal from both DSSD faces to be passed with the same polarity.

From the preamplifiers, the detector signals were sent to a pair of 16-channel, double width CAMAC shaper and discriminator modules from Pico Systems. From the discriminators, the signals were first sent to ECL-to-NIM converters and then to Phillips Scientific 7186 TDCs to extract the timing information. Timing troubles arose during the experiment; troubleshooting was abandoned in an effort to collect energy loss data. The shaper signals were sent to a pair of single-width CAMAC Phillips Scientific 7164 ADC modules where pulse amplitude (energy) and channel (strip) information was converted to a digital signal.

DSSD Detector Characterization

The two-proton decay RDM lifetime measurement requires the identification and integration of the energy loss (ΔE) peak in the DSSD from the parent nucleus ${}^{A}Z$ in coincidence with the detected heavy-ion decay residue ${}^{A-2}(Z-2)$ as a function of target-detector distance. As will be discussed in Ch. 4, the combined low statistics and short two-proton decay lifetime of ^{19}Mg prevented the analysis from proceeding in such a manner. Instead, lifetime information was obtained by fitting simulated ΔE lineshapes to the experimental DSSD spectra at 0 μm and minimizing the resulting χ^2 as a function of lifetime.

The experimental ΔE DSSD spectra were generated by summing the signals from the gain-matched upstream strips of the DSSD. 93% of the events consisted of energy deposits in only one strip. Gain matching was done using unreacted beam data. The centroid energy loss of each incoming beam component was extracted from a Gaussian fit to the peaks of the strip spectra. These centroids were then used to extract strip-by-strip gains and offsets from their linear fit to a representative strip with the smallest raw energy loss signal. Gain-matched unreacted beam ΔE spectra are presented in the first two columns of Fig. 2.6 for select strips from the upstream DSSD face. The summed spectrum of all 16 gain-matched strips is presented in the third column. The full-width at half-maximum energy resolution for ^{20}Mg was calculated to be 4.1%. Note that this resolution was dominated by the incoming momentum spread of the beam, energy and angular straggling through the target, and similar straggling through the dead layers of the detector; the intrinsic resolution of a silicon detector is typically on the order of, or better than, 1% [80, 81].

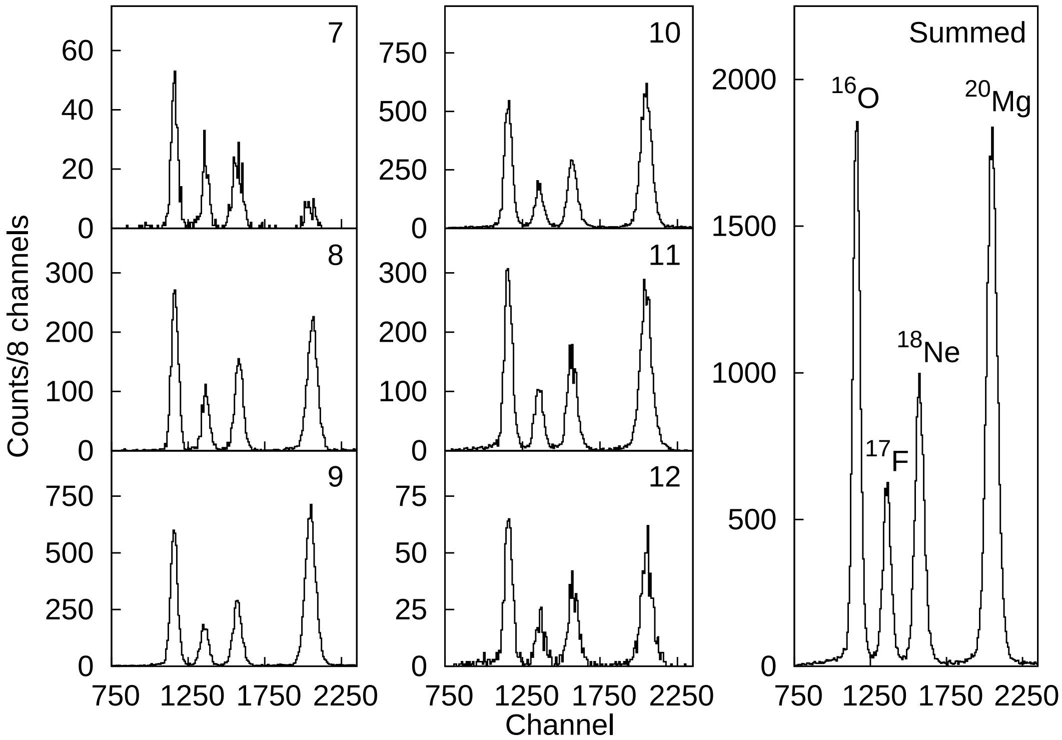

Figure 2.6: Silicon DSSD energy loss spectra for the unreacted beam components ^{16}O, ^{17}F, ^{18}Ne, and ^{20}Mg. Select vertical strips from the upstream DSSD face are plotted in the first two columns. Panel labels denote the strip number; strips were sequentially numbered from left to right when viewed upstream of the detector. The summed spectrum of all 16 gain-matched vertical strips is plotted in the third column.

2.3.3 The S800 Spectrometer

In the presented ^{18}C and ^{19}Mg studies, the reaction residues emerged from the Köln/NSCL plunger target, decayed in flight after a distance governed by their velocity and half-life, and were identified by the S800 Magnetic Spectrometer. The S800 is a large-acceptance, high-efficiency magnetic spectrometer with high energy resolution and good angular resolution. Like the A1900, it is an ion optical system—just as lenses and prisms are photon optical systems—and operates on the principles of magnetic separation via the momentum-to-charge ratio of ions as given in Eq. 2.3. Figure 2.7 illustrates the main features of the S800, including the two main components: the analysis beam line and the spectrometer. The analysis line extends from the object to target positions and consists of four 22.5° bending dipole

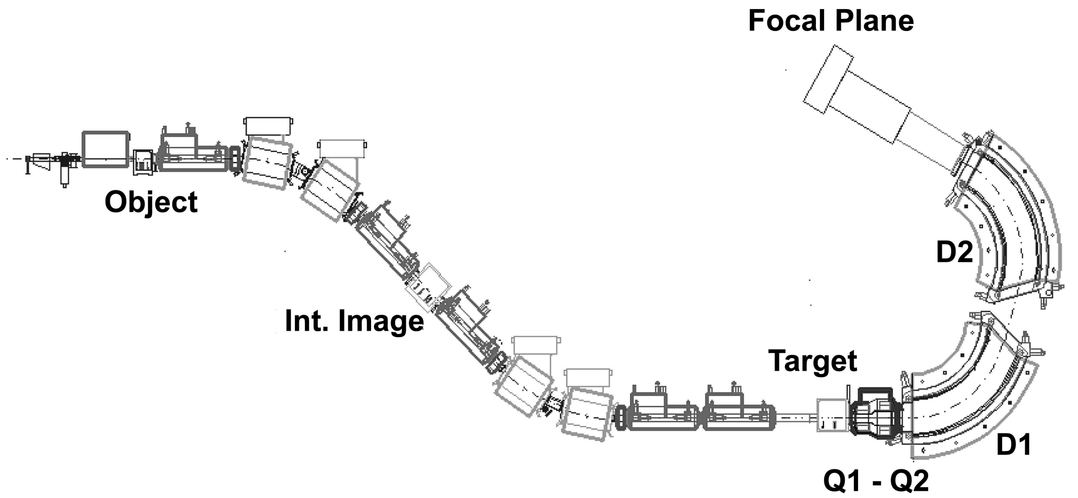

Figure 2.7: An illustration of the S800 Magnetic Spectrometer. Radioactive ion beams are delivered to the experimental target through the analysis line. Reaction residues emerge from the target; those within the acceptance of the S800 spectrometer are delivered to the focal plane, which consists of several detectors for position, timing, and energy measurements. See text for more details.

magnets, five quadrupole focusing magnets, and several sextupole correcting magnets. The spectrometer extends vertically from the target position to the focal plane as two large-bore quadrupole magnets and two 75° dipole magnets. The spectrometer has a large solid angle acceptance of $\Omega = 20$ msr, which approximately corresponds to angles of 7° in the dispersive and 10° in the non-dispersive directions.

The secondary beams selected by the A1900 Fragment Separator are delivered to the S800 and focused at the object position. Two main modes of S800 operation determine where the final focus of the beam is located. In *dispersion matching* mode, both the analysis line and the spectrometer are achromatically tuned such that the beam is focused at the focal plane and momentum dispersed at the target position. This configuration allows for the best energy resolution ($\Delta E/E = 2 \times 10^{-4}$ with a nominal 1 mm diameter beam spot at the object position) since the intrinsic momentum spread of the beam at the object position is canceled at the focal plane. However, the momentum dispersion at the target position restricts the acceptance to $\Delta p/p = \pm 0.25\%$ for a 5 cm square target. In *focused* mode, the analysis line is achromatically tuned such that the beam is focused at the target position and momentum dispersed at the focal plane. This allows for maximum momentum acceptance of the S800 ($\Delta p/p = \pm 2.5\%$), as ions of all momenta accepted by the analysis line arrive together as a small beam spot on the experimental target, but a lower energy resolution of $\Delta E/E = 10^{-3}$.

Both experiments used the S800 in focused mode to track and detect outgoing reaction residues emerging from the experimental target on an event-by-event basis. This facilitated particle tagging of decay events detected in SeGA or the particle plunger DSSD and significantly reduced unrelated background signals in these detectors. Spectra demonstrating the improvement in detector signal-to-noise ratios are provided in Ch. 3 and 4.

The following subsections detail the various detector systems of the S800 used for the ^{18}C and ^{19}Mg experiments. Several optional detectors, such as beam tracking parallel plate avalanche counters at the intermediate image of the analysis line, were not utilized in these works and therefore will not be discussed. The majority of the S800 detectors are located in the focal plane [82], including the cathode readout drift chambers (CRDCs), the ionization chamber (IC), and three plastic scintillators (E1, E2, and E3; 3 mm, 5 cm, and 10 cm thick, respectively) . The cross sectional dimension of each focal plane detector is approximately 30 cm wide by 60 cm tall. An experimental "S800 singles" trigger is generated from the fast timing pulse generated by an event in the E1 scintillator. This singles trigger can drive the experimental data acquisition by initiating the electronic readout of the detector hardware. This triggering scheme was utilized in the ^{19}Mg experiment, where the silicon DSSD energy loss signals of all particles accepted by the S800 were recorded. Alternatively, a logical "AND" between the S800 singles trigger and an external trigger generated by an auxiliary detector system can drive the readout. This scheme was adopted for the ^{18}C experiment, where only events corresponding to the detection of a reaction residue in the S800 and a gamma-ray energy deposition in SeGA within a 600 ns coincidence window were recorded.

Time of Flight Scintillators

Thin organic plastic scintillators are used for time of flight measurements. The light output generated by ionizing beam particles passing through the detectors is converted to electric current in a photomultiplier tube attached to the scintillator by the photoelectric effect and subsequent charge multiplication. In general, these detectors are not ideal for elemental identification as they have relatively poor energy resolution. However they have very fast decay times and therefore provide fast and reliable timing pulses.

A thin 1 mm plastic scintillator was installed at the object position of the S800 for both of the presented experiments. Together with a plastic scintillator installed at the focus of the A1900 (130 μm and 1 mm for the ^{19}Mg and ^{18}C experiments, respectively), the secondary beam components were separated by their time of flight between the two. The time of flight was computed from the timing difference between the two scintillator signals with respect to the common S800 trigger and enabled precise selection of the incoming beam component in the analysis. In addition, the thin E1 focal plane scintillator provided a timing signal which, when compared to the scintillator signal at the object position, yielded the time of flight through the S800.

Ionization Chamber

The ionization chamber is a Frisch gridded gas-filled ion chamber. The detector is segmented into 16 one inch anodes and filled with 140 Torr of P10 gas (a mixture of 90% argon and 10% methane). As the beam traverses the ion chamber perpendicular to the anode segmentation and between the Frisch grid and cathode, ion pairs are created in the gas. The energy deposited by the beam is measured by the collection of the electrons on the anode pads and is correlated to the residues' atomic number Z. This elemental identification together with the time of flight measurements served to unambiguously identify the reaction residues emerging from the plunger target.

To extract the average energy deposited for each event, the 16 anode channels were calibrated against one another. The procedure is outlined below. The calibrated energy readout of each channel was assumed to sample a Gaussian energy loss distribution. Thus, each event produced sixteen samples of this distribution, from which a centroid and standard deviation were calculated. If a channel's calibrated energy fell outside of one standard deviation from this centroid value, it was neglected and the arithmetic average energy deposit for the event was calculated from the remaining anode channels.

Cathode Readout Drift Chambers

The CRDCs are a pair of position sensitive drift detectors filled with a gas mixture of 80% carbon tetrafluoride and 20% isobutane to a pressure of 50 Torr. Each detector has an active depth of 1.5 cm. The high velocity reaction residues interact with the CRDC fill gas and, as in the case of interactions in the ionization chamber, create ion pairs. The electrons from the ionization of the CRDC gas drift through a Frisch grid and are amplified and collected on an anode wire. The charge on the anode wire induces a signal on a nearby pair of cathodes located on either side of the anode wire. Each cathode is segmented into 224 individual readout pads forming a linear chain. To determine the dispersive (x) position of the beam passing through the CRDC, the image charge distribution on the cathode pads is fit to an assumed Gaussian peak shape and the centroid is extracted. The non-dispersive (y) position of the beam passing through the CRDC is determined by the drift time of the electrons, which is extracted from the timing difference between the charge pulse on the anode wire and the S800 trigger from the E1 scintillator. The position resolution attained from these measurements is approximately 0.5 mm in both the dispersive and non-dispersive directions. It should be noted that for such large volume drift detectors, the charge collection process is relatively slow (tens of microseconds) and therefore to avoid detector malfunction or efficiency losses due to pile up, dead time, and other effects, the CRDC count rate is limited to 5 kHz.

The set of coordinates (x, y) determined by each CRDC were used to determine the focal plane positions and angles of each beam particle. From the pair of coordinates and the known distance of about 1 m between the two CRDCs, the angles at the focal plane in the dispersive and non-dispersive directions (a_{fp} and b_{fp}, respectively) were calculated. In addition, CRDC2 is positioned at the S800 optical focus and therefore its extracted beam particle coordinates (x, y) corresponded to the focal plane position in the dispersive and non-dispersive directions (x_{fp} and y_{fp}, respectively). To extract proper position and angle information about the beam, both CRDCs were calibrated by detecting beam ions with well defined and precise spatial positions. These calibrations are discussed in the following subsection.

Detector Calibrations

The position and angle information derived from the CRDCs were used to track the reaction residues' position, angle, and momentum spread as they emerged from the plunger target. To provide accurate tracking information, the CRDCs were first calibrated such that the detector response to an incident beam particle was correlated to a well defined (x, y) spatial position. To accomplish this calibration, a pair of thick tungsten beam blocking masks were used. A geometrical pattern of slits and holes are stamped through each mask at well defined positions. Thus, only beam particles incident upon the slits or holes entered the detector and the resulting electronic response was correlated to a precise spatial position. During a mask calibration, unreacted beam was swept across the entire focal plane by varying the magnetic field settings of the S800 to ensure the detector response over the entire face of the CRDC was probed. To obtain a complete set of CRDC calibration parameters (gains and offsets for CRDC1 and CRDC2), the experimental CRDC detector response to beam ions passing through each slit and hole was linearly fit to the known slit/hole positions on the two masks.

Several mask calibration runs were taken during each experiment to properly characterize the CRDCs as a function of time. This was necessary since the detector response is intimately linked to the operating conditions, such as temperature, gas pressure, and radiation damage, which affect the ion-pair production and electron mobility. The set of obtained gains and offsets from each mask calibration must be appropriately implemented in the analysis. For the analysis of the ^{18}C and ^{19}Mg data, run-by-run CRDC gains and offsets were obtained by linear interpolation of the results from each mask calibrations as a function of time.

The 16 anode channels of the ionization chamber were also calibrated such that the energy loss peak from each channel aligned with that of the other 15 channels. To complete this task, data with two or more beam species present in the IC (corresponding to two or more distinct energy loss peaks) was used; for the ^{19}Mg experiment, this was accomplished by delivering the unreacted beam components to the S800 focal plane while for the ^{18}C experiment, the reaction products from the ^{19}N secondary beam impinging upon the plunger target were used. A Gaussian was then fit to each energy loss peak and the centroids were extracted from each channel. From these centroids, gains and offsets were obtained from the linear fit of each channel to a chosen representative channel with the smallest uncalibrated energy loss signal.

The incoming secondary beam emittance, reaction kinematics, and straggling through the plunger target and degrader all have an impact on the spread of trajectories through the S800 for a given beam species. With properly calibrated CRDCs, the exact trajectory of each beam ion in the S800 was deduced (discussed below). With this knowledge, a path length correction was applied to both the calibrated ionization chamber energy loss and time of flight data. This was done by constructing a two dimensional histogram plotting the energy loss or time of flight information against the CRDC-determined focal plane position and angle information. The position/angular dependence of the measured energy loss or time of flight was manifest by a correlation in these plots. A simple constant of proportionality was then determined by eye to remove the observed correlation. The resulting trajectory-corrected

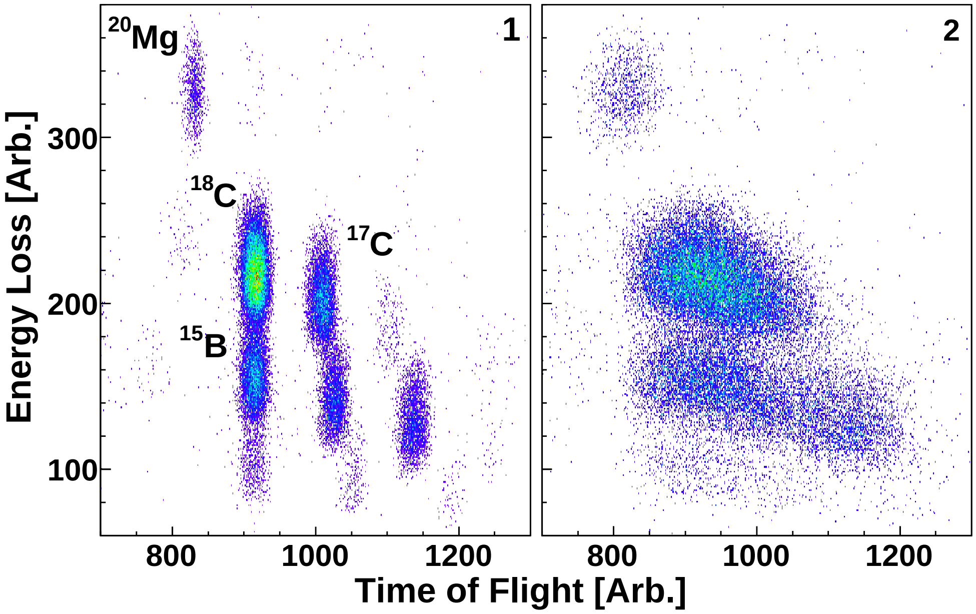

Figure 2.8: S800 trajectory-corrected (Panel 1) and -uncorrected (Panel 2) identification of the outgoing reaction residues from the incoming ^{19}N secondary beam on the plunger target by time of flight and energy loss information from the S800 Spectrometer. Increasing time is from the right to left along the abscissa.

time of flight and energy loss spectra exhibited increased resolution and the resulting particle identification plot of energy loss in the IC versus time of flight through the S800 was much improved. Figure 2.8 illustrates the striking improvement in resolution attained by these trajectory corrections from the presented work in Ch. 3.

Inverse Map Trajectory Reconstruction

For the presented study of ^{18}C and ^{19}Mg, the tracking of the outgoing reaction residues from the focal plane back to the S800 target position was of great importance for understanding the kinematics introduced by the knockout reaction. Comprehensive simulations played an important role in the analysis of both experiments. In particular, the spread of outgoing reaction residue momenta had to be accurately reproduced in the simulation in order to obtain realistic Doppler broadened SeGA gamma-ray energy or silicon DSSD energy loss simulated spectra. Thus, trajectory reconstruction via an inverse transfer map was done on an event-by-event basis.

The analytical method for event-by-event beam ion trajectory reconstructed in the analysis was based upon the ion optics code COSY Infinity [83] which calculates a transfer map $\mathcal{S}$ of the spectrometer based upon its measured magnetic field. The inverse transfer map $\mathcal{S}^{-1}$ relates the measured focal plane parameters x_{fp}, y_{fp}, a_{fp}, and b_{fp} to the target parameters y_{ta}, a_{ta}, b_{ta}, and d_{ta} (the y position, dispersive and non-dispersive angles, and energy deviation from the central trajectory, respectively) according to

$$\begin{pmatrix} a_{ta} \\ y_{ta} \\ b_{ta} \\ d_{ta} \end{pmatrix} = \mathcal{S}^{-1} \begin{pmatrix} x_{fp} \\ a_{fp} \\ y_{fp} \\ b_{fp} \end{pmatrix}. \tag{2.7}$$

Note that the dispersive position at the target, x_{ta}, is assumed to be negligibly small and is set to 0 in order to extract the energy at the target, d_{ta}. Thus the inverse transfer map results in the reconstruction of the momentum vector for each reaction residue (defined by a_{ta}, b_{ta}, and d_{ta}) and position in the non-dispersive direction at the target. Since the spectrometer separates particles according to their momentum-to-charge ratios, an inverse transfer map must be calculated for each reaction residue.

2.3.4 The Segmented Germanium Array

The Segmented Germanium Array is used extensively at NSCL for gamma-ray spectroscopy experiments. Short-lived excited states below the particle separation energy threshold typically decay by gamma-ray emission. Gamma-ray spectroscopy with SeGA in coincidence with reaction residue identification in the S800 Spectrometer yields final state information from nuclear reactions. It is therefore a powerful tool for probing nuclear structure properties far from stability such as transition strengths, nuclear deformation and collective behavior, cross sections, and spectroscopic factors.

SeGA consists of up to 18 high-purity, n-type cylindrical coaxial germanium crystals. Each crystal measures 80 mm in length and 70 mm in diameter and is electronically segmented into 8 slices transverse to the cylindrical symmetry axis and radially divided into four quarters. A central core electrode along the symmetry axis is biased during operation to $\sim$ 4000 V while the outer contacts of each of the 32 segments are grounded. The crystals are oriented such that the symmetry axis is perpendicular to the line segment connecting the S800 target position and crystal midplane. Figure 2.9 provides a schematic representation of a single crystal's segmentation scheme and the nomenclature used for identifying each segment. The crystals are kept at a temperature around 100 K by thermal contact with a cold finger to a 2 L liquid nitrogen reservoir oriented at 45° with respect to the crystal cylindrical axis.

The 32-fold electrical segmentation of each SeGA detector provides excellent angular sensitivity without relinquishing the detection efficiency afforded by a large crystal. This design enables both the accurate determination of the angle of the first interaction and the ability to absorb the full gamma-ray energy. The mechanism by which gamma rays interact with a detecting medium depends upon the photon energy. Section C.1 of Appendix C provides more details on the interaction of gamma rays with matter. For gamma-ray energies of several hundred keV to a few MeV, single or multiple Compton scattering followed by photoelectric absorption are the most probable interaction mechanisms; full energy deposition in a single SeGA segment is quite unlikely. Thus in order to properly Doppler reconstruct each event via Eq. 2.6, the angle of interaction, θ_{lab}, is taken from the segment with the largest energy deposit while the charge collected by the central electrode from the sum of all interactions within the crystal is used to gather the full energy deposition for the event, E_{lab}. For photon energies $E_\gamma > 500$ keV (and this is the case for all measured Doppler shifted transitions in the ^{18}C study) this algorithm has been determined to be robust [84].

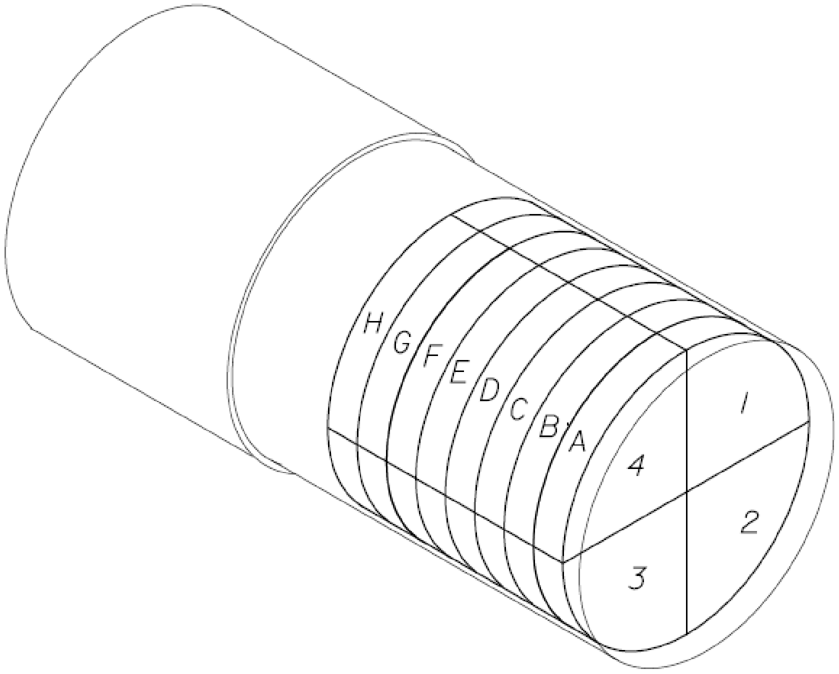

Figure 2.9: An illustration of a single Segmented Germanium Array crystal. Each of the eight slices transverse to the cylindrical symmetry axis are labeled with a letter A through H, with slice A closest to the beam pipe in the setup for the ^{18}C experiment. The four radial quarters are numbered 1 through 4, with quarters 2 and 3 closest to the beam pipe in the experimental setup. Preamplifiers and other electronics are housed behind slice H.

The intrinsic energy resolution of germanium detectors (on the order of 0.1%) is vastly superior to the commonly used alternative sodium iodide scintillator detector (between 6% and 8%). It is therefore desirable to utilize this enhanced resolving power in experiments that involve the detection of multiple gamma rays. However, germanium as a detection medium is quite costly and large volume single crystals are difficult to grow; for SeGA the price of this excellent energy resolution is small solid angle coverage and thus a low gamma-ray detection efficiency (on the order of 1%). The efficiency can be increased by installing the detectors closer to the experimental target. However, this increases the opening angle of a given segment and therefore the angular uncertainty for Doppler reconstruction.

The ultimate trade-off between efficiency and angular resolution drives several standard SeGA configurations that are available for different experimental needs. Delta SeGA (c.f. James “Russ” Terry’s thesis [85]) is configured to cover many different angles for angular correlation measurements. Classic SeGA (c.f. David Miller’s thesis [86]) has been utilized for gamma-ray polarization measurements. Barrel (Beta) SeGA (c.f. Joshua Stoker’s thesis [87]) has been used for maximum solid angle coverage.

The ^{18}C experiment utilized 15 detectors in the Plunger SeGA configuration, which consists of 8 detectors in the $\theta = 140^\circ$ backward ring and 7 detectors in the $\theta = 30^\circ$ forward ring.[6] The detectors are spaced at 45° intervals azimuthally symmetric to the beam axis (aside for one hole in the forward ring to accommodate a beam line vacuum valve). The forward and backward rings were placed approximately 30 cm and 23 cm radially, respectively, from the $z = 0$ target position of the S800 (which corresponds to the upstream face of the plunger degrader). The detector placement of SeGA is such that each slice is at a different polar angle θ with respect to the beam axis. The chosen angles for the forward and backward rings are the extrema achievable with the plunger beam pipe and therefore provide the maximum Doppler shift between gamma rays detected in the two rings. A diagram of the setup is provided in Fig. 2.10, with only the $\phi = 0^\circ$ detectors pictured for clarity.

Calibration Routine

Like the detectors in the S800 focal plane, the SeGA detectors must be calibrated and characterized in order to extract useful gamma-ray energy spectra. Proper calibrations for both the central contacts and segments are vital for the detectors to function as a single array since the signals in each ring of detectors were summed together. Furthermore, energy calibrations are vital to correlate the charge pulse from a detected gamma ray with the true photon energy (and thus the nuclear transition energy). Here, the procedure for calibrating all 480 segments and 15 central electrodes is outlined.

---

[6] The θ designation of each ring is the angle between the beam axis and the line segment connecting the S800 target position to the crystal midplane. Thus, the cylindrical symmetry axis of detectors in a $\theta = 90^\circ$ ring would lie parallel to the beam axis.

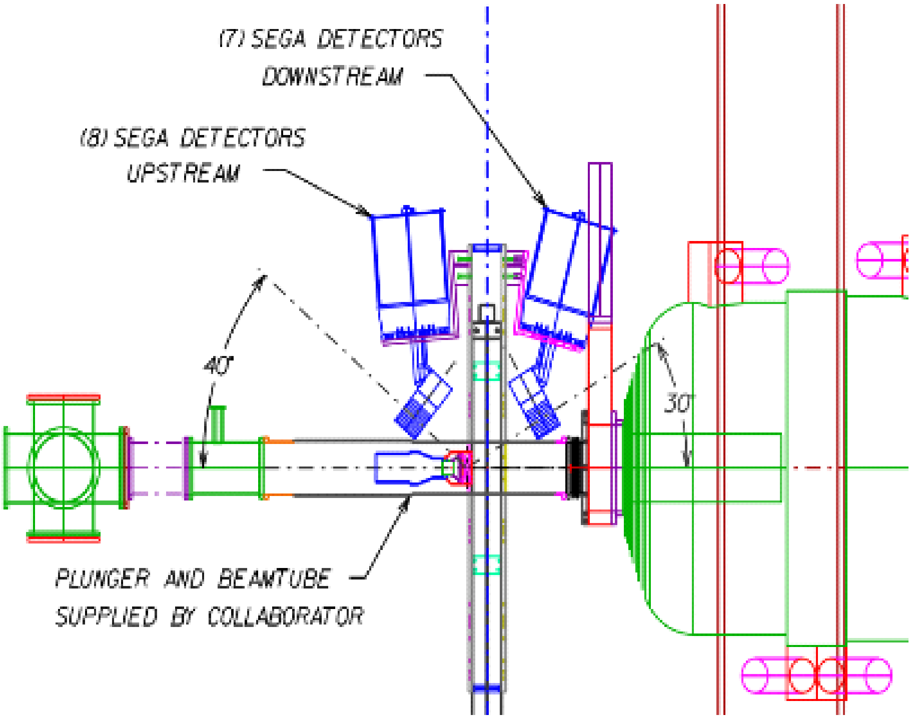

Figure 2.10: The experimental setup for the ^{18}C experiment. Only the $\phi = 0°$ SeGA detectors are shown at forward and backward ring angles of 30° and 140°, respectively. The plunger is aligned in the beam pipe with the upstream face of the degrader corresponding to the $z = 0$ S800 target position.

The first step is to calibrate all 15 central electrode channels against one another. This was done by matching the detector response to a ^{226}Ra source with the known energy transitions from that source. The goal of the calibration was to align the detected photopeaks from each detector with one another such that the peaks fell into the same histogram bins which corresponded to the correct transition energies. The calibration of each central contact was automated—the raw data histograms were read into the histogram and analysis software gf3 (Subsect. 2.4.1), a source file containing the known transition energies for ^{226}Ra was loaded, the peaks in the uncalibrated histograms were marked by the analyzer, and the data were fit to the source information by a χ^2 minimization of a second order polynomial. From this, three calibration parameters for the central contact of each detector were obtained.

Next, the individual segments must be calibrated to the calibrated central contact of each detector. This can quickly become a very complicated procedure; the set of three calibration coefficients are dependent upon the number of segments that participated in a given gamma-ray event (known as the multiplicity or fold for the event). Thus, a given segment will have a set of three fold-1 calibration parameters, 31 sets of three fold-2 calibration parameters (corresponding to the 31 possible segment combinations for fold-2 events), and so on. The procedure has been largely automated [88] and is described in brief below for a single detector.

First, the fold-1 subset of data was selected. There should be a one-to-one correspondence between the energy signal in the only active segment and calibrated central contact. This correspondence is independent of whether the detector signal resulted from partial or full gamma-ray absorption; data from the Compton continuum is as useful as that from the photopeak. A χ^2 minimization was used to extract 32 sets of fold-1 calibration parameters from a second order polynomial fit (one set for each segment). Next, the fold-2 subset of data was selected and in a similar manner, fold-2 calibration parameters were extracted by the one-to-one correspondence between the summed calibrated energy signals of the two active segments and the central contact. Thus, for fold-2 events a total of $32 \times \frac{31}{2}$ sets of calibration parameters were extracted from the χ^2 minimization of a pair of second order polynomials (6 correction coefficients total per set, three per segment).

For higher-order folds, the number of parameter sets grows with the possible combinations and the number of parameters in a set grows linearly. Therefore, the calibration for segments with folds larger than 2 were done not by fitting, but by applying a higher-order fold correction as given by

$$\begin{aligned} E^f &= \sum_{i=1}^{f} E_i^1 + \sum_{i=1}^{f} \sum_{j=i+1}^{f} \alpha_{i,j} + \frac{(f-1)(f-2)}{2}\xi \\ \alpha_{i,j} &= E_{i,j}^2 - E_i^1 - E_j^1. \end{aligned} \tag{2.8}$$

Here, E^f is the calibrated energy for segments with fold $f > 2$, E_i^1 is the calibrated fold-1

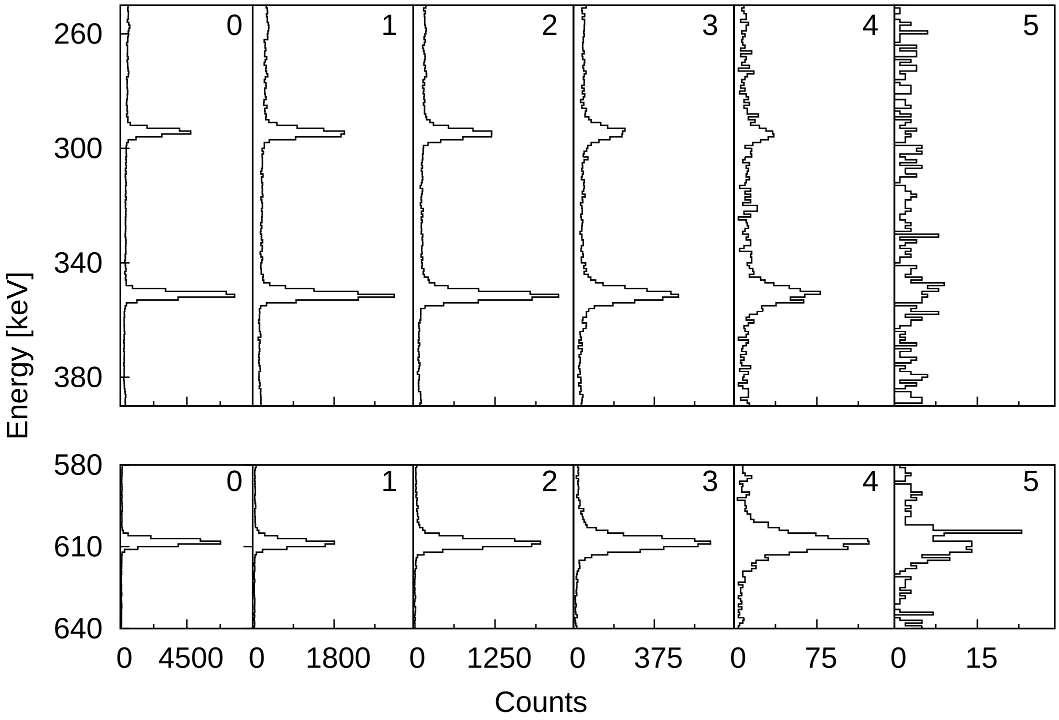

Figure 2.11: Subset of calibrated ^{226}Ra gamma-ray energy spectra from the central contact (panels 0) and segments with increasing event fold data from fold-1 to fold-5 (panels 1-5) of a single SeGA detector for the 295.2, 351.9, and 609.3 keV transitions. The calibrated energies for folds greater than two (panels 3-5) are given by Eq. 2.8.

energy for segment i, $E^2_{i,j}$ is the calibrated fold-2 energy for a segment pair i, j, and ξ is a fitting parameter for each detector that was generally found to be between 2 and 3 keV. The result of the calibrations is shown in Fig. 2.11. The degradation in energy resolution for higher folds is to be expected as the correction of Eq. 2.8 becomes a less and less accurate approximation. The prominent decrease in statistics for events of fold-3 or higher mitigates the effect of worsening resolution.

Photopeak Efficiency Calibration

For the presented work on ^{18}C, the lifetime information is extracted from the ratio of counts in the two photopeaks as a function of target-degrader distance. Since this is a relative measurement, determining the energy-dependent photopeak efficiency of the Segmented Germanium Array is not a vital task *per se*. However, the photopeak efficiency strongly depends upon the characteristics of the experimental setup such as the intrinsic detection efficiency of the germanium crystals, the solid angle coverage of the array, the photon energy, and the presence of absorbing materials such as the beam pipe, the aluminum casing of the detectors, and the plunger target and degrader support structures. Therefore, measuring the efficiency with a standard radioactive source can reveal weaknesses in the experimental setup and indicate where future design improvements must be made. More importantly, the experimentally determined photopeak efficiency provides a stringent verification of the analysis simulation software's ability to reproduce the experimental materials and setup, geometry, and gamma-ray attenuation. The simulation software is introduced in Subsect. 2.4.2 and discussed in detail in Ch. 3.

The placement of the Köln/NSCL plunger in the beam pipe introduces a loss of efficiency since the target and degrader material, along with the aluminum supporting structures, shadow the SeGA detectors. It is therefore expected that the efficiency measured with a radioactive source placed in an empty beam pipe will be larger than that of the experiment, where the plunger materials attenuate the gamma-ray flux. Section C.2 of Appendix C discusses gamma-ray attenuation in greater detail. To accurately determine the gamma-ray photopeak efficiency for the ^{18}C measurement, data were collected with standard gamma-ray sources inserted between the 1.1 mm plunger beryllium target and 1.2 mm tantalum degrader. ^{152}Eu (measured activity of 8.46 μCi on May 1st, 1978) and ^{226}Ra (measured activity of 9.93 μCi on August 1st, 1975) sources were used. The ^{226}Ra source emits gamma rays in an energy range from approximately 186 keV to 2448 keV. The corresponding range of energies from the ^{152}Eu source is 122 keV to 1408 keV.

The transition of interest in the ^{18}C experiment was Doppler shifted to over 2100 keV in the forward ring SeGA detectors (see Eq. B.24 of Appendix B) and thus the ^{226}Ra source was needed to probe the efficiency at such high energies. The alpha-decay half-life of ^{226}Ra is 1600(7) years. This imprecision results in an uncertainty in the current radioactivity calculated from the manufacturer's measured activity. In contrast, the beta-decay half-life of the ^{152}Eu ground state is precisely known to be 13.537(6) years. Thus, to obtain an absolute efficiency calibration from both sources, the relative efficiency measured with ^{226}Ra source data was scaled by the efficiency ratio of the two sources calculated from transitions of similar energies near 240, 350, 770, and 1120 keV. The energy-dependent absolute photopeak efficiency (in %), $\epsilon(E)$, is given by

$$\epsilon(E) = 100 \cdot \frac{N(E)}{A \cdot T \cdot P(E)}. \tag{2.9}$$

Here, $N(E)$ is intensity of the photopeak of energy E, A is the source disintegration rate (in Becquerels, or decays per second), T is the live-time duration of the measurement (in seconds), and $P(E)$ is the probability of a gamma-ray emission of energy E per decay (obtained from [89]).

The forward 30° and backward 140° SeGA ring photopeak efficiency curves are presented in Fig. 2.12. The efficiency is markedly higher in the backward ring because of its larger solid angle coverage afforded by having more detectors and being installed closer to the S800 target position, corresponding to the source location (8 detectors compared to 7 and 23.3 cm compared to 30.3 cm for the backward and forward rings, respectively.) In the forward ring, gamma-ray attenuation through the thick tantalum plunger degrader diminishes the steep increase in efficiency with decreasing photon energy observed in the backward ring and is responsible for the sudden inflection of the efficiency curve near 300 keV. From the plot, the summed absolute photopeak efficiency of the Plunger SeGA experimental setup for a 1 MeV photon emitted at rest is approximately 1.9%.

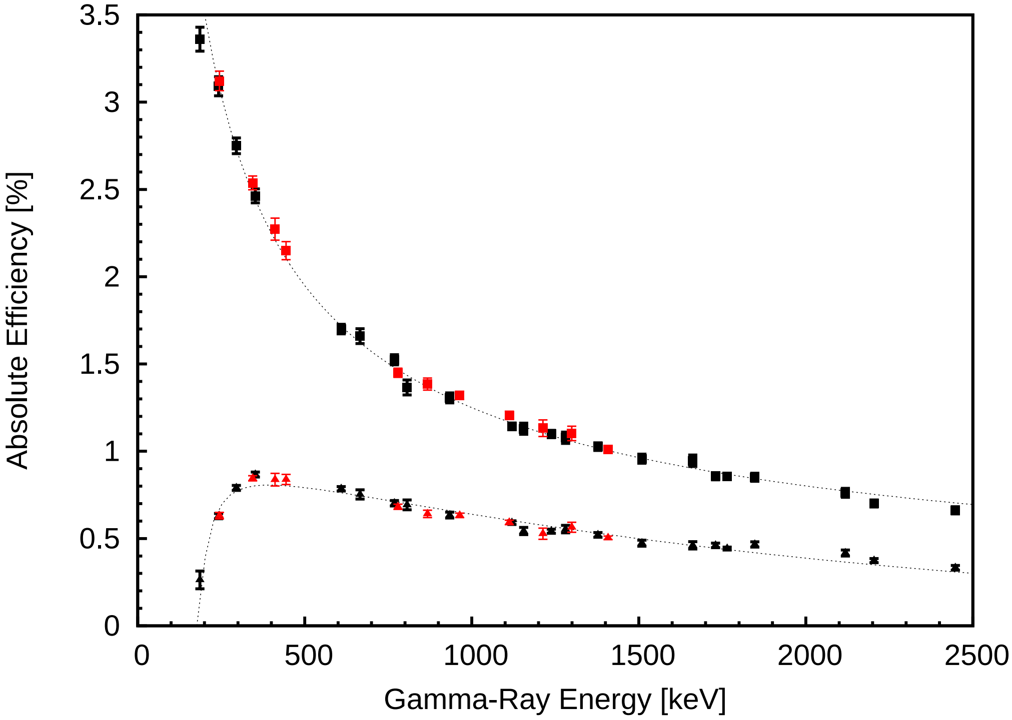

Figure 2.12: SeGA photopeak efficiency curves for the 30° ring (triangles) and 140° ring (squares) from ^{152}Eu (red) and ^{226}Ra (black) source data. The functional forms of the fits (dashed lines) were chosen phenomenologically and used to extract the in-beam photopeak efficiency for the transition of interest after correcting for the gamma-ray intensity asymmetry introduced by the relativistic Lorentz boost (see Ch. 3).

DDAS

The ^{18}C measurement marked the first experiment at NSCL to fully instrument SeGA with a complete array of digital electronics. The Digital Data Acquisition System (DDAS) was developed at NSCL to enable the waveform capture and pulse shape analysis of segmented radiation detectors. A more in depth discussion of DDAS can be found in [88] and references therein. Here, the more salient features are discussed.

The signal pulse arising from a detected gamma ray in SeGA contains vital information about the energy, timing, and position properties of the interaction. In order to fully extract all of this information on an event-by-event basis, it is necessary to capture and store the detected gamma-ray waveforms. Since the timing and interaction position information is extracted from the rising edge of the signal, it is crucial to sample the waveform on a very fine scale (relative to the rise time) to preserve the smooth, continuous nature of charge collection. DDAS was designed and built to capture waveforms of a user-defined length with a 100 MHz sampling rate and to perform pulse shape analysis of the signals extracted from all 594 electronic channels of the full 18-detector Segmented Germanium Array.

The Digital Data Acquisition System architecture is designed around the 16-channel Pixie-16 Digital Gamma Finder module. Each Pixie-16 module contains on-board computing systems to control synchronous waveform capturing and digital pulse processing for 16 input channels as well as module-to-module communications on a single-width PXI card. A 12-bit 100 MHz Flash Analog to Digital Converter is allocated to each input channel which facilitates the simultaneous analysis of up to 16 independent signals on a single card. The cards are housed inside four Compact PCI/PXI 14-slot crates. Each crate is controlled via an optical fiber bridge by a dedicated Linux-based PC server and a fifth server is designated for event building. All five PC servers are connected to a 10 TB data storage array over a fast Gigabit network. Together, the Pixie-16 modules, PCI/PXI crates, PC servers, and storage array constitute the full Digital Data Acquisition System.

There are a total of 39 Pixie-16 modules installed in DDAS to fully instrument the central contacts and segment electrodes of all 18 SeGA detectors. Their 16-channel input design drives a natural separation of the roles each card plays. A pair of cards (the Manager and Worker) are required to serve the 32 segment signals from a single detector. Six Manager/Worker pairs, and thus 6 detectors, are housed in each of three PCI/PXI crates. The fourth PCI/PXI crate houses the remaining three cards—a pair of Assistants which each serve 9 central contact signals in channels 0-8 and any potential auxiliary detector signals in channels 9-15, and the Director which is responsible for receiving and distributing trigger information. All 39 cards have identical hardware and firmware; their unique roles are designated by a set of circuit board jumpers and configuration software parameters that are loaded upon system initialization. This design grants the system maximum flexibility in the event of a module failure (for Plunger SeGA, only 15 detectors are used and therefore there are spare cards) or to accommodate different experimental needs.

If a gamma-ray interaction within a SeGA detector produces a charge pulse that rises above a user-defined energy threshold, several conditions must be met and tasks completed before the resulting waveform can be written to disk. The process begins with the above-threshold signal on one of the Assistant module channels. The active Assistant then communicates the presence of the event via a logic pulse sent through the PCI/PXI crate backplane to the Director. This pulse prompts the Director to open a coincidence window of user-defined length and compute the event multiplicity based upon how many logic pulses it receives from the Assistants within the coincidence window. If the computed multiplicity satisfies the user-preset condition, the Director performs the actions outlined below.

- First, a validation window of a user-defined length is opened. The Director must receive an external validation pulse within this window for the gamma-ray event to be written to disk. This validation window signal is sent to the S800 analog electronics setup via an optical fiber link. If the timing difference between the validation pulse and a reaction residue signal from the S800 E1 scintillator falls within the S800-controlled coincidence window, a master coincidence trigger is issued by the S800 electronics. This coincidence trigger initiates the writing of the S800 reaction residue analog data to disk and also serves as the external validation pulse for DDAS. (So the master trigger for the ^{18}C experiment required the coincident detection of one reaction residue and at least one gamma ray.)

- While the validation window is still open, the Director sends out a global fast trigger to all DDAS Pixie-16 modules. This trigger initiates synchronous waveform capturing and latches a time stamp provided by the 100 MHz DDAS clock that is common to all

Pixie-16 modules.

- The fast trigger is immediately proceeded by a hit pattern that indicates which modules are to store the captured waveform data if the external validation pulse is received by the Director. This hit pattern is based upon which Assistant channels sent event-detected logic pulses within the coincidence window. Both the fast trigger and hit pattern are distributed from the Director module to all other modules via a system of equal length CAT-6 cables and Low Voltage Differential Signaling (LVDS) fanout modules. Figure 1 of Ref. [90] illustrates this trigger/hit pattern distribution system.
- Finally, the arrival of the external validation pulse from the S800 trigger electronics prompts the Director to send out a record trigger signal. Upon receiving the record trigger signal, those modules indicated by the hit pattern assemble a data file with a header and energy, timing, and waveform information.

For a given event, up to 39 module event files can thus be written to the storage array. In order to assemble these individual module files into a single analysis-ready data file, two steps are taken. First, a single DDAS event is assembled from the individual module events by merging together those events that share a common DDAS time stamp and event number. This module event merging is done after the experimental run is completed on the fifth PC server and takes less than a minute total. Next, the complete DDAS digital run file is merged with the S800 analog run file. To do this, a copy of the digital data stream must be reduced to an equivalent analog data stream by retaining detector, segment, energy, and timing information, but removing stored waveforms. This reduced digital data stream is then merged with the S800 analog data stream on an event-by-event basis by another time stamping routine. For the presented ^{18}C experiment, a 48-bit counter was set up on the Director module and the S800 electronics rack. A common 1 MHz pulser was then sent to each counter; the counters were latched by the coincidence trigger (external validation pulse).

At the conclusion of an experimental run, the reduced digital and analog data streams were merged based upon common time stamps.

This merging method proved to be reliable and robust. Merging failures occasionally occurred and were often caused by missing data from the Assistant module; in all but a small handful of cases this issue was rectified. It is worth mentioning that both the original analog data and full digital data for each run are preserved, allowing remerging after the experiment or after an upgrade to the merging software. Finally, since an analog-equivalent data file necessary for real time experimental analysis was not available until the completion of the run, several analysis programs were developed to examine the data on the level of individual module events online, including displaying waveforms and creating and plotting module-specific energy histograms.

2.4 Analysis Software

Many software analysis tools exist at NSCL from which polished final results are extracted from raw experimental data. All of the run sorting, particle gating, and data reduction for the analysis of the ^{18}C and ^{19}Mg experiments was done with a collection of analysis code written in both C and C++. The code structure was similar from one task-specific program to the next—read in the data file (either the entire raw event file or a reduced data file), load and apply any pertinent calibration or correction parameters, apply any gating requirements, and output the results as a reduced data file or sorted histogram. During production runs, raw data was written to disk when a reaction residue was detected in the focal plane of the S800 (as in the ^{19}Mg experiment) or when a coincidence between a gamma-ray event in SeGA and a reaction residue in the S800 focal plane was registered (as in the ^{18}C experiment). Therefore, raw data contains events that originate from all of the secondary beam components that impinge upon the target and produce a reaction residue which falls within the momentum acceptance of the S800 spectrometer.

To take advantage of the opportunity to analyze data from several incoming beam components and outgoing reaction residues, the analysis code was designed to sort the initial raw data into various packets based upon the identification of incoming and outgoing beam components on an event-by-event basis. This data file segmentation also improves the signal-to-noise ratio of experimental spectra by removing events from contaminant beams and reaction residues. For example, the final data file from which a ^{18}C gamma-ray spectrum is obtained is greatly reduced from the original raw data file by first removing events arising from incoming beam contaminants and then eliminating from the remaining events those attributable to contaminant reaction residues in the S800 focal plane. Working with progressively smaller data files inherently speeds up the analysis. Furthermore, new calibration or correction parameters can be applied to only a specific data packet; the entire raw data file need not be resorted.

Typically, the sorting programs output calibration and correction parameters or raw and calibrated spectrum files. The output spectra are read, manipulated, and saved for display using either ROOT [91] or gf3 [92]. For the presented analyses, the final gamma-ray and DSSD energy loss spectra were passed to a Geant4/ROOT Monte-Carlo simulation software package built upon the ROOT and Geant4 [93] toolkits. Both of these programs are well documented with extensive online support and implementation examples; therefore the following two subsections are devoted to describing the gf3 histogramming software and the Geant4/ROOT simulations in brief detail.

2.4.1 Data Histogramming with gf3

In the presented analyses, the gf3 histogramming program from the RadWare software package was used almost exclusively for interactive graphical analysis of one dimensional histograms. These histograms were used for the analysis of SeGA gamma-ray spectra, particle plunger DSSD and S800 ionization chamber energy loss spectra, and CRDC x- and y-position spectra, among others. The data from these spectra are stored as unformatted integers in 4096 channels with 4 Bytes per channel. gf3 has many analysis features including spectra manipulations such as zooming, contracting, peak fitting, background parameterizing, and energy calibrating. Various histograms can be overlayed on top of one another or stacked for comparison. Manipulated histograms can be saved or printed as postscript files.

At its heart, gf3 is a peak-fitting program that allows for the simultaneous fitting of up to 15 peaks on a quadratic background. The main component of the fitted peak is a Gaussian that can be convoluted with a skewed Gaussian to account for incomplete charge collection in the detector, which results in a low energy exponential tail. A smooth step function on the low energy side of the peak can also be added for fitting gamma-ray spectra to account for the Compton scattering of events from one detector into another. The user has control over the parameters used to describe the peak shape and background. Parameters may be iteratively determined given initial estimates or simply fixed via a start-up script or command line prompt. The number of iterations to achieve convergence can also be controlled.

2.4.2 The Geant4/ROOT Simulation Package

The lifetime determinations reported in the subsequent two chapters were done by matching simulated detector lineshapes produced with various input lifetimes to the experimental spectra obtained at various plunger distances. In order to produce accurate detector lineshapes that can be reliably fit to experimental data, the simulations must reconstruct all pertinent experimental details within the Geant4 framework. The lifetime is then determined by the best fit via χ^2 analysis within ROOT. This method of analysis has been tested and described in detail in Ref. [94]. Chapters 3 and 4 describe the specific steps which brought the simulation to full complexity for the lifetime analyses. What is important to note here is that the simulated lineshapes are dependent upon the detector system and plunger geometries, the spatial extent and energy spread of the secondary beam, the reaction kinematics, and the acceptance settings of the S800. For both analyses, the geometry of the experimental setup, the phase space of the incoming secondary beam, the knockout kinematics and subsequent energy and angular straggling of the reaction residues, and the decay and detection processes were all accurately modeled within Geant4. ROOT was used to carry out the χ^2 analysis of the simulations' fit to data, display and manipulate histograms, and provide a convenient tree structure to access various histogrammed results.

The Geant4 and ROOT toolkits were seamlessly combined within G4UIROOT, which formed the backbone of the simulations. As its name implies, the G4UIROOT program provided a graphical user interface (GUI), built with ROOT, for simulations performed by Geant4. G4UIROOT allows the user to access and browse all Geant4 commands in a conveniently organized file system structure. Figure 2.13 shows several of the various on-screen windows available to the user during a simulation: the main GUI where commands are accessed or macro scripts can be executed, a tree viewer from which different result histograms can be directly accessed, and error and output message windows. In GUI mode, the terminal provides the ROOT command line which is useful for modifying the output histograms generated at the completion of a simulation. The program can also run silently in batch mode in the background. This is extremely useful in the final stages of analysis, where all simulation parameters are constrained and the lifetime determination requires long simulations run from a script which increments the input lifetime and plunger distance.

Finally, as noted in Subsect. 2.3.2, this simulation package proved useful in the preparation of RDM lifetime experiments, especially regarding the choice of plunger degrader material and thickness. The choice of target material and thickness are largely motivated by considerations concerning the reaction mechanism and experimental yield and can be predicted with LISE++ [95]. However, the choice of degrader material and thickness can be investigated by generating simulated lineshapes using various combinations and examining

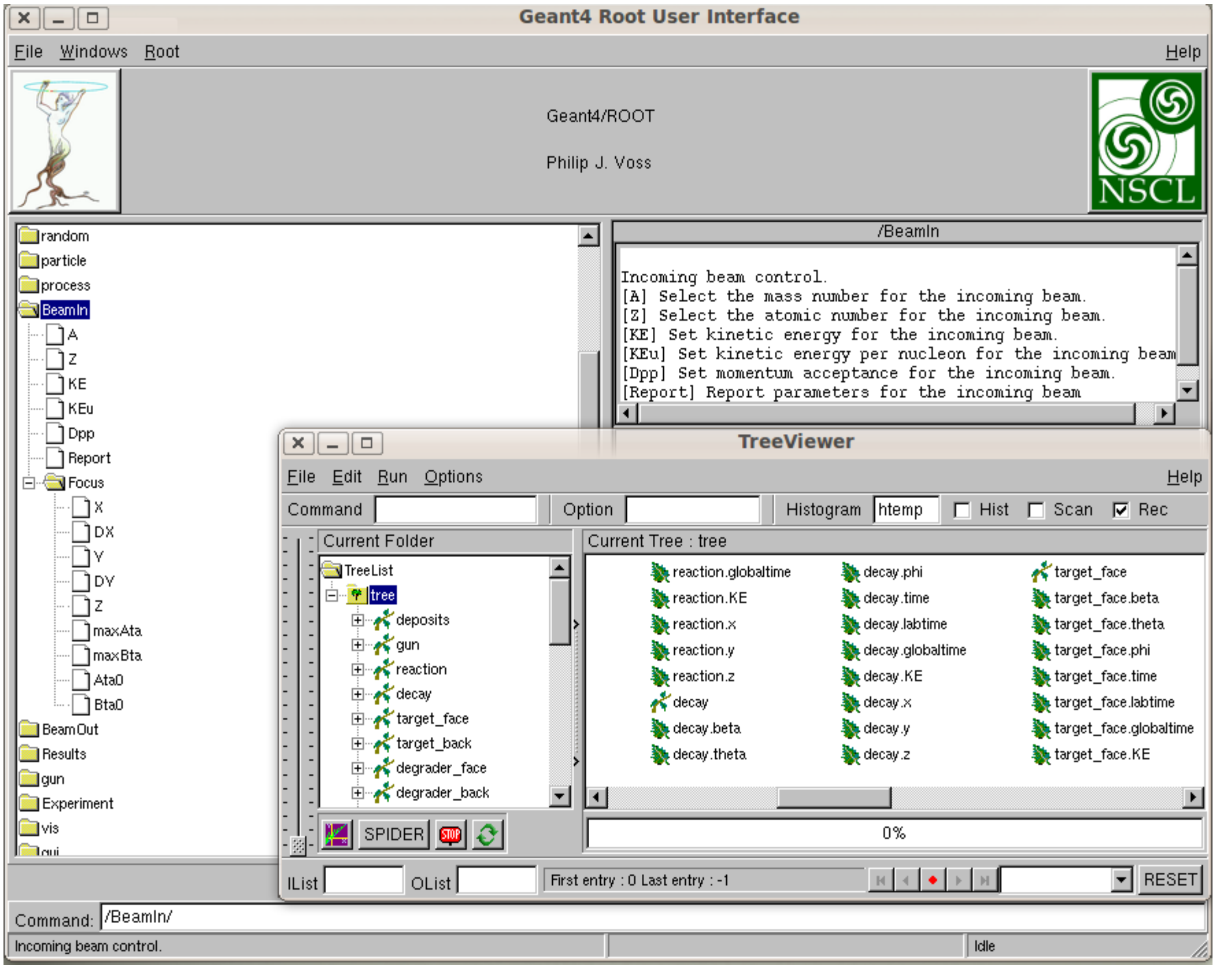

```
Incoming beam control.
[A] Select the mass number for the incoming beam.
[Z] Select the atomic number for the incoming beam.
[KE] Set kinetic energy for the incoming beam.
[KEu] Set kinetic energy per nucleon for the incoming beam
[Dpp] Set momentum acceptance for the incoming beam.
[Report] Report parameters for the incoming beam
```

First entry : 0 Last entry : -1

Command: /BeamIn/

Incoming beam control.

Figure 2.13: A screenshot of the Geant4/ROOT simulation user interface illustrates several of the GUI features of the program. All experimental commands can be accessed from the main GUI window. A tree viewer provides convenient access to many different histograms of the simulation results. Not pictured are the simulation output and error message windows or the visualization window which draws the experimental setup and provides tracking of each event. This last capability is computationally intensive and was not used in the analysis.

the resulting peak separation between the fast and slow gamma-ray decay photopeaks. The lifetime of the state of interest should also be varied; very short lifetimes in thick target materials will decay in target rather than in vacuum and therefore the energy resolution will worsen from velocity uncertainties in the Doppler reconstruction. Such material and thickness considerations were investigated using Geant4/ROOT simulations while preparing the ^{18}C experimental proposal.

Chapter 3

Lifetime Measurements in ^{18}C

The Köln/NSCL plunger lifetime measurement of the $2_1^+ \rightarrow 0_{gs}^+$ transition in ^{18}C was part of an experimental campaign investigating the collectivity and nuclear shape evolution of the neutron-rich carbon isotopes ^{16,18,20}C. As shown in Ch. 1, the reduced quadrupole transition matrix element $B(E2; 2_1^+ \rightarrow 0_{gs}^+)$ is inversely proportional to the lifetime. This $B(E2)$ transition strength is a measure of the degree of quadrupole collectivity of the nucleus and thus lifetime measurements of electromagnetic transitions in radioactive nuclei are useful and simple probes of nuclear structure. The lifetime investigation was carried out at the National Superconducting Cyclotron Laboratory via the application of the Recoil Distance Method lifetime technique applied to the ^{9}Be(^{19}N, ^{18}C*)X one-proton knockout reaction in inverse kinematics. This technique has been successfully applied to lifetime measurements in many different regions of the nuclear chart at NSCL [20–22, 78, 79] and has proven to be a reliable experimental method requiring minimal theoretical model dependence during analysis.

The lifetime of the $2_1^+ \rightarrow 0_{gs}^+$ 1585 keV transition in ^{18}C was determined to be $\tau = 22.4 \pm 0.9(\text{stat})^{+2.5}_{-1.6}(\text{syst})$ ps, which is in agreement with the literature value of $\tau = 18.9 \pm 0.9(\text{stat}) \pm 4.4(\text{syst})$ ps [29]. This corresponds to a reduced quadrupole transition matrix element value of $B(E2) = 3.64^{+0.46}_{-0.48}$ e^2fm^4 using Eq. 1.9. A 932 keV transition was observed to feed the 2_1^+ state from above. The statistics for this state with unassigned spin and parity were sufficient to set a lifetime upper limit of 4.5 ps. This is the first quantitative lifetime information measured for a state above the first 2^+ for even-even carbon isotopes with $N > 8$. The experimental technique and detector characterization were presented at length in Ch. 2. The present chapter details the experimental measurement, the data analysis, and the subsequent experimental results.

3.1 Experimental Considerations

The Geant4/ROOT simulation software described in Subsect. 2.4.2 proved to be a powerful analytic tool for extracting the lifetime from the ^{18}C RDM measurement. It was able to accurately simulate the experimental setup, the secondary beam emittance, the one-proton knockout kinematics and subsequent energy and angular straggling of the ^{18}C nuclei, and the gamma-ray decay and detection processes—including the Doppler broadening of the detected photopeaks, the asymmetric Lorentz boosted gamma-ray intensity distribution in the laboratory frame, and the gamma-ray detection efficiency. Such a complete description of all facets of the experiment required many input parameters. Properly constraining all of these parameters necessitated the collection of a unique combination of experimental data.

- First, standard gamma-ray radioactive source spectra were collected before and after the experiment for the energy and photopeak efficiency calibrations of SeGA (discussed within Subsect. 2.3.4). Comparing the simulated and experimental source photopeak efficiencies verified the proper implementation of the SeGA geometry, gamma-ray attenuation and detection processes, and the detector response within the simulation.

- In addition to SeGA calibrations, several in-beam calibrations for the S800 CRDCs and IC were performed. The calibration procedures were discussed in detail within Subsect. 2.3.3. Three CRDC mask calibrations were performed over the course of the experiment by sweeping the ^{19}N secondary beam across the entire focal plane. The reaction residues within the momentum acceptance of the S800 were also used for calibrations. Their energy loss signals in the ionization chamber were used to energy calibrate its sixteen channels.

- Prior to the insertion of the Köln/NSCL plunger, the ^{19}N secondary beam was delivered unimpeded to the S800 focal plane. The data constrained the simulation parameters describing the secondary beam emittance at the target position of the S800. From the calibrated angles and positions in the CRDCs and the S800 rigidity settings, the experimental spectra of the four S800 target parameters (a_{ta}, b_{ta}, y_{ta}, and d_{ta}) were produced by inverse map trajectory reconstruction. The simulation parameters were set by fitting the corresponding simulated spectra to these experimental counterparts.

- Next, the target-only plunger was inserted and the energy and angular straggling of the ^{19}N secondary beam transported through the beryllium target was studied. To preclude contributions from nuclear reactions, the S800 was tuned to accept only unreacted ^{19}N beam ions. As above, the simulated target-only S800 target parameter spectra were fit to their experimental counterparts and the simulation parameters describing energy and angular straggling were fixed to appropriate values.

- The S800 was then tuned to accept ^{18}C reaction residues and the data acquisition trigger was set for particle-gamma (S800-SeGA) coincidences. This target-only reacted beam data provided straightforward information on the relative population of different excited states in ^{18}C. It also constrained the simulation parameters required to describe the proton knockout reaction and its effect on the momentum distribution of ^{18}C by comparing the simulated a_{ta}, b_{ta}, y_{ta}, and d_{ta} reacted target-only beam spectra to their experimental counterparts.

- Finally, with the data taken to both calibrate the experimental equipment and facilitate the accurate parameterization of the experimental conditions in the simulation code, the tantalum degrader was installed and the full plunger was inserted. To account for the energy loss through the degrader, the S800 was retuned to accept ^{18}C reaction residues. The simulation parameters describing the spread in momentum and angular straggling introduced by the degrader were constrained by fitting the simulated full-plunger S800 target parameter spectra to their experimental counterparts. Figure 3.7 within Subsect. 3.3.1 illustrates the quality of the fit between the experimental data and the fully constructed reaction residue simulation.

3.2 Experimental Details

The remaining experimental data were taken with the full plunger apparatus, a particle-gamma coincidence trigger, and the S800 tuned to accept ^{18}C reaction residues. Gamma-ray energy spectra were collected at five target-degrader distances of 0.0, 600.0, 1500.0, 2200.0, and 3000.0 μm in coincidence with reaction residues in the S800. The details concerning the incoming secondary beam, outgoing reaction residues, and observed gamma-ray de-excitations follow.

3.2.1 Radioactive Secondary Beam

The delivery of the secondary beam to the Köln/NSCL plunger target involved the development, acceleration, and fragmentation of a ^{22}Ne primary beam and the subsequent selection and purification of the ^{19}N component. The method and devices employed were discussed in detail in Sect. 2.2.

The Coupled Cyclotron Facility at NSCL accelerated a primary beam of $^{22}\mathrm{Ne}^{+10}$ to 120 MeV/u ($\approx$ 46% the speed of light, or $\beta = v/c = 0.46$) with an average intensity of roughly 150 pnA. Following acceleration, the beam was delivered to a 1763 mg/cm^2 ($\approx$ 9.5 mm

Table 3.1: ^{19}N secondary beam characteristics. $B\rho$ and $\Delta p/p$ were taken from the experimental beam line savesets provided by the A1900 Fragment Separator Group. The beam energy was calculated from $B\rho_{3,4}$. The ^{19}N average rate and transmission to the S800 were calculated from run-by-run scaler information while the purity was calculated from integrating the peaks of Fig. 3.1.

B$\rho_{1,2}$	3.59090 T · m
B$\rho_{3,4}$	3.46591 T · m
Final Energy	75.46 MeV/u
$\Delta p/p$	0.7%
Average Rate	2000 pps/pnA
Purity	97.7%
Transmission to S800	82%

thick) ^{9}Be production target. From the resulting fragmentation reaction products, the ^{19}N secondary beam was selected by the A1900 Fragment Separator. The settings of the A1900 were optimized for transmission and purity of ^{19}N. In particular, the momentum acceptance was restricted to 0.7% with momentum apertures installed at Image 1 and 2 (refer to Fig. 2.1). A 300 mg/cm^2 Al energy degrading wedge at Image 2 was used for additional contaminant separation. The desired ^{19}N radioactive secondary beam emerged from the A1900 with better than 97% purity. The remaining beam contaminants, ^{17}C and ^{21}O, were distinguished from the ^{19}N fragment of interest by their time of flight between 1 mm thin plastic scintillators at the A1900 focal plane and the object position of the S800. The properties of the secondary beam are listed in Tab. 3.1. There, the subscripts refer to the four A1900 dipole magnets.

The magnetic rigidities of the final two A1900 dipole magnets were set to deliver the ^{19}N secondary beam at 75.46 MeV/u to the plunger at the S800 target position. The beam rates emerging from the A1900 and entering the S800 were monitored during the experiment by the plastic scintillators. Throughout the experiment, the secondary beam intensity at the A1900 focal plane was above 3.1×10^5 pps and the transmission losses en route to the S800 were less than 20%. Figure 3.1 shows the time of flight of the secondary beam components during a run where the unreacted secondary beam was delivered to the S800 focal plane;

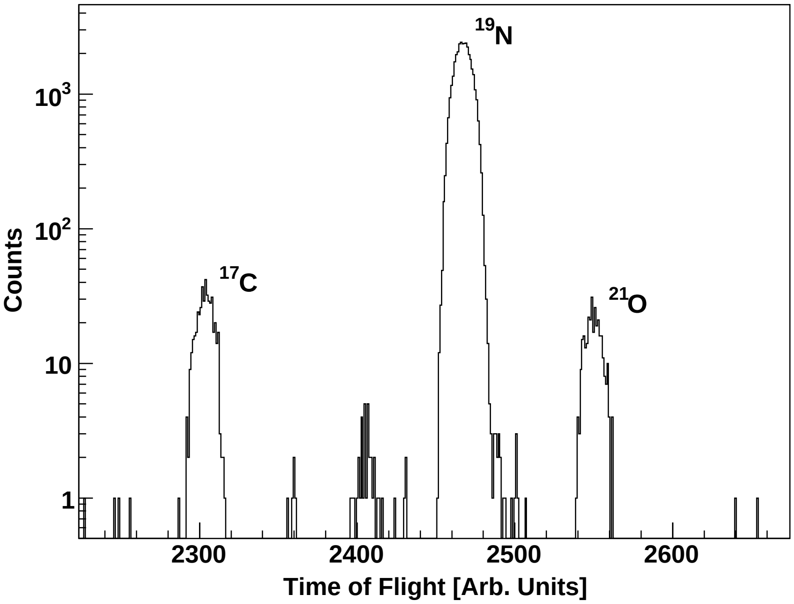

Figure 3.1: Identification of the secondary beam components by their time of flight between two thin plastic scintillators at the A1900 focal plane and object position of the S800. Note the logarithmic scale of the ordinate. Increasing time is from right to left along the abscissa.

the clear separation between ^{19}N and the ^{17}C and ^{21}O contaminants allowed for offline separation during the analysis.

3.2.2 Outgoing Reaction Residues

The ^{19}N secondary beam was sent to the S800 Spectrometer. The experiment utilized the S800 in focused mode; the beam was focused at the object position of the S800 and the analysis line delivered a focused beamspot onto the ^{9}Be 196 mg/cm^2 ($\approx$ 1.1 mm thick) Köln/NSCL plunger target. States in ^{18}C were populated by the one proton knockout reaction of ^{19}N on the beryllium target. The magnetic rigidity of the spectrograph was set to $B\rho = 2.83$ T $\cdot$ m to maximize the acceptance of ^{18}C and reject unreacted ^{19}N and other reaction contaminants.

For full-plunger production runs, the ^{18}C reaction residues emerged from the target with a velocity distribution centered at $\beta_{fast} = v/c = 0.3565(5)$. After a specified flight distance, the ^{18}C nuclei were slowed in the $^{\text{nat}}$Ta 2010 mg/cm^2 ($\approx$ 1.2 mm thick) degrader to a final velocity distribution centered at $\beta_{slow} = 0.2920(5)$. For target-only production runs, the ^{18}C reaction residues emerged from the target with a velocity distribution centered at $\beta'_{fast} = 0.3610(5)$. The difference between β_{fast} and β'_{fast} is strictly due to small variations in the momentum acceptance from tuning discrepancies of the S800 rigidity for data taken with and without the tantalum degrader. The *true* momentum distribution of ^{18}C as it emerges from the target is identical regardless of whether the degrader is present or not; the *observed* momentum distribution upstream of the degrader is affected by the acceptance settings of the S800. The procedure for determining the beam velocity and its uncertainty is mentioned in Sect. B.2 of Appendix B.

The knockout reaction residues within the acceptance of the S800 were identified on an event-by-event basis by their energy loss through the ionization chamber and time of flight between the object position and E1 focal plane scintillators. The clear separation between the ^{19}N knockout reaction residues accepted by the S800 is illustrated in Fig. 3.2. The subset of events plotted were selected by a run-by-run software gate on the ^{19}N peak in the secondary beam time of flight spectra. In order to achieve the level of separation in the particle identification plot, the ionization chamber channels were calibrated and flight-path corrections were applied to the energy loss and time of flight signals using focal plane angle and position information determined from the calibrated CRDCs. These trajectory corrections were described within Subsect. 2.3.3.

3.2.3 Observed Gamma-Ray Transitions and Analysis

Doppler shifted de-excitation gamma rays were measured with the Segmented Germanium Array in coincidence with reaction residues in the S800. The experiment utilized the Plunger SeGA configuration with 15 detectors surrounding the plunger in two rings at laboratory

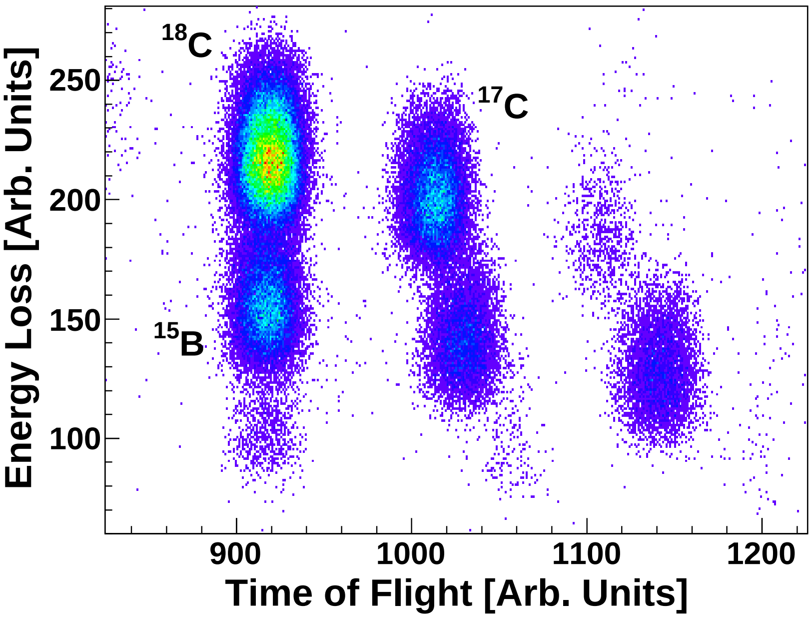

Figure 3.2: Identification of the outgoing reaction residues from the incoming ^{19}N secondary beam by time of flight and energy loss information from the S800 Spectrometer. Increasing time is from the right to left along the abscissa.

angles of 30° and 140° with respect to the beam axis. The electronics trigger was issued upon the coincident detection of a reaction residue in the S800 E1 scintillator and a gamma ray in SeGA within 600 ns of one another (discussed in detail within Subsect. 2.3.4). This coincidence requirement significantly reduced background contaminants in the gamma-ray spectra resulting from ambient sources and gamma-ray transitions from fragmentation contaminants that were not accepted by the S800. Further background suppression was achieved in the analysis by incoming ^{19}N and outgoing ^{18}C software particle gates. These gates rejected events that originated from secondary beam contaminants or undesired reaction channels that had similar momenta to ^{18}C and therefore were transmitted to the S800 focal plane. The enhancement in the signal-to-noise ratio (S:N) of gamma-ray spectra provided by software gating is illustrated by Panel 3 of Fig. 3.3, where Doppler reconstructed gamma-ray spectra are plotted with no software gates (black dashes), gates on only incoming ^{19}N (solid

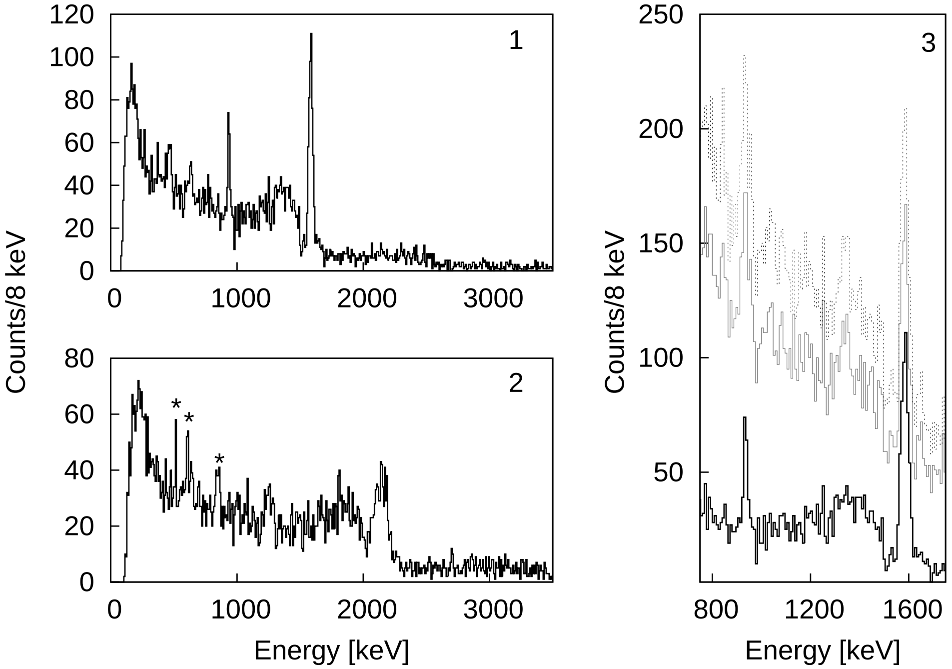

Figure 3.3: Gamma-ray energy spectra for the forward ring of SeGA from target-only production data. Panels 1 and 2 demonstrate the improvement in energy resolution offered by Doppler reconstruction; Panel 3 illustrates the improvement of S:N via software particle gating. See text for details.

gray), and gates on both incoming ^{19}N and outgoing ^{18}C (solid black). The improvement in the full-width at half-maximum energy resolution, E_{res}, achieved by Doppler reconstruction based upon the mean velocity of the ^{18}C reaction residue and the angle of detection with respect to the beam axis is illustrated in the incoming and outgoing particle-gated spectra of Panels 1 (corrected, $E_{res} \approx 2\%$) and 2 (uncorrected, $E_{res} \approx 5\%$). The asterisks in Panel 2 mark three background contaminants corresponding to the 511 keV annihilation line and neutron inelastic scattering in the detector at 609 keV and 844 keV.

Two transitions in ^{18}C were observed in the Doppler corrected gamma-ray spectra at energies of 932(11) and 1585(19) keV as indicated in Panel 1 of Fig. 3.3. The energies are in good agreement with the values of 919(10) and 1585(10) keV reported in Ref. [96]. These two photopeaks are shown in greater detail in the target-only spectra of Fig. 3.4. The full

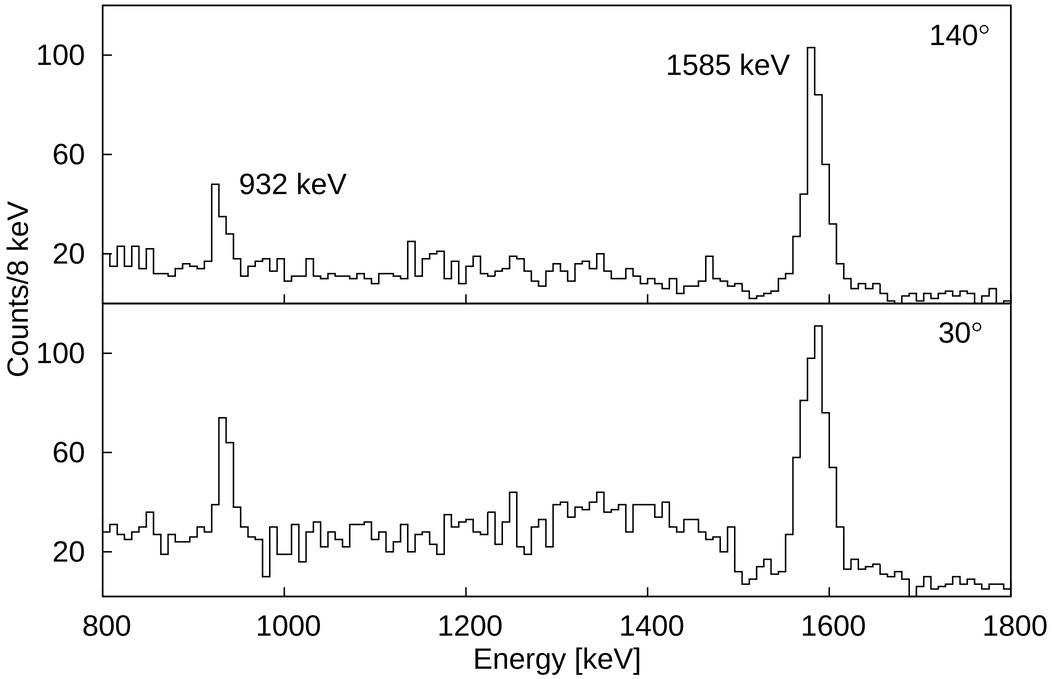

Figure 3.4: Doppler reconstructed gamma-ray energy spectra for the forward (bottom) and backward (top) rings of SeGA. The data were collected with the plunger degrader removed and therefore each transition is represented by a single photopeak. Note the misalignment of the 932 keV transition; the Doppler reconstruction was performed to align the 1585 keV transition corresponding to decays downstream of the target.

width at half maximum energy resolution for the forward and backward rings is 2.27(9)% and 1.89(7)% respectively, in excellent agreement with the estimated resolution of 2.21% and 1.96% as discussed in Appendix B.

After in-beam efficiency corrections at the Doppler shifted laboratory energies, 80% of the observed photopeak intensity was in the 1585 keV photopeak which corresponds to the $2_1^+ \rightarrow 0_{gs}^+$ transition of interest. The remaining photopeak intensity was in the 932 keV transition populating the 2_1^+ state from a higher-lying state with undetermined J^π. Their placement in the ^{18}C level scheme is illustrated in Fig. 3.5. The in-beam photopeak efficiency was extracted from source efficiency measurements by correcting for the asymmetric gamma-ray intensity distribution introduced by the Lorentz boost. Thus, assuming no additional

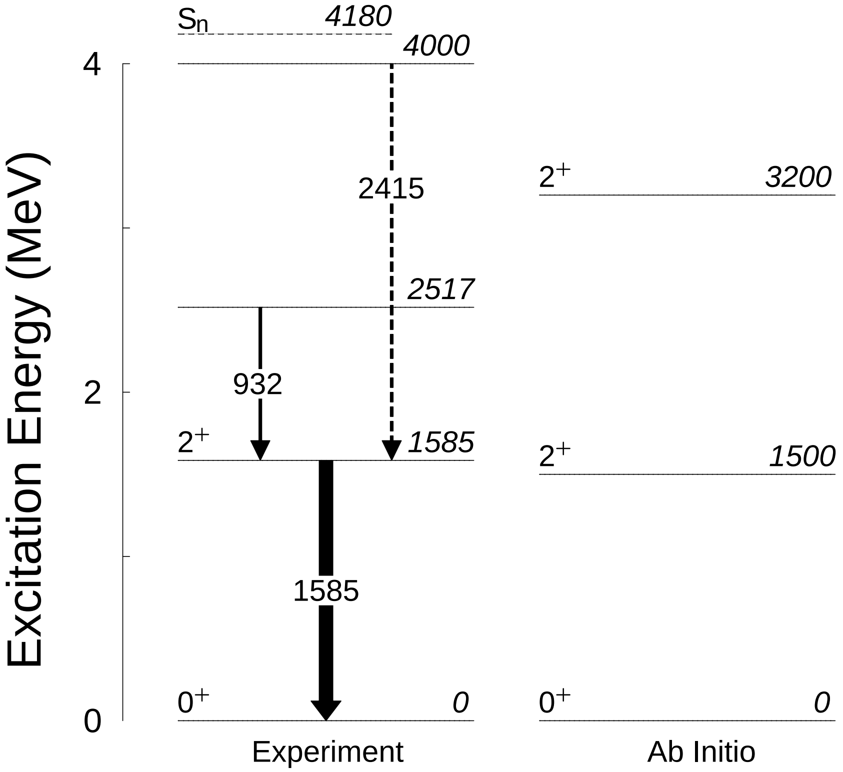

Figure 3.5: Experimental level scheme of ^{18}C (left). The solid arrows indicate transitions observed in this work; their relative thickness corresponds to the measured in-beam efficiency-corrected intensity. The 4 MeV level and an unobserved gamma-ray (dashed arrow) were reported in Ref. [96]. The neutron separation energy was taken from Ref. [97]. The energy levels from *ab initio* calculations [15] discussed in Ch. 5 are given on the right.

feeding contributions to either observed state, the proton knockout reaction was found to preferentially populate the 2_1^+ state over the higher-lying feeder state by a ratio of 4 : 1.

For the lifetime analysis of $2_1^+ \rightarrow 0_{gs}^+$ transition in ^{18}C, the effect of the 932 keV feeder transition was determined to be negligible. This simplification is justified by the 4 : 1 ratio of proton knockout reactions which directly populated the 2_1^+ state. Furthermore, aligning the 932 keV photopeaks in the two rings of SeGA in the Doppler reconstructed target-only gamma-ray energy spectra required $\beta = 0.3650(5)$. Thus the 932 keV transition must proceed within the target and therefore has a very short lifetime of only a few picoseconds. This is clear when compared to the $\beta = 0.3610(5)$ necessary to align the 1585 keV photopeaks, as these transitions proceed in vacuum downstream of the target. From these two pieces of information, it was decided to neglect feeding effects in the lifetime analysis. The error introduced from this simplification is negligible compared to the uncertainty of t_0 (the time from which "counting" begins for the lifetime), corresponding to where in the thick 1 mm plunger target the 2_1^+ state in ^{18}C was produced. Nonetheless, despite low statistics for the 932 keV transition and thick plunger foils optimized for larger lifetime measurements, an upper limit for the lifetime of the feeder transition was extracted.

3.3 Lifetime Analysis

The ^{18}C particle-gated gamma-ray spectra collected at all five target-degrader distances yielded gamma-ray lineshapes with components from fast, slowing, and fully-slowed decays that occurred before, inside, and after the plunger degrader. Fitting these experimental spectra with simulated lineshapes generated from various input lifetime values yielded the measured lifetime result. Details of the simulations and lifetime analysis for the observed transitions in ^{18}C are presented here.

3.3.1 Specifics of Geant4/ROOT Simulations

Monte-Carlo simulations based upon the Geant4/ROOT toolkits were used to determine the lifetime of the observed transitions in ^{18}C. These simulations required the parameterization of experimental details to produce accurate simulated gamma-ray lineshapes. Section 3.1 described the assorted experimental data collected to properly constrain the parameters. The full simulation—describing the experimental geometry and detector response, beam properties, reaction kinematics, and gamma-ray decay and interaction processes—was methodically constructed in small increments; each added complexity was vetted against experimental data to ensure accuracy and consistency. The more salient steps in this process are presented here.

SeGA Geometry

The canonical Plunger SeGA ring angles of 30° and 140° are often just approximations of the true angles. The exact values must be known to obtain proper Doppler reconstructed gamma-ray spectra. Variations in the installation of the two SeGA rings and/or inaccurate placement of the plunger[1] result in forward and backward ring angles that deviate from their canonical values. A laser tracking system can be employed to determine the exact angles of the SeGA rings. In practice however, this is a difficult and time consuming set of measurements to make in the confines of the experimental vault.

In the present analysis, the eight SeGA slice spectra in each ring from target-only production data were compared to their simulated counterparts. As the slice spectra are not Doppler corrected, the photopeak centroid varies from one slice to the next according to that slice's angle with respect to the beam axis. This varying photopeak position is used to determine the correct SeGA ring angles; by varying the input angles in the simulated slice spectra, the best fit yields the exact angles of the forward and backward rings. From this procedure, the forward ring was found to deviate by nearly 2° from the canonical value and was determined to be at $31.9(2)^\circ$. The backward ring, at $140.3(2)^\circ$, was much closer to the canonical value of 140°. These angles were thus used to calculate the true segment angles used for the Doppler reconstruction of both the experimental and simulated gamma-ray lineshapes.

Photopeak Efficiency

With the geometry fixed, the simulated photopeak efficiency for ^{152}Eu and ^{226}Ra gamma-ray sources was compared to the measured source photopeak efficiency (discussed within Subsect. 2.3.4). Figure 3.6 demonstrates the agreement between the scaled simulated (red)

---

[1] Recall that the upstream face of the degrader should correspond to the target position of the S800. It is from this position that the laboratory angles are determined and therefore if the plunger is shifted along the beam axis, the angles will differ from their canonical values.

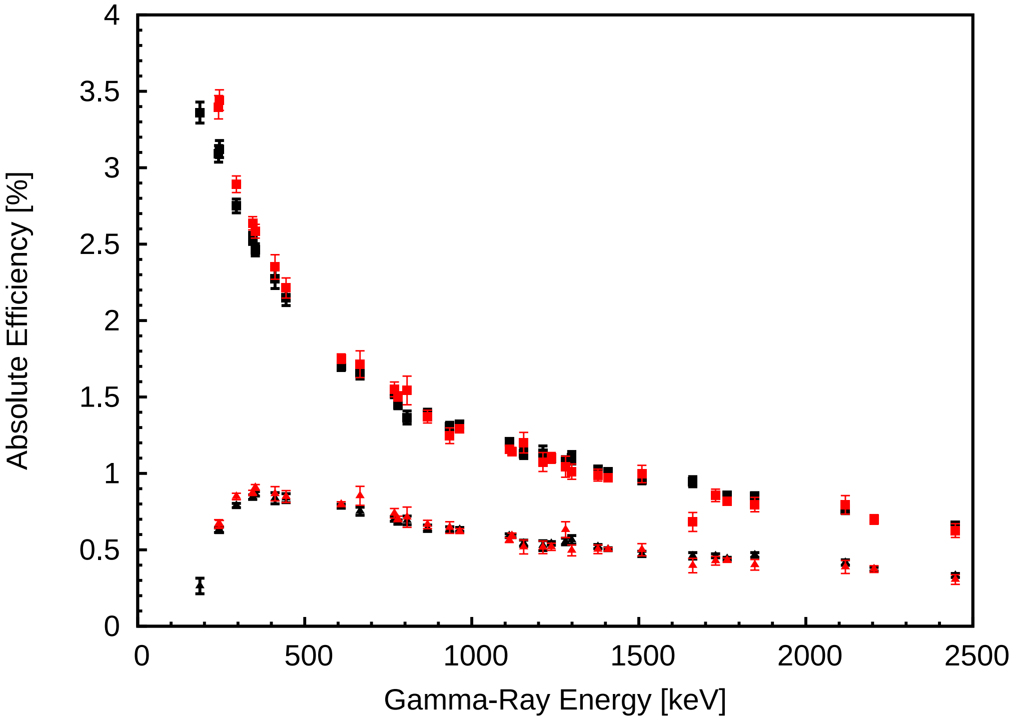

Figure 3.6: Absolute SeGA photopeak efficiency curves from measured ^{152}Eu and ^{226}Ra source data (black) and scaled simulations (red) for the 30° ring (triangles) and 140° ring (squares). See text for details.

and experimental (black) photopeak efficiency curves. The scaling factors of both SeGA rings coincided within uncertainties and were roughly 0.8 and 0.6 for the ^{152}Eu and ^{226}Ra sources, respectively. This scaling is inconsequential as the lifetime analysis incorporates a scaling factor for the simulated lineshapes of each SeGA ring to attain the best match to the data. What is important is the equivalent shapes of the efficiency curves for the forward and backward rings after scaling—especially in the 1 to 2 MeV range which corresponds to the Doppler shifted energies of the 1585 keV transition. The low-energy deviation observed in the backward ring may reflect the absence of plunger target mounting structures in the simulation. The plot suggests these features, which are present in the experiment but not built into the simulation, may account for the additional low-energy photon attenuation in the data with respect to the simulated efficiency curve. Overall, the agreement indicated by Fig. 3.6

validates the simulation's implementation of gamma-ray attenuation in the experimental materials (the plunger target and degrader, beam pipe, and SeGA detector casing), the detector response, and the energy-dependent gamma-ray interactions with matter.

Beam Characteristics and Reaction Kinematics

The ^{19}N secondary beam emittance and straggling through the plunger target was parameterized by fitting the simulated a_{ta}, b_{ta}, y_{ta}, and d_{ta} S800 target spectra to their experimental counterparts for target-only, unreacted beam production data. Angular straggling from the one-proton knockout reaction and reaction residue transport through the plunger target and degrader Coulomb fields was properly constrained by similar S800 target fits using full-plunger reacted beam production data. In addition, the effective thickness of the plunger foils and knockout reaction longitudinal momentum transfer were fine-tuned by simultaneously requiring consistency between the simulated and measured beam velocity downstream of the degrader, β_{slow}, and a proper fit between simulated and experimental d_{ta} spectra. The excellent agreement between the simulated S800 target spectra and their experimental counterparts illustrated in Fig. 3.7 indicates an accurate parameterization of the incoming secondary beam properties, plunger foil thicknesses, and knockout reaction dynamics.

Lineshape Generation

The generation of de-excitation gamma-ray spectra at all five plunger distances was the final task in bringing the simulation to full complexity. Having constrained all the parameters describing the experimental geometry, secondary beam emittance, reaction kinematics, and reaction residue properties, the only additional parameters needed to obtain the lineshape spectra were the level and transition energies, the decay lifetimes, and the ^{18}C production yield ratio (N_{tar}/N_{deg}) of the number of one-proton knockout reactions on the target and degrader. The first two pieces of information were well constrained by the experimental

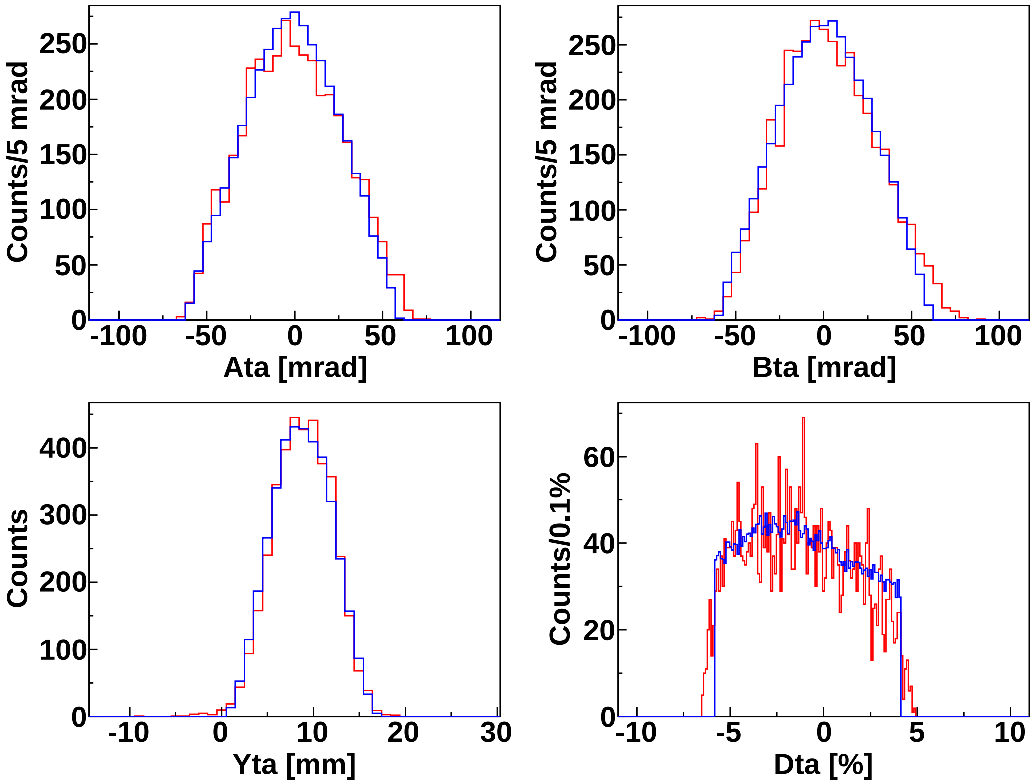

Figure 3.7: Fit of simulated (blue) and experimental (red) ^{18}C reaction residue S800 target spectra. The angular distributions in the dispersive (a_{ta}) and non-dispersive (b_{ta}) directions, spread in non-dispersive position (y_{ta}), and kinetic energy deviation from that corresponding to a central trajectory through the S800 (d_{ta}) are obtained from inverse map trajectory reconstruction. See discussion within Subsect. 2.3.3 for more details.

Doppler reconstructed gamma-ray spectra of Fig. 3.4. The excited state lifetimes were the object of study and therefore were varied in the simulations to ascertain the best fit to the experimental gamma-ray lineshapes. The target-degrader yield ratio is an important parameter and will be described below. The simulation could also incorporate gamma-ray background from target and degrader excitations, however ^{9}Be has no bound excited states and no de-excitations from the $^{\mathrm{nat}}$Ta degrader were observed in the experiment.

The simulated ^{18}C Doppler reconstructed gamma-ray spectra included both of the observed transitions—the 932 keV transition feeding the 2_1^+ state and the 1585 keV transition depopulating this state to the ^{18}C ground state. The photons produced the spectral features (photopeak and associated Compton background) of the β_{fast} and β_{slow} decay components with an intensity ratio dependent upon the input lifetimes, the target-degrader spacing and yield ratio, and the reaction residue velocity. Decays in the degrader at an intermediate velocity were included as well. This required the simulation of properly Doppler shifted photons with a Lorentz boosted intensity distribution (from an assumed isotropic distribution in the rest frame), implementing the in-beam photopeak efficiency, and then correcting for the Doppler shift exactly as done in the experiment—with an input beam velocity β and the calculated SeGA segment angles.

Two simplifications were made for the lifetime fits of the simulated gamma-ray spectra to the experimental lineshapes. First, as discussed in Subsect. 3.2.3, the effect of feeding the 2_1^+ state from above with the 932 keV gamma ray was determined to be negligible. Therefore the final lifetime simulations for the $2_1^+ \rightarrow 0_{gs}^+$ transition did not incorporate the feeder state. Furthermore, in accord with previous Köln/NSCL plunger lifetime measurements utilizing gamma-ray lineshape simulations (see Ref. [22, 78, 94]), only the most sensitive spectral features to lifetime effects—namely the two photopeaks and their relative centroid amplitudes—were included in the lifetime χ^2 analysis. Thus from the simulated gamma-ray spectra, only a region localized around the transition of interest was utilized for the lifetime determination. This simplification facilitated the use of a simple polynomial background function to be added atop the simulated gamma-ray lineshapes.

3.3.2 Electromagnetic Transition Rates in ^{18}C

With simulated plunger gamma-ray lineshapes at each of the five target-degrader distances, the lifetimes of the observed electromagnetic transitions in ^{18}C were extracted. To do this, the χ^2 of the fit between the simulated and experimental spectra at various input lifetimes was calculated within ROOT. The excited state lifetimes were extracted from the minimum in χ^2 as a function of simulated lifetime.

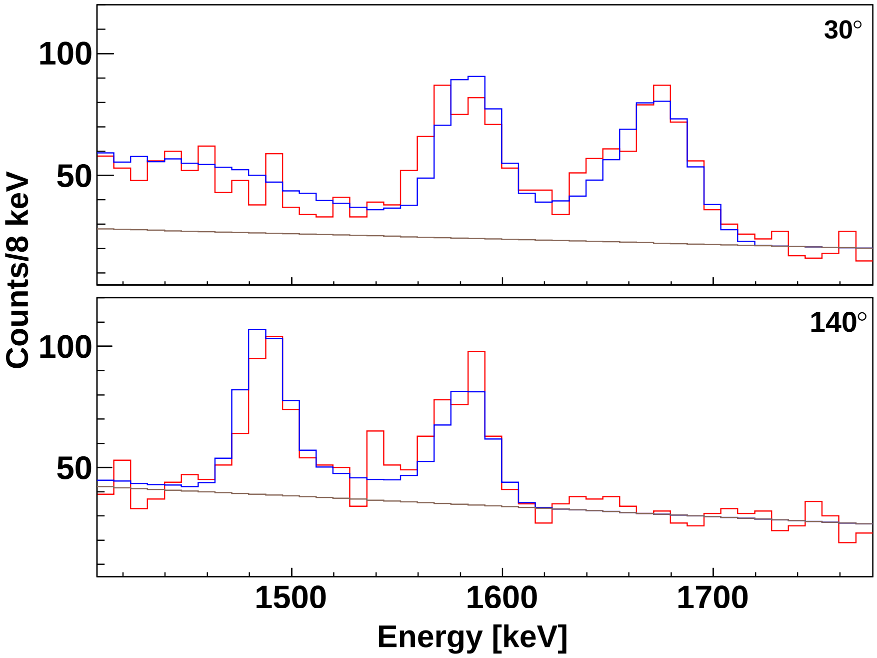

Figure 3.8: Example fit of experimental gamma-ray spectra (red) and best-fit linear background (gray) and gamma-ray lineshapes (blue) for the 1585 keV transition in ^{18}C for the forward (top) and backward (bottom) rings of SeGA at a target-degrader distance of 1.5 mm.

$2_1^+ \rightarrow 0_{gs}^+$ Lifetime

To determine the electric quadrupole transition rate of the 2_1^+ state in ^{18}C, simulated gamma-ray spectra were produced over a coarse lifetime grid. A distribution of χ^2 values was obtained from the fit of these simulated lineshapes to the forward and backward ring experimental data at each distance. To properly account for the unique gamma-ray background present in each ring and at each target-degrader distance, the coefficients of a linear background were allowed to vary freely in the fit. The optimal set of background parameters were taken from the simulation nearest the extracted χ^2 minimum of this broad lifetime scan. Figure 3.8 demonstrates the fit to data (red) acheived by the simulation (blue) with the optimal linear background parameters (gray) and best-fit lifetime (see below) for both the forward and backward rings. With the background parameters fixed, a final lifetime scan was performed in 1 ps increments around the broad lifetime scan minimum. A variable normalization fac-

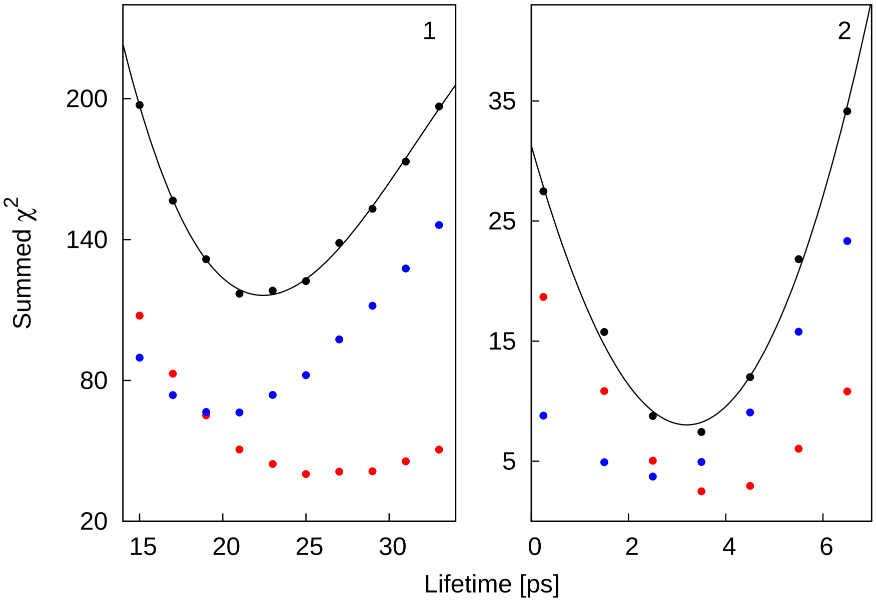

Figure 3.9: χ^2 minimization for the lifetime of the $2_1^+ \rightarrow 0_{gs}^+$ (Panel 1) and 2_1^+ feeder (Panel 2) transitions. The summed χ^2 (black points) was obtained from the unweighted sums of the individual χ^2 values from the fits to the forward (blue points) and backward (red points) ring spectra at each target-degrader distance. The cubic polynomial fits (black lines) were used to determine the χ^2 minimum from which the lifetime was extracted. Despite the lack of lifetime sensitivity exhibited by the backward ring in Panel 1, a complete and independent error analysis for each ring yields consistent lifetime results.

tor accounted for the different statistics obtained in each ring and at each target-degrader distance. A lifetime of $\tau = 22.4 \pm 0.9(\text{stat})$ ps was extracted from the χ^2 minimization of the summed individual χ^2 values from the fits to the forward and backward ring spectra at all five target-degrader distances. Panel 1 of Fig. 3.9 indicates the quality of the summed χ^2 minimization; the minimum was obtained from the cubic polynomial fit to the summed χ^2 data. The statistical error was taken to be the average half-width of this cubic polynomial at a value of $\chi^2 = \chi^2_{min} + 1$ as prescribed in Ref. [98].

Figure 3.10 illustrates the best fit of simulated lineshapes to the experimental gamma-ray spectra for all five plunger distances. The fits were generated with the background parameters fixed to their optimal values as described in the previous paragraph and the lifetime extracted

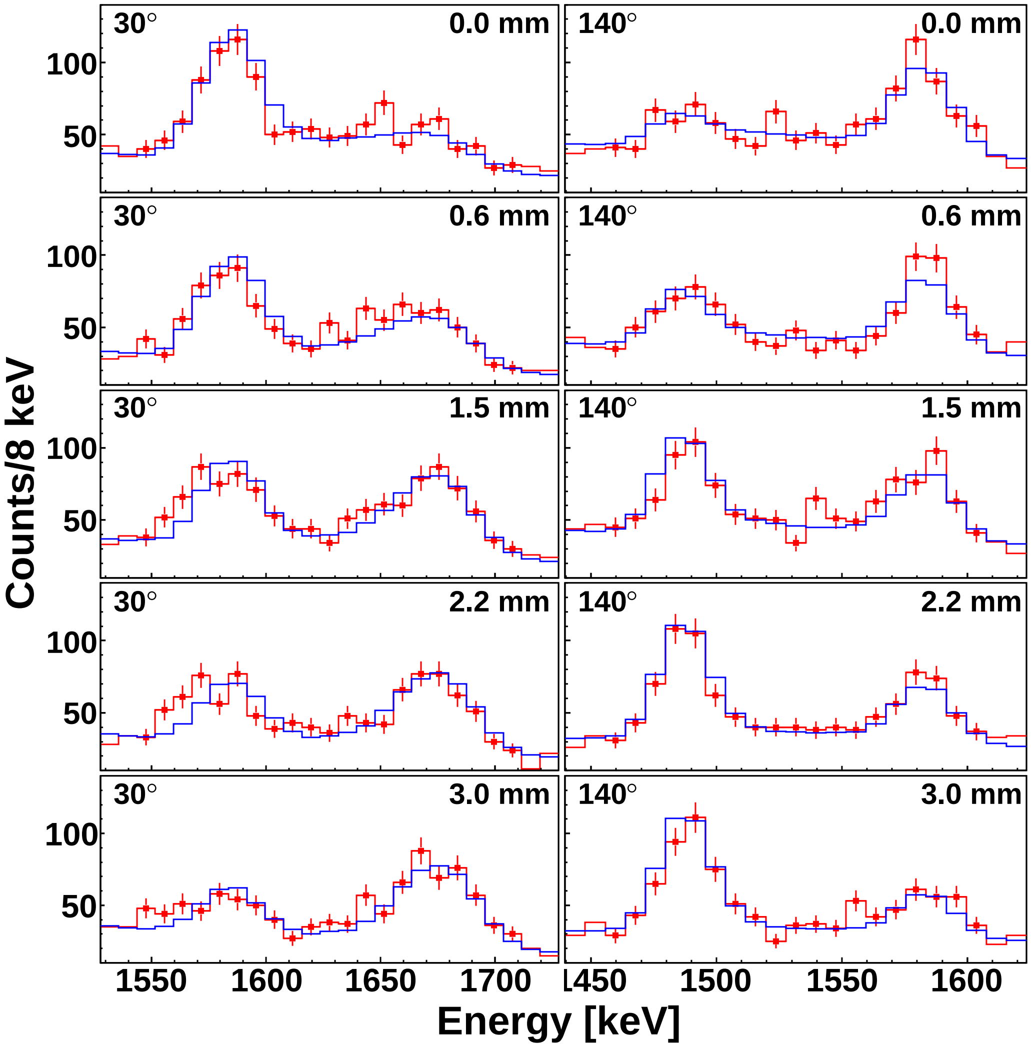

Figure 3.10: Experimental gamma-ray spectra with statistical uncertainties (red) and simulated lineshapes (blue) for the 1585 keV $2_1^+ \rightarrow 0_{gs}^+$ transition in ^{18}C for the forward (left column) and backward (right column) rings of SeGA and all five plunger target-degrader distances. The simulated lineshapes were generated with $\tau = 22.4$ ps. Bins with experimental error bars indicate the lifetime-sensitive region of the lineshapes where the χ^2 was calculated.

from the summed χ^2 minimum (Panel 1 of Fig. 3.9). The figure indicates the narrow lifetime-sensitive region over which the fit was performed.

The most dominant source of systematic error in the reported measurement was an uncertainty in the ^{18}C production yield ratio of one-proton knockout reactions on the target and degrader (N_{tar}/N_{deg}). For target-degrader distances several times that of the average flight distance of the 2^+ excited state ($d = \gamma v \tau \approx 2$ mm), the expectation is that all decays occur upstream of the degrader. Hence the observation of a slow component in the Doppler reconstructed gamma-ray spectrum at these so-called "infinite distances" would elucidate the ^{18}C production yield via one-proton knockout reactions on the degrader. Production data at this large distance were not obtained due to experimental time constraints. This led to a large uncertainty in the target-degrader yield ratio.

To deduce the ratio, a two dimensional χ^2 hypersurface was generated from the fit of experimental spectra in the forward ring to the corresponding simulated lineshapes obtained with various input lifetimes and target-degrader yield ratios. A bivariate quadratic function f was fit to this χ^2 surface and both the minimum f_{min} and the ellipse tracing the function at a value of $f_{min} + 1$ were obtained. Figure 3.11 provides more details. Projecting the minimum and this ellipse onto the ^{18}C production yield ratio axis generated the range of permissible ratios 2.15 ± 0.74. An additional constraint restricted the lower limit: assuming the production data obtained at the 3 mm distance corresponded to the infinite distance, a ratio of 2.09 ± 0.28 was obtained. Thus the actual ratio must be larger than 1.81 since this distance is insufficient to completely remove the target contribution to the slow component of the Doppler reconstructed gamma-ray spectrum. Therefore the final ^{18}C production yield ratio was determined to be $2.15^{+0.74}_{-0.34}$.

To ascertain the uncertainty of the lifetime measurement introduced by the poorly constrained ^{18}C production yield ratio, lifetime scans were performed with the ratio set to the extracted upper and lower limits. From the minima of the resulting summed χ^2 of the fits, the systematic error introduced by the uncertainty in this ratio was found to be $\tau^{+2.2}_{-1.1}$ ps. Deviations between the experimental and simulated momentum distribution were also found to be an important source systematic error. Uncertainties in the simulated ^{18}C momentum distribution impact the Doppler shift and thereby alter the simulated Doppler reconstructed gamma-ray spectra. It was determined that a scant 2% change in the degrader thickness

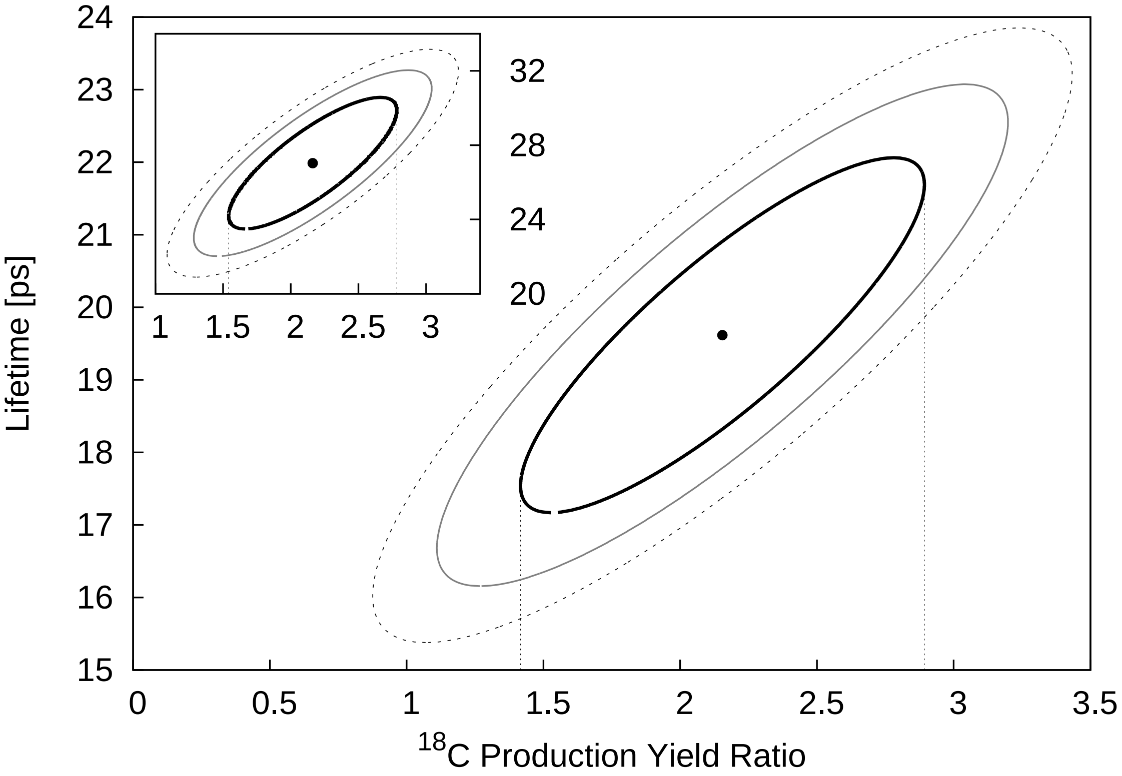

Figure 3.11: Ellipses tracing the $f_{min} + 1$ (black solid), $f_{min} + 2$ (gray solid), and $f_{min} + 3$ (black dashed) cross sections of the bivariate quadratic function fit to the two dimensional χ^2 hypersurface described in text. From the global minimum (square) and dashed vertical traces, the ^{18}C production yield ratio was determined to be 2.15 ± 0.74 from the forward ring (main plot) and 2.16 ± 0.62 from the backward ring (inset). The ^{18}C production yield ratio was taken from the forward ring fit data as it yielded a slightly wider range of permissible values and therefore a more conservative estimate of the uncertainty in the ratio.

was tolerable before disrupting the fit of the experimental and simulated dta spectra. Thus another pair of lifetime scans were performed at these extrema. The resulting χ^2 minima indicated a systematic uncertainty of $\tau \pm 1.1$ ps. Other sources of error were found to be negligible and thus the root sum of squares was adopted for the final systematic error.

Including both statistical and systematic errors, the lifetime of the $2^+_1 \rightarrow 0^+_{gs}$ transition in ^{18}C was found to be $\tau = 22.4 \pm 0.9(\text{stat})^{+2.5}_{-1.6}(\text{syst})$ ps. This is in agreement with [29], which reported a lifetime of $18.9 \pm 0.9(\text{stat}) \pm 4.4(\text{syst})$ ps.

2_1^+ Feeder Lifetime

The plunger target and degrader thicknesses ($\sim$ 1 mm) were optimized for the lifetime measurement of the $2_1^+ \rightarrow 0_1^+$ transition in ^{18}C. Thus the setup was not ideal for measuring lifetimes of only a few picoseconds as most de-excitations would occur in the plunger foils rather than in vacuum. Indeed, the beam velocity required to align the 932 keV transition in the Doppler reconstructed spectra of each SeGA ring was larger than that used to align the 1585 keV transition, which corresponded to decays in vacuum downstream of the target. In addition, the one-proton knockout from ^{19}N preferentially populated the 2_1^+ excited state by a ratio of 4 : 1. Nonetheless, a lifetime upper limit was established for the 932 keV transition which populated the 2_1^+ state.

The combination of thick plunger foils and a fast de-excitation resulted in the majority of gamma-ray decays proceeding within the same foil as the knockout reaction. Very few decays occurred in vacuum and therefore the Doppler reconstructed lineshapes were qualitatively the same regardless of target-degrader distance. Thus the experimental gamma-ray spectra from all five distances were summed and the resulting effective 0 mm distance spectrum was fit with simulated lineshapes also generated at a 0 mm target-degrader distance. Note that the summing does not improve the signal-to-noise ratio of the data, but rather has the effect of smoothing out statistical fluctuations in the background. This improved the accuracy of the background polynomial fit functions.

The lineshape simulations of the 932 keV transition were generated in much the same manner as those for the 1585 keV transition. Simulated spectra were produced over a course lifetime grid and the parameters of a cubic polynomial background fit were allowed to freely vary. The optimal background parameters were obtained from the simulation nearest the extracted χ^2 minimum of this broad lifetime scan. A final lifetime scan was then performed and as before, a variable normalization factor accounted for the different statistics obtained in each SeGA ring. The input target-degrader yield ratio of 2.15 from the analysis of the

1585 keV transition was used. The lifetime was determined to be $\tau = 3.2 \pm 0.7(\text{stat})$ ps from the minimum of the summed χ^2 obtained from the individual χ^2 of the fits to the forward and backward ring experimental spectra. This minimum was obtained from the cubic polynomial fit to the χ^2 data (Panel 2 of Fig. 3.9) and the statistical error was taken from the half-width of the polynomial at a value of $\chi^2 = \chi^2_{min} + 1$.

Figure 3.12 illustrates the resulting best fit of simulated lineshapes generated with this lifetime to the summed experimental gamma-ray spectra. The asymmetric peaks primarily arise from excited-state production on the tantalum degrader and the subsequent decay before emerging into vacuum. The black arrows indicate the location of these diminutive degrader components after Doppler reconstruction with the improper velocity corresponding to the more prevalent decays within the target. As before, bins with error bars indicate the narrow region over which the χ^2 fit was performed.

It should be noted that the 0 mm experimental 932 keV gamma-ray lineshape in the forward ring could be fit with two Gaussian components. These corresponded to excited-state production and subsequent decay entirely within the target or the degrader. Even with the low statistics, a production yield ratio of 3.5 ± 1.9 was obtained for this 2^+_1 feeder state. This is consistent with the value of 2.15 used to help generate Fig. 3.12, but given the large uncertainty and also the general lack of experimental sensitivity to such short lifetimes, the conservative approach of only pursuing a lifetime upper limit was adopted. This limit was extracted from the χ^2 minimum of the lifetime scans using the upper limit on the excited-state production yield ratio of 5.4. Degrader contributions were thus minimized within the simulation, which then required longer lifetimes to fit the experimental spectra. In this manner, the conservative lifetime upper limit of the 932 keV transition in ^{18}C was found to be $\tau < 4.5$ ps.

The reported results from the $2^+_1 \rightarrow 0^+_{gs}$ lifetime measurement and that of the 932 keV feeder transition are discussed in Ch. 5. There, the nuclear structure implications of the

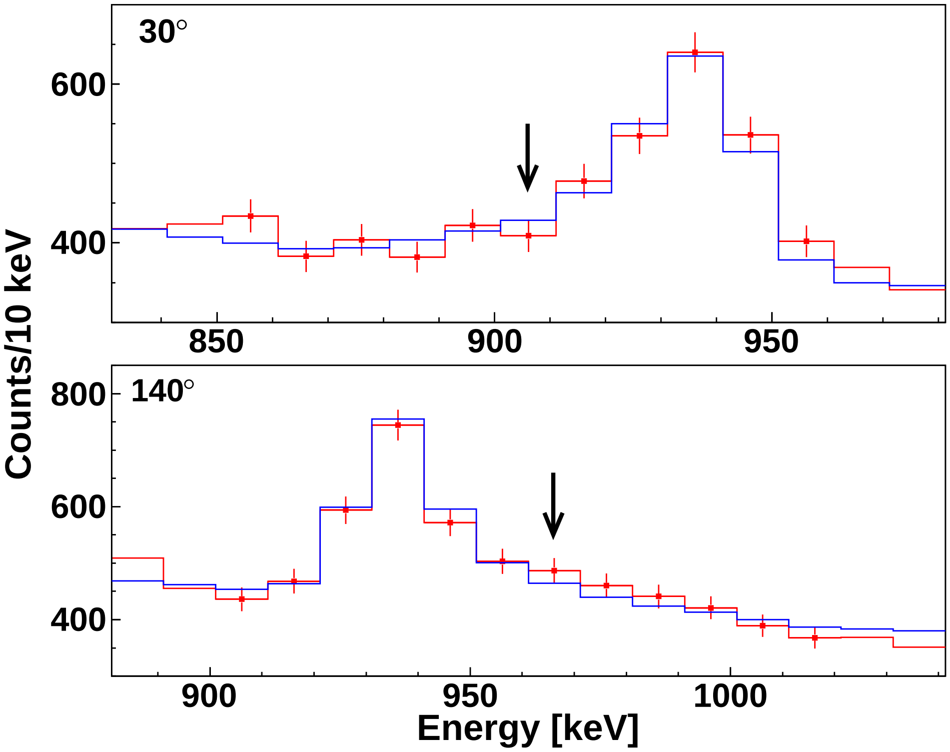

Figure 3.12: Doppler reconstructed experimental gamma-ray spectra with statistical uncertainties (red) and simulated lineshapes (blue) for the 932 keV transition feeding the 2^+_1 state in ^{18}C for the forward (top) and backward (bottom) rings of SeGA. The simulated lineshapes were generated with $\tau = 3.2$ ps. The black arrows indicate the centroid positions of gamma-rays from knockout reactions and decays within the degrader. See text for details.

lifetime measurements are examined both within the context of other recent measurements and in comparison to the results obtained by state-of-the-art *ab initio* no-core shell model (NCSM) theoretical calculations. This comparison provides a vital benchmark for the theoretical tools used, specifically the truncation of unimportant basis states in the NCSM calculation for this $A = 18$ system.

Chapter 4

Two-Proton Decay Lifetime of ^{19}Mg

The mean lifetime measurement of the exotic two-proton decay $^{19}\mathrm{Mg} \rightarrow \mathrm{p} + \mathrm{p} + {}^{17}\mathrm{Ne}$ following the one-neutron knockout reaction $^{\mathrm{nat}}\mathrm{C}(^{20}\mathrm{Mg},\, ^{19}\mathrm{Mg})\mathrm{X}$ in inverse kinematics was conducted at the National Superconducting Cyclotron Laboratory. For the measurement, the Köln/NSCL plunger was modified by replacing the velocity degrader with a silicon double-sided strip detector (DSSD). This enabled elemental identification of both reaction and decay residues[1] emerging from the carbon plunger target. In principle, the lifetime is determined from the varying relative intensity of the ^{19}Mg and ^{17}Ne energy loss peaks in the silicon DSSD as a function of target-DSSD distance. The unambiguous identification of ^{19}Mg from the unreacted ^{20}Mg secondary beam was facilitated by a software particle gate on the two-proton decay residue ^{17}Ne detected in the S800 focal plane.

This study was the first of its kind and therefore serves as a proof of concept for the particle plunger variant of the Recoil Distance Method for picosecond lifetime measurements along the proton dripline. The low counting statistics in the ^{19}Mg energy loss peak at the

---

[1] The signature reaction and decay residues in this study were ^{19}Mg and ^{17}Ne, respectively; the lifetime analysis was not sensitive to the proton decay remnants. However, to avoid confusion of terms, "reaction residues" in this chapter shall henceforth refer to both ^{19}Mg and ^{17}Ne. A distinction will be made where additional clarity is necessary.

0 mm target-DSSD distance indicated a lifetime much shorter than the literature value of $\tau = 5.8 \pm 2.2$ ps [38]. It also reduced the analysis to lineshape fitting at a single distance in a manner similar to the lifetime analysis of the feeder transition in ^{18}C as presented in Ch. 3. To properly fit the full energy loss lineshape, the contribution of the nonresonant breakup $^{20}\mathrm{Mg} \rightarrow \mathrm{p} + \mathrm{p} + \mathrm{n} + {}^{17}\mathrm{Ne}$ to the prominent ^{17}Ne energy loss peak must be quantified. However, the production mechanism ratio, given by

$$R_p = \frac{{}^{\mathrm{nat}}\mathrm{C}({}^{20}\mathrm{Mg},\ {}^{17}\mathrm{Ne})\mathrm{X}}{{}^{\mathrm{nat}}\mathrm{C}({}^{20}\mathrm{Mg},\ {}^{19}\mathrm{Mg})\mathrm{X} + {}^{\mathrm{nat}}\mathrm{C}({}^{20}\mathrm{Mg},\ {}^{17}\mathrm{Ne})\mathrm{X}}, \tag{4.1}$$

could not be constrained by the data, as the resulting ^{17}Ne DSSD energy loss signal is indistinguishable regardless of origin.

Hence, the mean lifetime of the two-proton emitter ^{19}Mg was determined as a function of the production mechanism ratio in the range $R_p = [0.05, 0.95]$. As R_p was increased, the best fits were achieved with a monotonically increasing lifetime. In particular, within the reasonable range $R_p = [0.15, 0.85]$, the best-fit lifetimes fell in the range $\tau = [0.39, 2.44]$ ps. Technical details and calibration procedures for the Köln/NSCL particle plunger and supporting experimental devices were discussed in depth in Ch. 2. The details regarding the measurement, data analysis, and experimental results are presented here.

4.1 Experimental Considerations

Similar to the procedure reported in Ch. 3, several types of in-beam data were collected during the experiment to facilitate the proper characterization of the detector systems. These data also helped constrain the many simulation parameters necessary to generate energy loss DSSD lineshapes for the lifetime analysis. The experiment was not designed to be analyzed via lineshape simulations; therefore without certain data some simulation parameters could not be optimally constrained. For instance, without target-only production data, the effective target and detector thicknesses were fixed to the manufacturers' specifications. However, as indicated by the Bethe formula of Eq. 2.4, the energy deposited in the DSSD is inversely proportional to the beam energy. Hence a good agreement between the simulated and measured reaction residue momentum distribution is vital for accurate energy loss simulations. A description of the steps necessary to ensure this follows.

- The unreacted ^{20}Mg secondary beam was delivered through the full particle plunger and swept across the focal plane to calibrate the S800 CRDCs. In total, 3 CRDC mask calibrations were taken during the experiment. Gains and offsets were extracted to correlate the raw detector signals with the well defined (x, y) coordinates of the mask slits and holes. From the three sets of calibration parameters, a run-by-run set of parameters was extracted as described within Subsect. 2.3.3. The resulting calibrated CRDC positions and angles (x_{fp}, y_{fp}, a_{fp}, and b_{fp}) were used for the trajectory reconstruction of the reaction residues back to the S800 target position.

- In addition, the unreacted beam data was used to calibrate the 16 channels of the S800 ionization chamber (IC). The raw energy loss signals in each channel were gain matched to a representative channel such that from the calibrated signals, an average energy deposit could be calculated on an event-by-event basis.

- The data used for the IC calibration were also used to help constrain the simulation parameters describing the secondary beam emittance and straggling through the target and detector. This was done by constructing simulated S800 target parameter spectra (a_{ta}, b_{ta}, y_{ta}, and d_{ta}) and fitting them to their experimental counterparts obtained from unreacted beam trajectory reconstruction.

- Finally, the S800 magnetic rigidity was tuned to center the two-proton decay remnant ^{17}Ne in the focal plane. From the calibrated focal plane positions and magnetic field settings, the experimental S800 target spectra were used to constrain the one-neutron knockout reaction kinematics. Simulated S800 target spectra were fit to their experimental counterparts and the extracted reaction parameters were used for both reactions on the target and silicon detector, as well as both ^{17}Ne production mechanisms. The lack of target-only reacted beam production data necessitated the former simplification. The latter was necessary from the indistinguishable origin of ^{17}Ne from the breakup of ^{20}Mg or the two-proton decay of ^{19}Mg.

The quality of the fit between the experimental S800 target spectra and fully constructed reaction residue simulation is illustrated in Fig. 4.5 within Subsect. 4.3.1. Despite an asymmetric beam profile in the non-dispersive direction, the excellent agreement between the simulated and experimental momentum distribution spectra (d_{ta}) was paramount to producing accurate simulated energy loss lineshapes.

4.2 Experimental Details

The remaining production data was devoted to collecting DSSD energy loss signals in coincidence with reaction residues in the S800 focal plane. The particle plunger Inchworm Control System was kept off until the target-DSSD distance needed to be changed to reduce electronic noise in the DSSD. The S800 was operated in focused mode and was tuned to accept the decay remnant ^{17}Ne. The data acquisition was triggered by the detection of a particle (reaction residue or beam ion within the S800 momentum acceptance) in the E1 scintillator. Several other reaction residues with similar momentum-to-charge ratios were within the acceptance cut. One of these, ^{18}Ne, proved particularly useful in the analysis as will be discussed in Sect. 4.3.1. A discussion of the properties of the radioactive ^{20}Mg secondary beam, subsequent reaction residues, and observed DSSD energy loss signals follows immediately.

4.2.1 Radioactive Secondary Beam

A ^{24}Mg primary beam was accelerated by the Coupled Cyclotron Facility at NSCL and fragmented on a thick ^{9}Be production target. A ^{20}Mg radioactive secondary beam was selected, purified, and delivered to the Köln/NSCL particle plunger target. The method and devices used were discussed in Sect. 2.2.

The ^{24}Mg^{+12} primary beam was accelerated to 170 MeV/u ($\approx$ 0.53% the speed of light) by the coupled K500 and K1200 cyclotrons and delivered to a 1081 mg/cm^2 ($\approx$ 5.8 mm thick) ^{9}Be production target. The settings of the A1900 were adjusted to provide an adequate balance between purity and intensity of the ^{20}Mg secondary beam. In particular, the momentum acceptance was restricted to 0.5% with momentum apertures installed at Image 1 and 2. A 1050 mg/cm^2 energy degrading Al wedge at Image 2 was used for additional isotopic separation. The desired ^{20}Mg secondary beam emerged from the A1900 with a purity of roughly 36%. Three significant secondary beam contaminants—^{16}O, ^{17}F, and ^{18}Ne—were distinguished from the ^{20}Mg fragment by their time of flight between two thin plastic scintillators installed at the A1900 focal plane and the S800 object position. The time of flight of a ^{10}C contaminant could not be resolved from ^{20}Mg since they have the same mass-to-charge ratio and thus the same time of flight. Instead, software particle gates on their unique energy loss in the S800 ionization chamber provided the separation. The properties of the secondary beam are listed in Tab. 4.1 where the subscripts refer to the four A1900 dipole magnets.

The desired ^{20}Mg radioactive secondary beam emerged from the A1900 with an energy of 92.65 MeV/u alongside the four contaminants and was delivered to the particle plunger at the S800 target position. The unreacted secondary beam time of flight from the A1900 focal plane to the S800 object position is plotted in Fig. 4.1. Note the clean separation between the ^{16}O, ^{17}F, ^{18}Ne, and ^{20}Mg time of flight peaks which facilitated offline separation during the analysis. After setting a software gate on the ^{20}Mg time of flight peak, the ^{10}C component was removed by particle gating in the S800 (see Subsect. 4.2.2).

Table 4.1: ^{20}Mg secondary cocktail beam characteristics. $B\rho$ and $\Delta p/p$ were taken from the experimental beam line savesets provided by the A1900 Fragment Separator Group. The beam energy was calculated from $B\rho_{3,4}$. The beam composition percentages were calculated by integrating the appropriate time of flight peaks in Fig. 4.1. The ^{20}Mg average rate and transmission to the S800 were calculated from run-by-run scaler information.

B$\rho_{1,2}$	2.85500 T · m
B$\rho_{3,4}$	2.36871 T · m
Final Energy	92.65 MeV/u
$\Delta p/p$	0.5%
^{10}C Contaminant	4.9%
^{16}O Contaminant	28.6%
^{17}F Contaminant	10.6%
^{18}Ne Contaminant	18.7%
^{20}Mg Total Purity	36.2%
Average Rate	2500 pps
Transmission to S800	65%

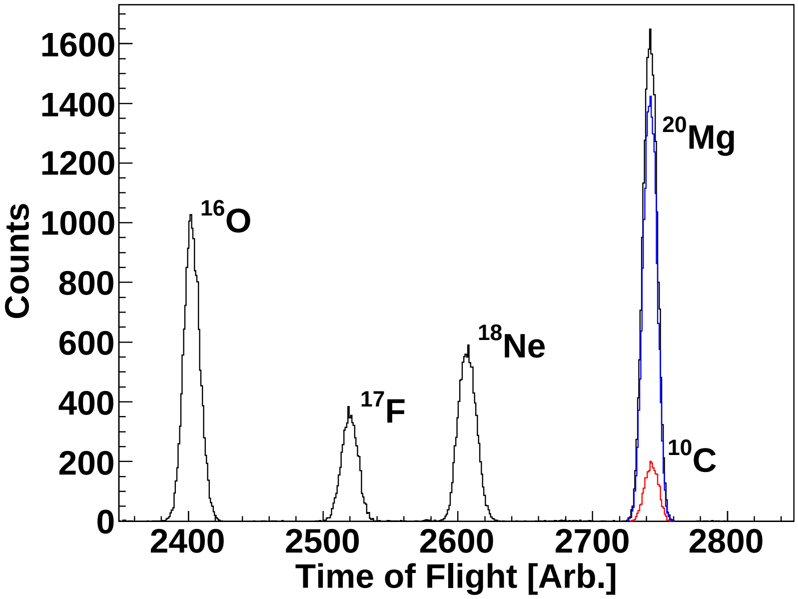

Figure 4.1: Identification of the secondary beam components by their time of flight between two thin plastic scintillators at the A1900 focal plane and object position of the S800. To resolve the ^{10}C (red) and ^{20}Mg (blue) components of the fourth peak, the time of flight data was sorted from appropriately particle-gated events in the S800. Increasing time is from right to left along the abscissa.

The plastic time of flight scintillators were also used to monitor the beam rates. The secondary beam emerged from the A1900 with an average rate of 6800 pps as measured at the A1900 focal plane. Transmission losses en route to the S800 were measured by the ratio of beam rates at the A1900 focal plane and S800 object position to be nearly 35%.

4.2.2 Outgoing Reaction Residues

The S800 Magnetic Spectrometer provided event-by-event particle identification and data acquisition triggering. The ^{20}Mg radioactive secondary beam was focused at the object position and then delivered via the analysis line as a focused beamspot onto the Köln/NSCL particle plunger $^{\mathrm{nat}}$C 110 mg/cm^2 (≈ 0.5 mm thick) target. States in ^{19}Mg were populated by the one neutron knockout reaction and subsequently decayed by two-proton emission[2] after a distance governed by the lifetime and beam velocity to available states in ^{17}Ne. A similar one-neutron knockout reaction of a ^{20}Mg secondary beam on a thick beryllium target was used in the ^{19}Mg lifetime measurement of Ref. [38]. The S800 magnetic rigidity was set to $B\rho = 2.29402\ \mathrm{T \cdot m}$ in order to center the ^{17}Ne reaction residues in the focal plane and reject reaction residues from the secondary beam contaminants.

Various reaction residues, the ^{17}Ne two-proton decay remnants, and the high-momentum tail of unreacted ^{20}Mg fell within the momentum acceptance of the S800. Each component was clearly resolved on an event-by-event basis by their energy loss through the S800 ionization chamber and time of flight between the object position and E1 focal plane scintillators.

---

[2] There is no experimental differentiation between proton emission from the ground state (via direct two-proton decay) and excited states (via sequential one-proton decays through a resonance in the $(Z-1)$ intermediary ^{18}Na). Following Ref. [38], excited state decays will have a lifetime far below the picosecond sensitivity we report here and thus these events are indistinguishable from the nonresonant breakup of ^{20}Mg. Therefore the contribution of these two processes to the energy loss data are lumped together within the ^{17}Ne production mechanism ratio R_p. Hence, the term "two-proton decay" labels only ground state proton emission of ^{19}Mg and variants of "direct production of ^{17}Ne" are taken to mean both the breakup of ^{20}Mg and prompt ^{19}Mg excited state decay.

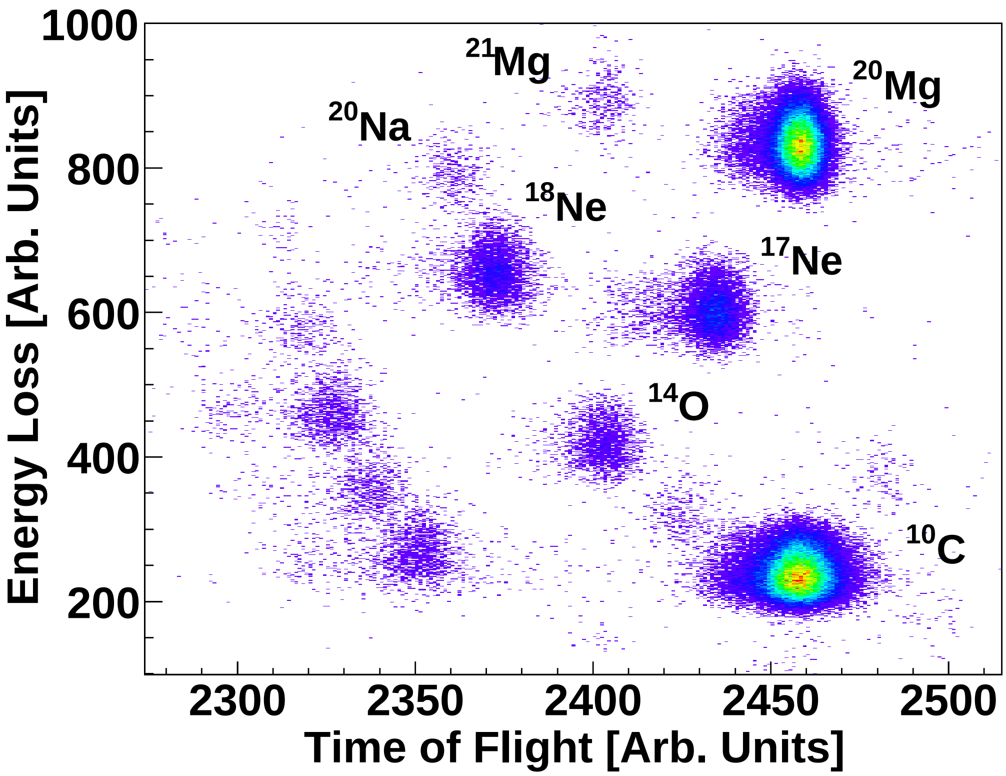

Figure 4.2: Identification of the outgoing reaction residues and decay remnants from the incoming ^{20}Mg secondary beam by time of flight and energy loss information from the S800 Spectrometer. Increasing time is from the right to left along the abscissa.

Figure 4.2 illustrates this particle identification spectrum. The quality of isotopic separation indicated in the figure was achieved with flight-path corrected time of flight and calibrated IC energy loss signals using the focal plane angles and positions determined from the calibrated CRDCs (as discussed within Subsect. 2.3.3). The population of several reaction channels close in mass to ^{20}Mg serves as indirect evidence that the one-neutron knockout reaction producing ^{19}Mg likely occurred.

4.2.3 Observed DSSD Energy Loss Spectra and Analysis

The energy loss profile of each beam particle emerging from the particle plunger target was detected in the 69 mg/cm^2 ($\approx$ 0.3 mm thick) silicon double-sided strip detector mounted downstream of the target. Each face of the DSSD was electronically segmented into 16 strips; the gain-matched front strip spectra were summed to produce run-by-run ΔE lineshapes. More details were provided within Subsect. 2.3.2.

DSSD energy loss signals were recorded in coincidence with reaction residues detected in the S800 E1 scintillator. This trigger requirement suppressed background energy loss signals from contaminant reaction residues. Further background reduction was achieved during analysis by software particle gates on incoming ^{20}Mg and outgoing ^{17}Ne.[3] The incremental enhancement in the signal-to-noise (S:N) ratio is demonstrated in Panel 1 of Fig. 4.3 where ΔE lineshapes are shown for ungated data (black dashes), data gated on incoming ^{20}Mg (solid gray), and data gated on both incoming ^{20}Mg and outgoing ^{17}Ne (solid black). This final set of gates removed all DSSD signals not directly related to either the two-proton decay $^{19}\mathrm{Mg} \rightarrow \mathrm{p} + \mathrm{p} + {}^{17}\mathrm{Ne}$ or the direct dissociation $^{20}\mathrm{Mg} \rightarrow \mathrm{p} + \mathrm{p} + \mathrm{n} + {}^{17}\mathrm{Ne}$.

^{17}Ne particle-gated DSSD energy loss spectra were collected at five target-DSSD distances of 0.0, 100.0, 200.0, 500.0, and 1000.0 µm. The combination of reactions on the target and detector for both direct production of ^{19}Mg and ^{17}Ne and also two-proton decays in the target and detector obfuscated the origin of the ΔE components which together comprise the full lineshape plotted in Panel 2 of Fig. 4.3. Events where only ^{17}Ne traversed the detector—corresponding to the direct production of ^{17}Ne in the target or the production and decay of ^{19}Mg in the target—generated the full energy ^{17}Ne peak. The small ^{19}Mg peak originated from magnesium energy loss through the entire detector—corresponding to ^{19}Mg production in the target (or extreme front/back of the detector) and decay after the detector. The broad plateau between the two peaks was generated by events with mixed neon and magnesium energy deposits. Neither the experimental data or previous studies addressed the relative importance of each of these components; thus the simulations discussed

---

[3] Recall from Subsect. 4.2.1 that a time of flight gate on the incoming ^{20}Mg peak necessarily includes contributions from ^{10}C. The subsequent S800 particle gate on ^{17}Ne precludes any contributions from ^{10}C in the final DSSD energy loss spectra.

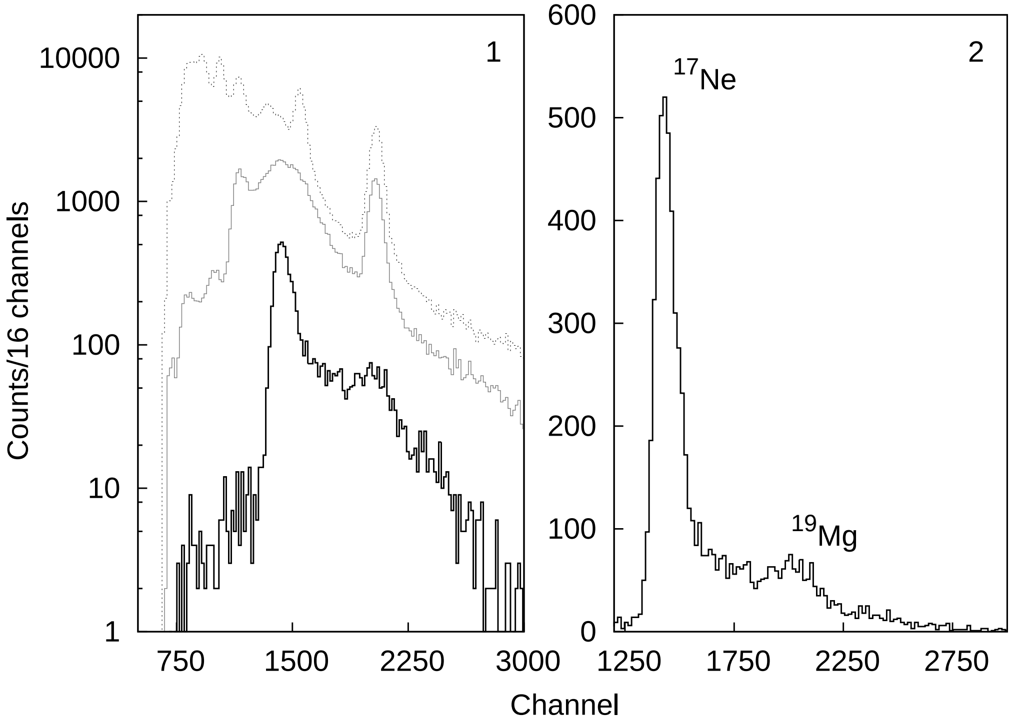

Figure 4.3: Energy loss spectra constructed from summing the front (upstream) gain-matched strips of the DSSD. The data were collected at the 0 mm target-DSSD distance. The improvement in S:N of the DSSD spectra via incoming ^{20}Mg particle gates (solid gray) and incoming ^{20}Mg and outgoing ^{17}Ne particle gates (solid black) in the analysis over the ungated spectrum (black dashes) is demonstrated in Panel 1. Note the logarithmic scale of the ordinate. Panel 2 replots the DSSD ΔE spectrum from the fully-gated data subset linearly.

below were constructed to probe the three dimensional parameter space of lifetime, ^{17}Ne production mechanism ratio R_p, and target-detector yield ratio R_σ. This is the ratio of reactions occurring in the carbon target compared to the silicon detector. The definition is equivalent to the target-degrader yield ratio of Ch. 3, except here the reactions are both the one neutron knockout producing ^{19}Mg and the direct dissociation yielding ^{17}Ne.

4.3 Lifetime Analysis

The ^{17}Ne particle-gated DSSD energy loss spectra for three of the five target-DSSD distances are plotted in Fig. 4.4. The paucity of counts in the ^{19}Mg peak even at 0 mm strongly

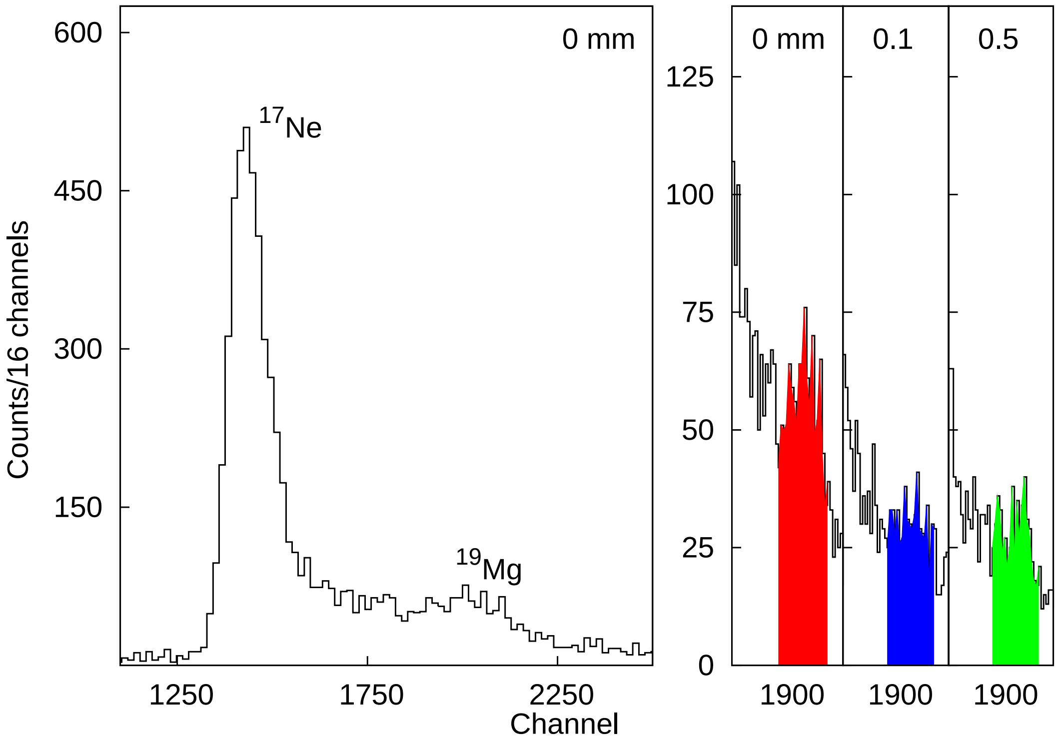

Figure 4.4: ^{17}Ne particle-gated silicon DSSD ΔE spectra. The full spectrum for data taken at the 0 mm target-DSSD distance is plotted in the leftmost column. To the right, the region surrounding the ^{19}Mg energy loss peak is examined for 0 mm (red), 0.1 mm (blue), and 0.5 mm (green) distances.

indicates a very short two-proton decay lifetime. This precluded the lifetime analysis via counting ^{19}Mg as a function of target-detector distance. Instead, a modification of the Monte-Carlo simulation software from the ^{18}C lifetime analysis was used.

It was decided to use only the 0 mm lineshape data for the lifetime analysis due to the slight enhancement of the ^{19}Mg energy loss peak and the near equivalence of the energy loss lineshapes for the remaining distances. This simplification also mitigated the effects of drifting DSSD calibrations due to radiation damage. Thus, 0 mm simulations were constructed within the three dimensional parameter space of τ, R_p, and R_σ. At each step the χ^2 of the fit to the experimental DSSD spectrum was calculated by ROOT; the set of simulations at a single R_p exhibit a clear minimum in the plot of χ^2 against lifetime and minimal dependence upon R_σ. Details of the lineshape simulations and the lifetime analysis are presented here.

4.3.1 Specifics of Geant4/ROOT Simulations

Similar to the simulation discussions in Ch. 3, the ΔE lineshape simulations required an accurate parameterization of the experiment to properly describe the experimental geometry and silicon DSSD response, the secondary beam emittance and knockout reaction kinematics, and the two-proton decay process. The lack of certain production data, such as target-only unreacted beam and detector-only reacted beam runs, prevented the data-based constraint of several simulated parameters; examples were provided in Sect. 4.1. As noted there, the production of realistic ΔE lineshape simulations hinges upon accurately reproducing the reaction residue d_{ta} momentum distribution. Trajectory variations through the detector for a given residue also impact the energy loss simulations. Yet this trajectory spread is restricted by the S800 angular acceptance (7° and 10° in the dispersive and non-dispersive directions) to deviations less than 0.4%. Thus, the ΔE depends much more strongly upon the reaction residue momentum distribution. The steps towards obtaining accurate DSSD ΔE lineshapes are outlined below.

Beam Characteristics and Reaction Kinematics

The simulated ^{20}Mg secondary beam emittance and S800 detector response was parameterized by fitting the simulated a_{ta}, b_{ta}, y_{ta}, and d_{ta} S800 target spectra to their experimental counterparts from unreacted secondary beam data obtained prior to the installation of the particle plunger in the beam line. The energy and angular straggling introduced by the carbon target and silicon detector were constrained by similar fits to unreacted beam data obtained after the particle plunger installation. The absence of target-only data prevented the deconvolution of the straggling effects introduced separately by the target and detector.

Care was taken to accurately constrain the simulation parameters affecting the momentum distribution. First, the plunger target and detector thicknesses were fixed to the manufacturers' specifications. Next, the longitudinal momentum transfer from the one-neutron knockout reaction was tuned to achieve agreement between the simulated and experimental d_{ta} spectra. Note that in principle, the competing reactions $^{19}\mathrm{Mg} \rightarrow \mathrm{p} + \mathrm{p} + {}^{17}\mathrm{Ne}$ and $^{20}\mathrm{Mg} \rightarrow \mathrm{p} + \mathrm{p} + \mathrm{n} + {}^{17}\mathrm{Ne}$ on both the target and detector necessitate four separate parameterizations as they result in different ^{17}Ne momentum distributions and hence unique DSSD energy deposits. Yet for reasons discussed within Sect. 4.1, only an effective target-detector parameterization was implemented for each simulated R_p to properly fit the DSSD ΔE and d_{ta} spectra simultaneously. An example of the fit quality between the experimental S800 reaction residue target spectra and their simulated counterparts at $R_p = 0.55$ is illustrated in Fig. 4.5. Beam quality issues at the particle plunger target in the non-dispersive direction (manifest in the b_{ta} and y_{ta} spectra) were not simulated as this had negligible impact on the simulated DSSD lineshapes.

Silicon DSSD Response

Next, the simulated energy loss spectra (binned in MeV) were calibrated to the experimental spectra (binned in channels, and thus indicating relative energy loss in the detector) with unreacted beam data such that meaningful comparisons could be made. From a Gaussian fit to each unreacted beam energy loss signature, the simulated and experimental energy loss centroids were plotted against one another and from the least-squares linear fit, the calibration gain and offset parameters $a = 0.0315$ MeV/channel and $b = 2.11$ MeV were obtained, respectively.

For simplicity, the simulation regarded the DSSD as a passive silicon degrader. As such, the simulated detector response was strictly a function of the momentum and trajectory spread of the ionizing radiation. Therefore detector-specific sources of energy degradation [99–101], such as incomplete charge collection due to charge carrier trapping or recombination

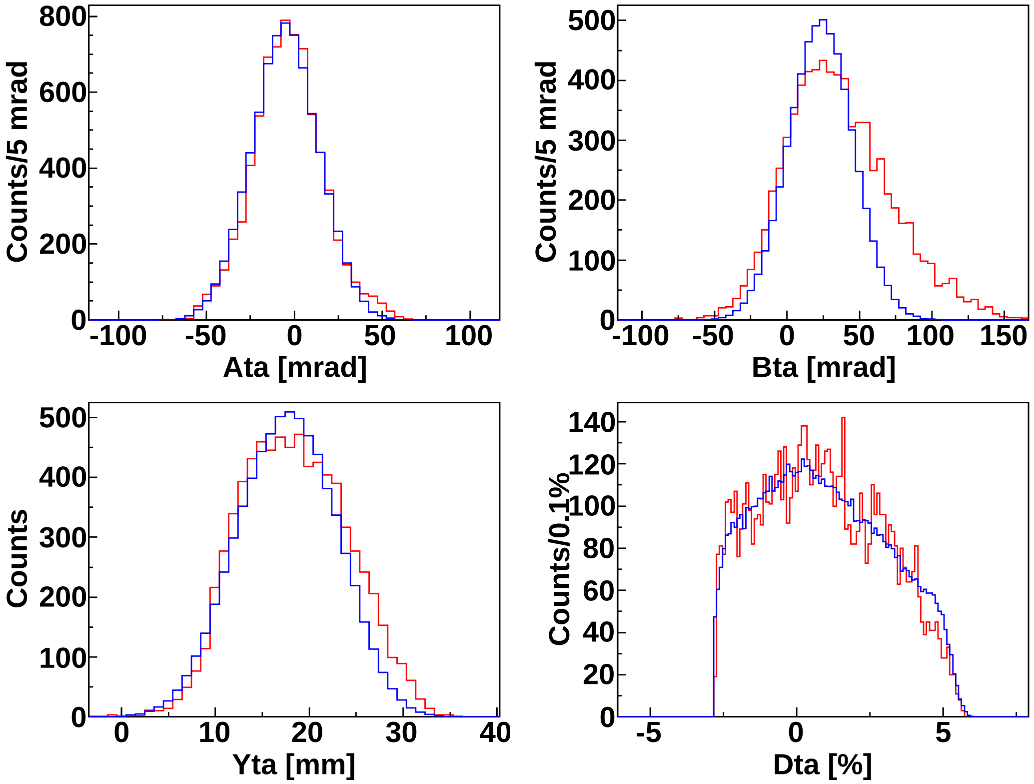

Figure 4.5: Fit of simulated (blue) and experimental (red) ^{17}Ne particle-gated S800 reaction residue target spectra. The angular distributions in the dispersive (a_{ta}) and non-dispersive (b_{ta}) directions, spread in non-dispersive position (y_{ta}), and kinetic energy deviation from that corresponding to a central trajectory through the S800 (d_{ta}) are obtained from inverse map trajectory reconstruction. See discussion within Subsect. 2.3.3 for more details.

effects, energy straggling introduced in the detector dead layers, and electronic noise were not explicitly accounted for. In addition, the energy loss lineshapes from reaction residues exhibited a right-skewed asymmetry. The underlying cause of this is a matter for future examination; it is likely to be a combination of correlated background events (discussed below) and lifetime effects.

Thus both effects were accounted for to produce proper lineshape fits. A detector response function was incorporated into the simulation based upon a general peak shape from the DAMM (Display, Analysis and Manipulation Module) software package [102]. On an event-by-event basis, the simulated raw energy loss E_{raw} (based solely upon momentum and trajectory variations through the detector) was taken as the centroid of a unique lineshape probability distribution function $P(x)$ of the form

$$P(x) = \begin{cases} \frac{1}{\sqrt{2\pi\sigma^2}} e^{-(x-x_0)^2/2\sigma^2} & \text{for } x < x_0 = E_{raw} \\ \frac{1}{\sqrt{2\pi\sigma^2}} e^{-(x-x_0)^2/\left[2\sigma^2\left[1+\frac{\epsilon(x-x_0)}{\sigma}\right]\right]} & \text{for } x \geq x_0 = E_{raw}. \end{cases} \tag{4.2}$$

A random number was then generated based upon the above probability distribution function and this value was passed as the simulated energy deposit for a single event. Both the standard deviation σ and the strength of the asymmetric high-energy tail ϵ were adjusted to properly fit the experimental DSSD lineshape. Figure 4.6 demonstrates the fit using this detector response implementation for unreacted beam energy loss data. Reacted beam ΔE fits are provided below. It should be noted that for unreacted beam data, the strength of the right-skewed parameter ϵ was found to be very small compared to that required to fit reacted beam data ($\approx 5\%$) and the width σ was only 80% that necessary for reacted beam data fits.

DSSD Lineshape Generation

Having constrained the ^{20}Mg secondary beam properties, parameterized the reaction kinematics, and modeled the silicon detector response to ionizing radiation, simulated reaction residue energy loss spectra were generated. This required two functions to adequately describe the experimental background shape and also the variation of the three previously mentioned parameters: the ^{19}Mg two-proton decay mean lifetime, the ^{17}Ne production mechanism ratio R_p, and the target-detector yield ratio R_σ. Each shall be discussed in turn.

There were two distinct types of background in the ΔE spectra. The low energy tails extending from the full energy deposit peaks in Fig. 4.3, 4.4, and 4.6 are well understood as a result of incomplete charge collection within the detector [103], variations in dead

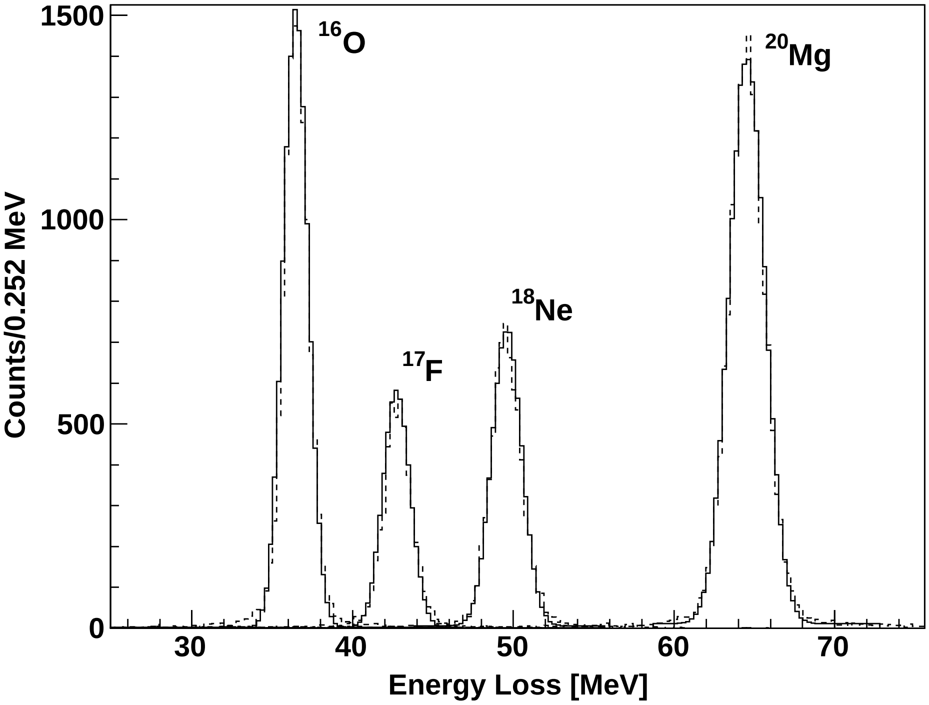

Figure 4.6: Experimental (dashed) and simulated (solid) DSSD energy loss lineshapes for the four dominant secondary beam components. Each labeled ΔE peak is from data gated on both the incoming and outgoing labeled species; the resulting four individual histograms were added together to produce a single spectrum.

layer thickness [99], and random background events. As the figures illustrate, this is a small effect ($<$ 2% for the ^{20}Mg peak in Fig. 4.6) and therefore a simple constant background was employed to account for these events. Future improvements will certainly involve more accurate reproductions of this shape; in the present analysis, more effort was dedicated to modeling the detector response and the second background type.

The origin of the high energy background events (i.e. the events in channels beyond 2250 in Fig. 4.4) in the incoming ^{20}Mg and outgoing ^{17}Ne particle-gated DSSD energy loss spectra is a subject for future analysis. The events cannot originate from $Z > 12$ contaminants—this possibility is entirely excluded by the particle gating condition used to generate the spectra. Nor can they be the coincident detection of the full set of decay daughters ^{17}Ne+p+p as the proton energies are similar to the reaction residue energies (~ 90 MeV) and thus the energy deposited by each is insufficient (< 1 MeV). A possible candidate may be the simultaneous detection of reaction residues in coincidence with dislodged target or detector nuclei.

For the present analysis, a phenomenological fit to these background events was performed. The functional form f of the background for channel x was chosen to be

$$f(x) = h \cdot arctan\left(\frac{x - x_0}{a}\right) exp\left(-\frac{x - x_0}{b}\right). \tag{4.3}$$

The arctangent function was chosen as it produces a rounded step function shape while the decaying exponential tail fits the background trend at high energies. Four parameters controlled the initial height h, the offset x_0, the roundedness of the step a, and the exponential decay constant b to best fit the background.

The four background parameters were adjusted to fit the high energy background events in the 0 mm DSSD energy loss spectrum. However, the ^{17}Ne particle-gated ΔE spectrum includes the finite lifetime effects of ^{19}Mg. To exclude these effects from contaminating the fit of the background parameters, a ^{18}Ne particle-gated DSSD energy loss spectrum was used instead. The ^{18}Ne reaction channel was populated either directly from the two-proton knockout of the secondary beam by $^{20}\text{Mg} \rightarrow \text{p} + \text{p} + {}^{18}\text{Ne}$ or from the one-proton decay of ^{19}Na which immediately proceeds from the one-proton knockout reaction $^{20}\text{Mg} \rightarrow \text{p} + {}^{19}\text{Na}$. The ^{19}Na ground state is unbound to proton emission by roughly 320 keV [104] and has a $1p$ decay lifetime on the order of femtoseconds from Shell Model calculations of the proton decay width [105]. Both production mechanisms result in the immediate production of ^{18}Ne and the resulting DSSD spectrum exhibits no lifetime effect within the experimental sensitivity.

Thus the four high energy background parameters were fixed to fit the high energy events in the ^{18}Ne particle-gated spectrum. It was decided to offset $f(x)$ to the center of the ^{18}Ne energy loss peak, although both this choice and that of the roundedness a are somewhat

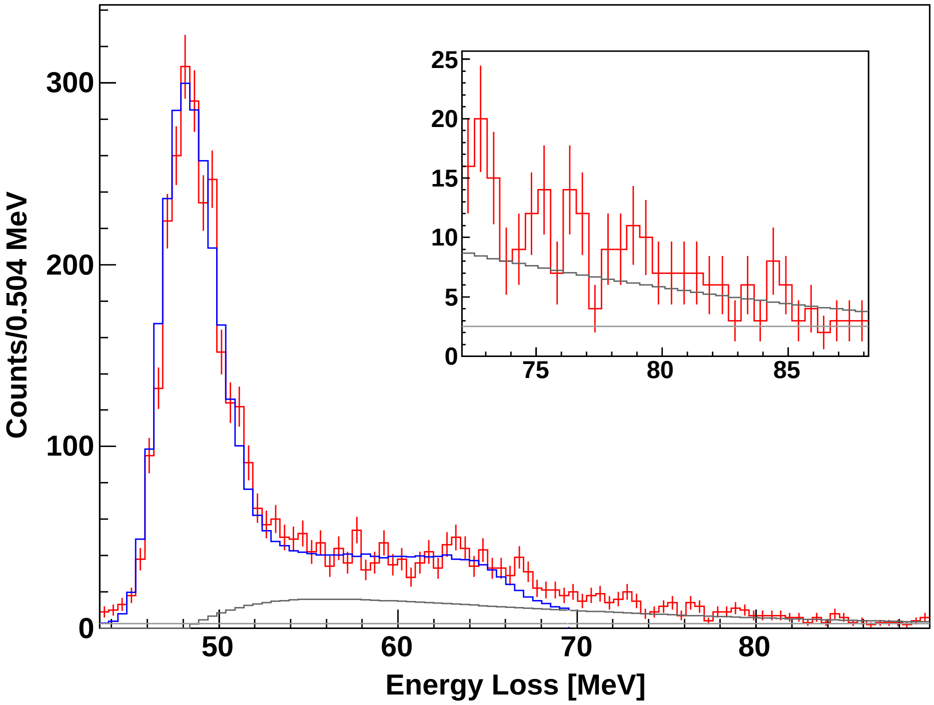

Figure 4.7: ^{18}Ne particle-gated silicon DSSD ΔE spectrum at a target-detector distance of 0 mm (red) with statistical uncertainties. The simulated lineshape (blue) was constructed assuming a 0 ps one-proton decay lifetime of ^{19}Na and includes contributions from the high energy background function $f(x)$ (dark gray) and the constant background (light gray). The inset displays the high-energy background events, the constant background, and $f(x)$ of Eq. 4.3 with parameters $h = 25$, $x_0 = 48.4$ MeV, $a = 10$ MeV, and $b = 35$ MeV.

arbitrary. The implementation of this background is illustrated in the inset of Fig. 4.7. For the ^{19}Mg lifetime simulations, the roundedness and exponential decay constant parameters (a and b) were held fixed while the offset x_0 was adjusted to the center of the ^{17}Ne peak and the height h was scaled by the ratio of counts in the ^{17}Ne and ^{18}Ne particle-gated spectra.

Next, the yield ratio R_σ of the one-neutron knockout reaction $^{20}\mathrm{Mg} \rightarrow \mathrm{n} + {}^{19}\mathrm{Mg}$ on the carbon target and silicon DSSD was constrained. Cross section ratio estimates within LISE++ using the fragmentation parameterizations EPAX 2.15 [106] and Abration Ablation [107,108] gave $R_\sigma = 2.9$ and 3.3, respectively. In addition, cross section calculations at beam energies of 80, 85, and 90 MeV/u produced a similar ratio of 3.2 [109]. Furthermore, both EPAX 2.15 and Abration Ablation calculations gave the exact same R_σ values as above for the similar nucleon knockout reaction ^{20}Mg $\rightarrow$ p + ^{19}Na. Simulations of the ^{19}Na $1p$ decay with $\tau = 0$ ps were fit to the ^{18}Ne particle-gated ΔE lineshapes. The best fits were in the range $R_\sigma = [3.03, 3.43]$. Therefore several target-detector yield ratios within this range, well constrained by both calculations and data, were used for ^{19}Mg lifetime analysis.

The single largest uncertainty in the measurement was the ^{17}Ne production mechanism ratio R_p of Eq. 4.1. Simple LISE++ calculations produced ratios of nearly 0.06 and 0.25 using Abration Ablation and EPAX 2.15 parameterizations, respectively. This ratio could not be constrained with the experimental data or from previous work in the literature. It was therefore decided to extract the two-proton decay lifetime as a function of R_p. A large simulated production mechanism ratio, corresponding to the majority of ^{17}Ne production from the dissociation of ^{20}Mg, required a longer ^{19}Mg lifetime to properly fit the energy loss data. Conversely, a small ratio, corresponding to the majority of ^{17}Ne production from the two-proton decay of ^{19}Mg, required a short lifetime to fit the data.

4.3.2 Two-Proton Decay Lifetime of ^{19}Mg

DSSD energy loss spectra were simulated with all the parameters modeling the secondary beam emittance, reaction kinematics, silicon detector response to ionizing radiation, and the high energy background function of Eq. 4.3 constrained as discussed in the previous subsection. Lineshapes were generated for the 0 mm distance over a range of lifetimes for each input production mechanism ratio and target-detector yield ratio. The reduced χ^2 (χ^2_ν) of the fit between the simulated and experimental energy loss spectra was calculated within ROOT. For each R_p-R_σ pair, the mean lifetime of the two-proton emitter ^{19}Mg was extracted from the minimum of a polynomial fit to the χ^2_ν lifetime distribution.

Energy loss lineshape simulations were performed over a range of ^{19}Mg lifetimes for

Table 4.2: ^{19}Mg lifetime (picoseconds) dependence on R_p and R_σ. See text for details.

		$\mathbf{R_p}$									
		0.05	0.15	0.25	0.35	0.45	0.55	0.65	0.75	0.85	0.95
$\mathbf{R_\sigma}$	3.03	0.32	0.35	0.41	0.43	0.54	0.68	0.88	1.24	2.32	7.52
	3.23	0.35	0.39	0.46	0.49	0.60	0.76	0.96	1.35	2.44	7.26
	3.43	0.39	0.42	0.50	0.54	0.66	0.82	1.04	1.45	2.59	7.37

ten ^{17}Ne production mechanism ratios from 0.05 to 0.95 in increments of 0.1. This process was repeated three times at target-detector yield ratios of 3.03, 3.23, and 3.43. A variable normalization factor was implemented to account for statistical differences between the simulation and the data. Each simulation used the same functions to describe the experimental background and detector response, but as mentioned previously, each R_p required slightly different parameterizations of the longitudinal momentum distribution to simultaneously fit the d_{ta} and ΔE spectra. Distributions of χ^2_ν values from the fits were constructed for all thirty R_p-R_σ pairs and fit with cubic polynomials. The best-fit lifetimes were then extracted from the minima. Table 4.2 summarizes the results. With the exception of the final column, smaller yield ratios, which correspond to more reactions on the silicon detector, result in shorter best-fit lifetimes as expected. Note that for a given R_p, the spread of lifetimes from the three target-detector yield ratios is insignificant compared to the overall uncertainty introduced by the unconstrained ^{17}Ne production mechanism ratio.

The three panels of Fig. 4.8 indicate the sensitivity of nine sample fits with production mechanism ratios of $R_p = 0.35$, 0.55, and 0.75 and yield ratios of $R_\sigma = 3.03$, 3.23, and 3.43. The lifetime sensitivity is enhanced for small values of R_p as expected; with limited contributions from the breakup $^{20}\text{Mg} \rightarrow \text{p} + \text{p} + \text{n} + {}^{17}\text{Ne}$, the intensity ratio of the small ^{19}Mg and prominent ^{17}Ne energy loss peaks is heavily dependent upon the two-proton decay lifetime. Statistical errors were taken from the cubic polynomials fit to the χ^2_ν values in the same manner as in Ch. 3. The main contribution to the systematic error was taken to be

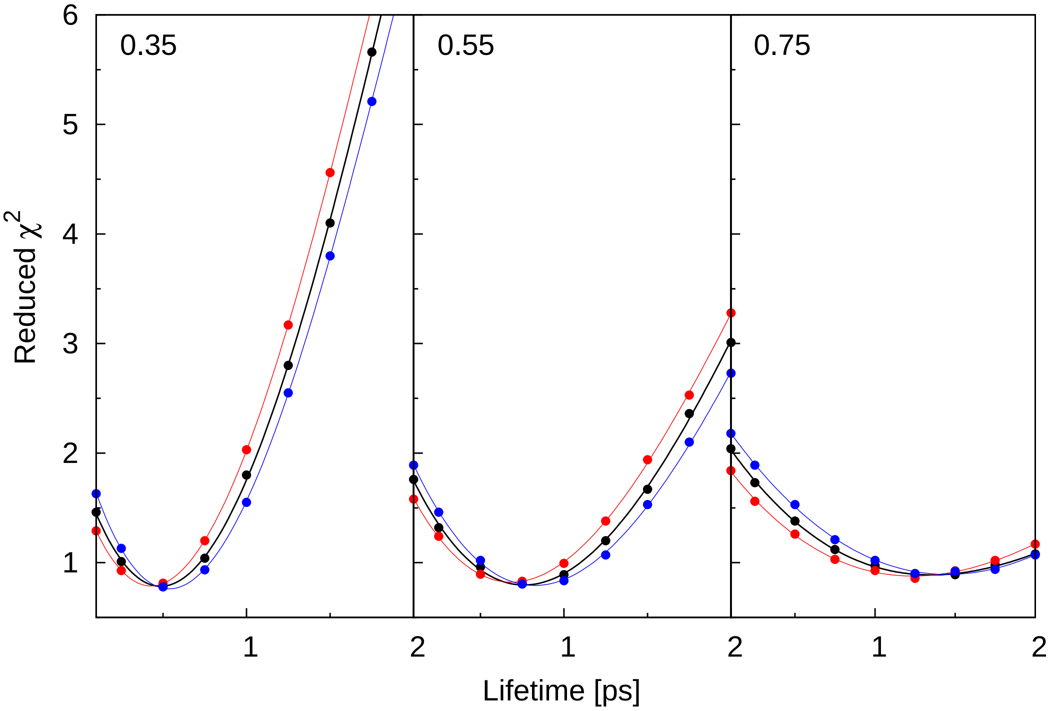

Figure 4.8: χ^2_ν from the fit of simulated ΔE lineshapes to 0 mm experimental data for ^{17}Ne production mechanism ratios of 0.35, 0.55, and 0.75 and target-detector yield ratios of 3.03 (red), 3.23 (black), and 3.43 (blue). Table 4.2 lists the best-fit ^{19}Mg lifetimes, extracted from the minima of the cubic polynomial fits.

the average spread of best-fit lifetimes from simulations at the upper (3.43) and lower (3.03) limits of R_σ. Other sources of systematic error are discussed within Sect. 5.2 of Ch. 5.

The four plots in Fig. 4.9 illustrate the sensitivity of the simulated ΔE lineshape features to small changes in lifetime. The χ^2_ν was calculated by ROOT from the fit over the entire range of the simulated lineshape (blue). The superior fit of $\tau = 0.76$ ps simulation is clear; this lifetime value was extracted from the minimum of the black curve in the middle panel of Fig. 4.8.

Figure 4.10 plots the $R_\sigma = 3.23$ data from Tab. 4.2 to illuminate the general lifetime trend as a function of an increasing R_p (red points). The sum of the statistical and total systematic uncertainties discussed above was taken as the error in the best-fit lifetime at each

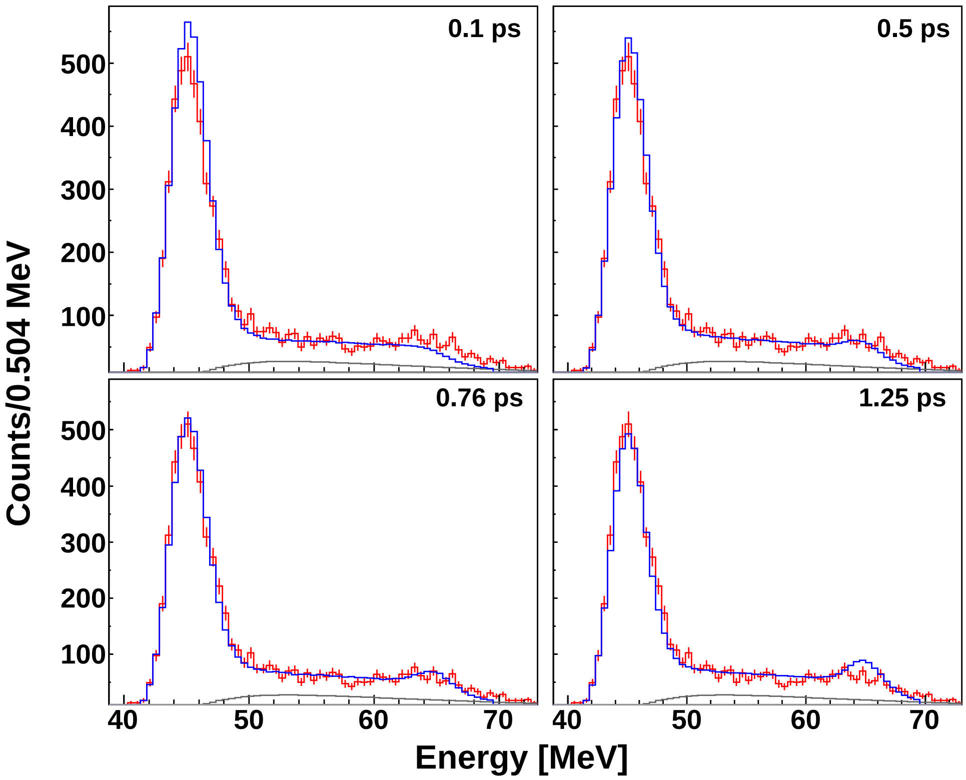

Figure 4.9: ^{17}Ne particle-gated silicon energy loss spectra at a target-detector distance of 0 mm. The fit between experimental data (red, with statistical uncertainties) and simulated lineshapes (blue) produced with $R_p = 0.55$ and $R_\sigma = 3.23$ is plotted for four simulated lifetimes of $\tau = 0.1$, 0.5, 0.76, and 1.25 ps.

R_p and is included in the figure. No minimum was obtained for the χ^2_ν fits of the $R_p = 0.95$ lifetime scan. Rather, the distribution flattened out. For $R_\sigma = 3.23$ this occurred at 7.26 ps and therefore this value has been taken as a lifetime lower limit at $R_p = 0.95$. Within the reasonable range of ^{17}Ne production mechanism ratios 0.15 to 0.85 (see discussion in Ch. 5), the extracted lifetimes span the range from 0.39(9) ps to 2.44(54) ps.

The ^{19}Mg two-proton decay lifetime results of Ref. [38] are also plotted in Fig. 4.10 for comparison (black points). The quoted value of $\tau = 5.8 \pm 2.2$ ps at $R_p = 0.25$ is given, along with lifetimes of 4.5 ± 1.5 ps and 9^{+3}_{-6} ps derived at $R_p = 0.0$ and 0.65, respectively, from the same work. (The $R_p = 0.0$ data has been shifted off the ordinate for clarity.) The obvious disparity between the two measurements can only be resolved at the two-sigma level for the

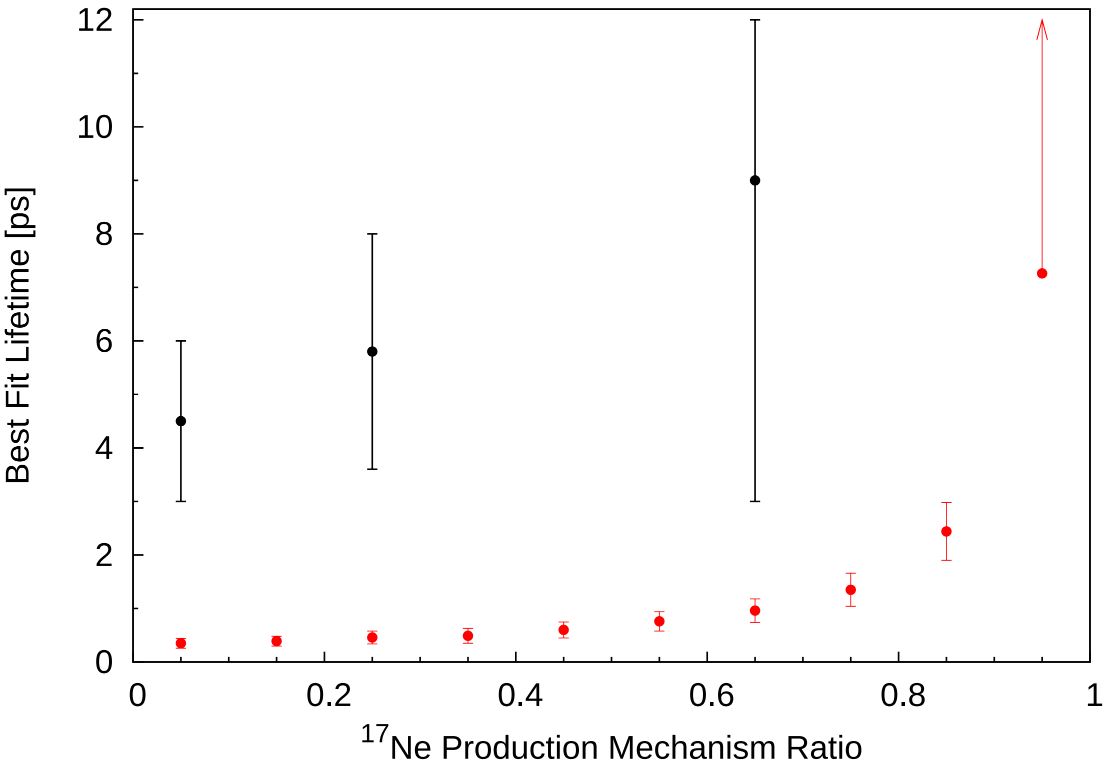

Figure 4.10: Best-fit ^{19}Mg ground state two-proton decay lifetime as a function of increasing ^{17}Ne production via the dissociation $^{20}\mathrm{Mg} \rightarrow \mathrm{p} + \mathrm{p} + \mathrm{n} + {}^{17}\mathrm{Ne}$ (red points). The error bars indicate the sum of the statistical and systematic uncertainties. The literature values [38] are plotted for comparison (black points). See text for details.

$R_p = 0.65$ result or if the two experimental techniques probed different ^{17}Ne production ratios.

Plotting the χ^2_ν of the lineshape fits to the experimental energy loss spectrum for all simulated R_p and lifetime values results in a two dimensional χ^2_ν hypersurface. Figure 4.11 illustrates this hypersurface from scans with $R_\sigma = 3.23$. The plot indicates the χ^2_ν valley, representing the extracted lifetimes given in the second row of Tab. 4.2, trends towards larger lifetimes with increasing production of ^{17}Ne via the direct breakup of ^{20}Mg. The same trend was depicted in Fig. 4.10; here, the lack of lifetime sensitivity at $R_p = 0.95$ is clear.

The lifetime results presented here for the two-proton emitter ^{19}Mg are discussed further

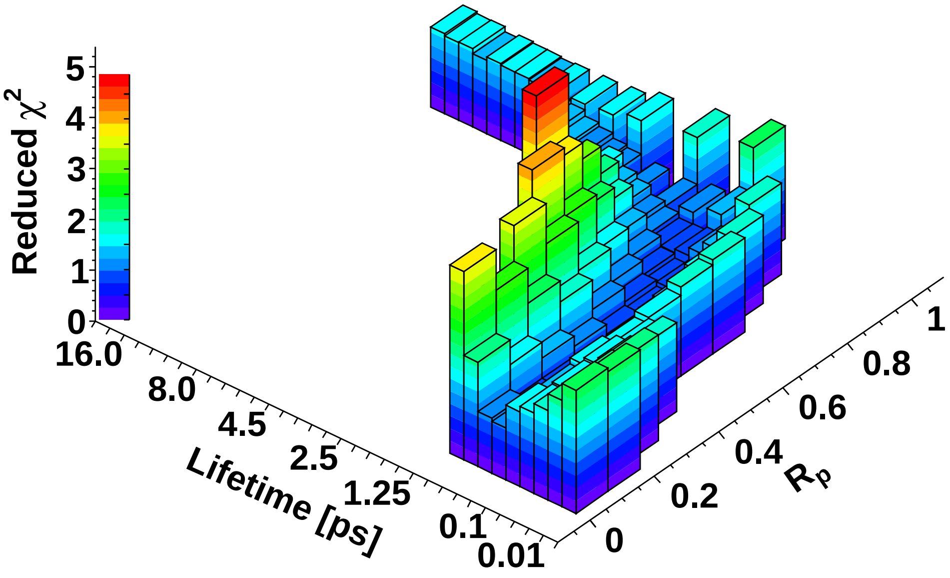

Figure 4.11: χ^2_ν of the energy loss lineshape fits to the 0 mm experimental data from various input τ and R_p values at a fixed target-detector yield ratio of 3.23. For display purposes, the lifetime axis is non-linear. The bins—each corresponding to a single lifetime simulation point—are of equal width regardless of the spacing between consecutive simulated points.

in Ch. 5. The permissible range of lifetimes determined by this work is inconsistent with the result reported in Ref. [38], but lends credence to this proof of concept study. Within this context, a brief prospectus outlining opportunities for future study and improvements of charged-particle lifetime measurements at NSCL with the particle plunger shall be given.

Chapter 5

Discussion

5.1 ^{18}C Commentary

The lifetime measurement of the $2_1^+ \to 0_{gs}^+$ transition in ^{18}C via the Recoil Distance Method was presented in Ch. 3. The mean lifetime of $22.4 \pm 0.9(\text{stat})^{+2.5}_{-1.6}(\text{syst})$ ps is in agreement with the literature value $18.9 \pm 0.9(\text{stat}) \pm 4.4(\text{syst})$ ps reported in [29]. The lifetime is inversely proportional to the electromagnetic transition rate and thus the reduced quadrupole transition strength $B(E2; 2_1^+ \to 0_{gs}^+)$ was determined via Eq. 1.9 to be $3.64^{+0.46}_{-0.48}$ e^{2}fm^4. A 932 keV gamma-ray transition was observed to feed the 2_1^+ level from above. Though this higher-lying state was populated with an intensity only 25% that of the first 2^+ state, a lifetime upper limit $\tau < 4.5$ ps was extracted. This quantitative lifetime measurement is the first of its kind for states above the first 2_1^+ in even-even carbon isotopes with $N > 8$.

The observed excited state properties are summarized in Tab. 5.1. There, the assumed J^π assignment of 2_2^+ for the observed 2_1^+ feeder level shall prove convenient for comparison with *ab initio* theoretical calculations in Subsect. 5.1.2.[1] In addition, shell model calculations

---

[1] Experimental spin and parity assignments for excited states populated by nucleon knockout reactions from gamma-ray spectroscopy with SeGA are daunting (*c.f.* Ref. [86,110]) and not feasible for the measurement presented here.

Table 5.1: Measured electromagnetic transition properties of ^{18}C excited states.

Observable	Experiment	Unit
$E(2_1^+ \to 0_{gs}^+)$	1585(19)	keV
$E(2_2^+ \to 2_1^+)$	932(11)	keV
$\tau(2_1^+)$	$22.4^{+3.4}_{-2.5}$	ps
$\tau(2_2^+)$	< 4.5	ps
$B(E2; 2_1^+ \to 0_{gs}^+)$	$3.64^{+0.46}_{-0.48}$	e^{2}fm^4

with the WBP interaction [111] also predict the second excited state to be 2^+ [5]. From the lifetime upper limit of this state, a reference lower limit $B(E2; 2_2^+ \to 2_1^+) = 8.1$ e^{2}fm^4 is calculated. This is just an estimate; a mixing ratio ($\delta \propto E_\gamma \sqrt{B(E2)/B(M1)}$) of $-0.18(15)$ was adopted from the $2_2^+ \to 2_1^+$ transition in ^{16}C [112] and 100% branching was assumed from the non-observation of a 2517 keV transition to the ground state. If instead a pure $E2$ transition is assumed, the lower limit $B(E2; 2_2^+ \to 2_1^+)$ increases thirty fold to 257 e^{2}fm^4. Note that the selection rules from Appendix A also permit an $M3$ or $E4$ transition, but both can be excluded as lower multipoles dominate higher ones.

With the aid of Eq. A.3, the single-particle Weisskopf estimate of $B(E2; 2_1^+ \to 0_{gs}^+)$ is found to be $B_W(E2) = 2.8$ e^{2}fm^4. The ratio of the experimental reduced quadrupole matrix element to the single-particle value (Eq. 1.17) indicates the degree of collectivity for the excited state. The deduced ratio of $B_{exp}/B_W = 1.3$ is near unity and suggests the excitation should be well described within the framework of the single-particle shell model. This will be demonstrated below.

The experimental results tabulated in Tab. 5.1 serve as useful probes of the nuclear structure of ^{18}C. In particular, the electric quadrupole transition strength is a powerful indicator of changes in shell structure [23]. The discussion provided immediately below illustrates this fact; there the near constancy of $B(E2; 2_1^+ \to 0_{gs}^+)$ values for neutron-rich carbon isotopes is explored. The measurements are also valuable benchmarks which can hone the predictive power of various nuclear models. In turn, accurate models can help interpret data and identify interesting objects for future studies. RDM lifetime measurements are certain to play an important role as this mutual feedback loop advances the forefront of the field; thus the section concludes with a few general suggestions and comments regarding future Köln/NSCL plunger measurements.

5.1.1 Nuclear Structure of Neutron-Rich Carbon Isotopes

The final remarks surrounding Eq. 1.18 in Ch. 1 alluded to the marked deviation of ^{16,18}C from the systematic liquid drop behavior $B(E2) \propto E(2^+)^{-1}$ with respect to ^{14}C as evidence for a very different excitation mechanism. Indeed, the hindered $B(E2)$ observed in ^{16,18}C with respect to other light open-shell nuclei [28, 29] has been reported by some to indicate exotic proton and neutron decoupling modes [113]. The divergence from expected behavior is demonstrated in Fig. 5.1, where the $B(E2)$ values (main plot) for ^{14,16,18}C remain relatively constant while the $E(2_1^+)$ (inset) drops significantly from nearly 7.0 MeV for ^{14}C to less than 2.0 MeV for ^{16,18}C. The present ^{18}C results, together with previous measurements of ^{16,18,20}C (Ref. [28,29,79]), can systematically deduce the degree of quadrupole collectivity for the 2_1^+ excitations of these neutron-rich carbon isotopes. It will be shown below that simple shell model calculations suffice to describe the observed behavior of neutron-rich carbon isotopes without evoking exotic decoupling modes.

The four valence protons of ^{18}C completely fill the $\pi 0p_{3/2}$ orbital. Shell model calculations discussed in Ref. [29] for ^{16,18}C indicate a large energy gap between the $\pi 0p_{3/2}$ and $\pi 0p_{1/2}$ orbitals. It can therefore be expected that the 2_1^+ excited state is dominated by neutron contributions. However, the quadrupole transition strength is strictly an electromagnetic phenomenon and therefore neutrons cannot contribute directly. Instead, the valence neutrons (all in the $\nu 0d_{5/2}$ shell for $^{16-20}$C, but with a strong admixture of $\nu 1s_{1/2}$ contributions due to the disappearance of the $N = 14$ subshell closure for carbon isotopes [5] which induces a near degeneracy between $\nu 0d_{5/2}$ and $\nu 1s_{1/2}$ orbitals) couple to the proton core. This

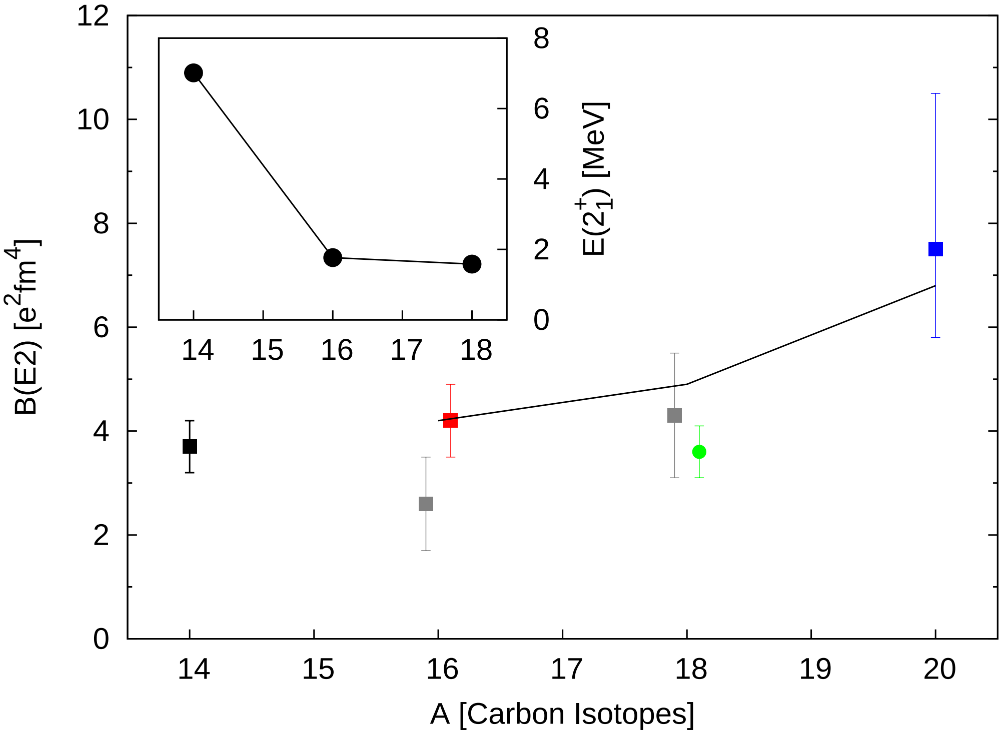

Figure 5.1: Observed $B(E2; 2_1^+ \rightarrow 0_{gs}^+)$ trend for even-even $14 \leq A \leq 20$ carbon isotopes (main plot). The squares indicate measured $B(E2)$ data for ^{14}C (black) [27], ^{16}C (red) [28], ^{16,18}C (gray) [29], and ^{20}C (blue) [79]. The green circle is taken from the present work discussed in Ch. 3. $B(E2)$ shell model calculations for ^{16,18,20}C are given by the black line and are discussed in Ref. [79]. See text for more details. The relatively constant $B(E2)$ for ^{14,16,18}C together with the $E(2_1^+)$ trend (inset) demonstrates the marked deviation from even-even isotope global systematics of Ref. [26].

collective behavior induces polarization of the proton core and the $B(E2)$ transition strength is indicative of the extent of this core polarization. The polarization effects are weaker at large isospin (small neutron binding energies) [114], as the spatially extended neutrons with increasing $\nu 1s_{1/2}$ admixtures induce polarization less efficiently.[2]

Therefore a relatively hindered core polarization and suppression of proton excitations leads to the small $B(E2)$ values observed in ^{16}C [28, 29] and ^{18}C (as presented in Ch. 3 and Ref. [29]). In addition, the transition strength should increase for ^{20}C due to the monopole

---

[2] It is interesting to note that this spatially extended $\nu 1s_{1/2}$ orbit also plays a vital role in the known halo configuration of ^{19}C [115, 116].

interaction of the tensor force [117], where the $\nu 0d_{5/2}$ orbital is filled and therefore the attractive $\nu 0d_{5/2} - \pi 0p_{3/2}$ and repulsive $\nu 0d_{5/2} - \pi 0p_{1/2}$ interactions reduce the shell gap between the two proton $0p$ orbitals. Thus the $B(E2)$ strength contribution from proton excitations is enhanced, as has been observed [79].

The observed behavior of the $B(E2; 2^+_1 \rightarrow 0^+_{gs})$ values for neutron-rich carbon isotopes can be reproduced with shell model calculations discussed in Ref. [79]. This is illustrated in Fig. 5.1 where $B(E2)$ data and calculations are shown as a function of neutron number. The calculations were constructed from

$$B(E2; 2^+_1 \rightarrow 0^+_{gs}) = \frac{1}{2J_i + 1} \left| M_p e_p + M_n e_n \right|^2 , \tag{5.1}$$

where J_i is the spin of the initial state and $M_p(M_n)$ are the shell model proton(neutron) matrix elements coupling the two states of the $2^+_1 \rightarrow 0^+_{gs}$ transition. The e_p and e_n are the isospin-dependent proton and neutron effective charges as parameterized in Ref. [118]. The effective charges are introduced to account for contributions to the quadrupole transition strength from excitations outside of the truncated shell model space. They are useful here as they quantify the core polarization; e_p and e_n will approach the canonical charge values of $+1e$ and 0, respectively, as the core polarization disappears. The numerical values for both the matrix elements and effective charges were extracted from Ref. [79].

The agreement between the calculations and data presented in Fig. 5.1 presents clear evidence that the collective behavior of neutron-rich carbon isotopes can be described within the shell model utilizing isospin-dependent effective charges. Strong proton-neutron decoupling did not need to be invoked, but rather a lessening of neutron-proton core polarization due to the spatial extent of $\nu 1s_{1/2}$ valence neutrons. More immediately important is the excellent agreement between the $B(E2)$ derived from the current lifetime measurement and that of the previous study [29].

5.1.2 Comparison to *ab initio* NCSM

The ^{18}C excited state lifetime measurements presented in Ch. 3 and discussed above provide a unique opportunity to test the accuracy of *ab initio* calculations, such as the no-core shell model (NCSM) [12]. This fundamental theoretical approach begins with realistic two- and three-nucleon interactions and the full set of nucleon degrees of freedom. A brief description of the *ab initio* NCSM and several pertinent definitions were provided in Sect. 1.2. Here, a set of NCSM calculations performed by Ref. [15] are compared to the ^{18}C electromagnetic transition data.

Besides the extreme neutron-to-proton ratio of ^{18}C, which as shown above can result in interesting quadrupole excitation behavior, this $A = 18$ system is slightly beyond current computational limits for full NCSM calculations. For example, extracting stable excitation energies for low-lying states requires a very large model space and prohibits results for $A > 16$ [119]. To extend the applicability of *ab initio* NCSM to either heavier nuclei or larger model spaces, approximations such as the importance-truncation (IT) scheme [16, 17] must be applied.

In the IT-NCSM approach, unimportant basis states are first identified with many-body perturbation theory and then removed prior to the full matrix eigenvalue calculation. A substantial number of basis states are irrelevant for the description of low-lying excited states and therefore removing these inconsequential states truncates the model space without compromising predictive power. Using this reduced model space extends *ab initio* NCSM predictions to heavier nuclei and higher harmonic-oscillator excitations. The approach has been tested with calculations of properties of the stable nuclei ^{4}He, ^{16}O, and ^{40}Ca [17], as well as light radioisotopes of helium [16]; the present discussion marks a vital benchmark test for the scheme's applicability to heavier short-lived radioactive nuclei.

Large-scale *ab initio* NCSM calculations were performed for the low-lying excited states of ^{18}C using two different realistic nucleon-nucleon interactions: CD-Bonn 2000 [9] and

INOY [120]. The former provides a charge-dependent potential, built upon fits to global proton-proton and neutron-proton scattering data with an excellent χ^2/datum $\sim$ 1, while the latter introduces non-local interactions to account for three-body effects without explicitly including them. For brevity, only the CD-Bonn based calculations will be compared with the experimental data. A more complete comparison will be provided in a forthcoming paper. From the two-body realistic potentials, effective interactions were derived to accelerate convergence issues introduced by strong short-range nucleon-nucleon correlations. No adjustable parameters or effective charges were used in the NCSM calculation. The calculations were performed using harmonic-oscillator (HO) basis states constrained by a total HO energy cutoff characterized by a maximum number of HO excitations N_{max} above the ground state.

The results exhibited a dependence upon both N_{max} and the HO frequency $\hbar\Omega$ that is expected to disappear as the model space is increased [14]. This implies that N_{max} sequences obtained at different $\hbar\Omega$ values should all eventually converge to the same result. Thus the fits of multiple sequences can be constrained to converge at the same result [13]. To this end, the calculations employed as large an N_{max} basis as feasible over a wide range of $\hbar\Omega$ and extrapolated the calculated observables to infinite space. As the computational limit for full space ^{18}C calculations is $N_{max} = 6$, the importance-truncation scheme was employed to extend the calculations to $N_{max} = 8$, thereby improving the reliability of the infinite space extrapolation. Figure 5.2 presents the NCSM full space (closed squares) and importance-truncated (open squares) results as well as the extrapolations for two of the observables considered.

Table 5.2 presents a comparison of the extrapolated NCSM results to the corresponding ^{18}C experimental measurements. In particular, the 2_1^+ excitation energy and the calculated $B(E2; 2_1^+ \rightarrow 0_{gs}^+) = 4.3(5)$ e^{2}fm^4 are in excellent agreement with the experimental results. The calculated quadrupole moments for the two 2^+ states are $Q(2_1^+) = +3.8(1)$ efm^2 and $Q(2_2^+) =$ -3.8(2) efm^2. An infinite space extrapolation for the 2_2^+ excited state would permit

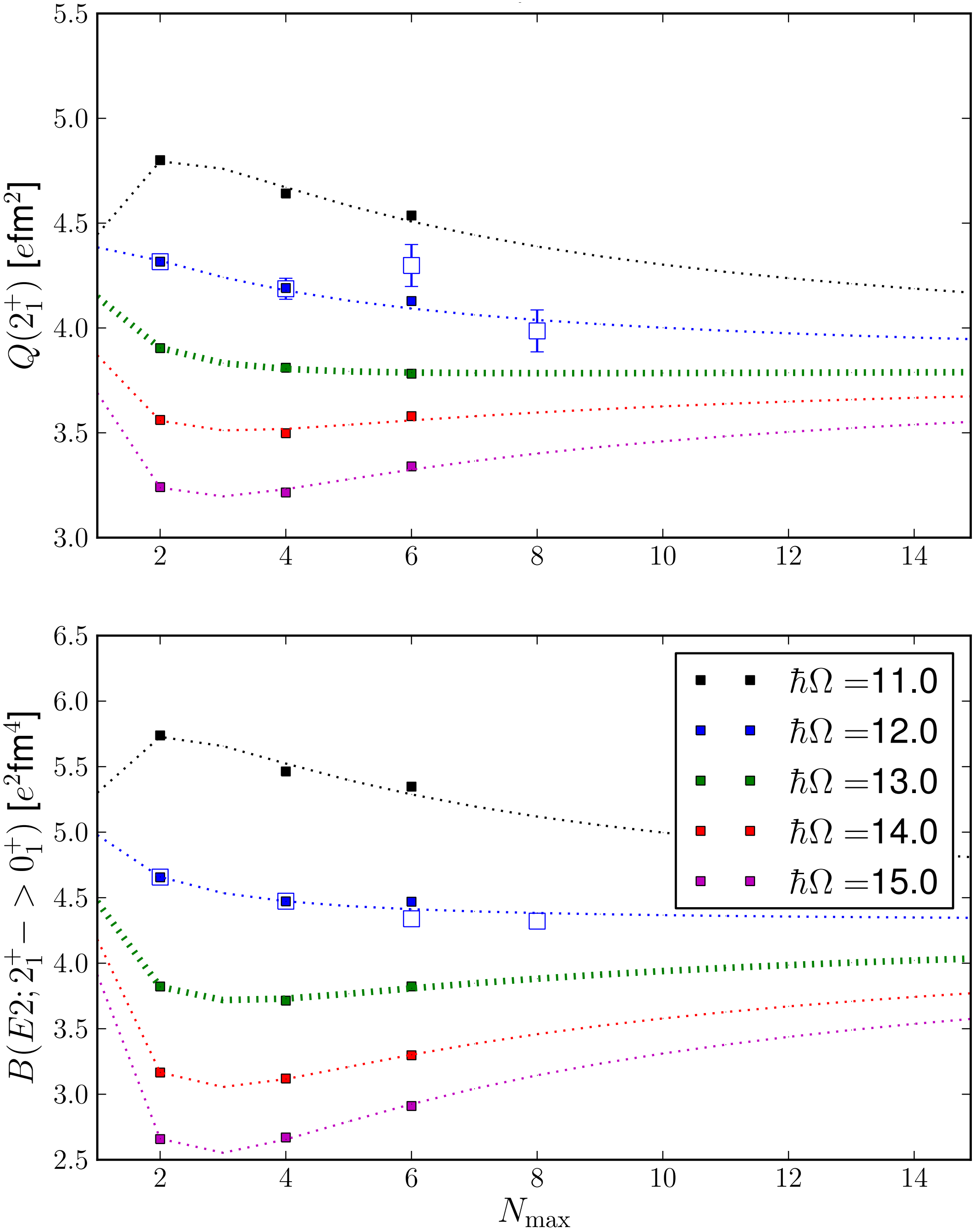

Figure 5.2: *Ab initio* NCSM results from Ref. [15] for electromagnetic observables of the 2_1^+ excited state in ^{18}C illustrating the N_{max} dependence of $Q(2_1^+)$ and $B(E2; 2_1^+ \rightarrow 0_{gs}^+)$ calculated with the CD-Bonn 2000 interaction. The filled (open) squares correspond to full (importance-truncated) model space results. Each extrapolation curve corresponds to the sequence of results obtained at a fixed HO frequency. The quoted theoretical results in Tab. 5.2 are derived from the calculated convergence of the extrapolation curves.

Table 5.2: *Ab initio* no-core shell model calculations of low-lying ^{18}C electromagnetic transition properties [15] compared to the experimental results tabulated in Tab. 5.1. The theoretical $E(2_2^+)$ value is from a preliminary $N_{max} = 2$ calculation; the full extrapolated value was not calculated.

Observable	Experiment	Theory	Unit
$E(2_1^+)$	1.585(19)	1.5(4)	MeV
$B(E2; 2_1^+ \rightarrow 0_{gs}^+)$	$3.64^{+0.46}_{-0.48}$	4.3(5)	e^2fm^4
$Q(2_1^+)$	—	+3.8(1)	efm^2
$E(2_2^+)$	2.517(22)	3.2(4)	MeV
$Q(2_2^+)$	—	−3.8(2)	efm^2

a meaningful comparison to the data, but only some of the properties of the two lowest ^{18}C excited states (2_1^+ and 2_2^+) were converged due to the complexity of the calculation. However, in a much smaller model space calculation ($N_{max} = 2$) the properties of many states were calculated, including the 2_2^+ excitation energy $E(2_2^+) = 3.2(4)$ MeV.

5.1.3 Suggestions and Outlook

The successful lifetime measurement presented in Ch. 3 and discussed here serves to further validate the Köln/NSCL plunger RDM technique with fast radioactive beams. This work has been unique; as part of a larger campaign it has aided in deciphering the evolution and degree of quadrupole collective behavior in the neutron-rich ^{16,18,20}C isotopic chain. Together, the results are well described within the shell model (Subsect. 5.1.1) using isospin-dependent effective charges. Alone, the current ^{18}C results agree well with the literature value [29], but are reported with greater precision. In addition, the observation and analysis of two electromagnetic transitions in this exotic isotope with a 2:1 neutron-to-proton ratio has provided a benchmark for reliable *ab initio* no-core shell model calculations far from stability. As shown in Subsect. 5.1.2, the $E2$ transition properties of the first excited state are well reproduced; more work must be done to achieve agreement for the higher-lying state. In light of the successes reported here and in past NSCL plunger lifetime measurements [21,22,78,79], the Köln/NSCL plunger technique will continue to play an important role in elucidating the nuclear structure of exotic radioactive isotopes. In the spirit of continual improvement, several practical suggestions are offered below and a brief outlook is presented.

The dominant source of systematic error in the ^{18}C analysis was an uncertainty in the ratio of excited-state production on the target and degrader. A satisfactory constraint of this ratio was obtained from a two dimensional χ^2 minimization by varying both the ratio and the lifetime and fitting the resulting simulated lineshapes to the gamma-ray energy spectra. However the construction of the χ^2 hypersurface is computationally intensive. A much simpler solution is to collect gamma-ray data at the "infinite distance" (Subsect. 3.3.2) such that any observed radiation emitted downstream of the degrader is directly attributable to reactions on the degrader. This data simultaneously reduces systematic uncertainties and accelerates the analysis.

In addition, the employed Geant4 Monte-Carlo simulations were shown to accurately reproduce all of the key experimental features that impact the gamma-ray energy lineshapes including the experimental geometry, the reaction residue momentum distribution, and the photon detection efficiencies. Future plunger data will undoubtedly be analyzed within a similar framework. It would therefore be advantageous to add the following to the simulations: a more complete description of the plunger geometry and the capability to generate an anisotropic gamma-ray angular distribution within the rest frame. These augmentations would enhance the realistic description of experiment.

The first suggestion entails the addition of the plunger foil mounting hardware—including the aluminum cones supporting the foils and the rigid structures affixing the cones to the plunger body—into the simulation. The attenuation of low energy gamma rays within these structures may influence the intensity ratio of photopeaks from decays upstream and downstream of the degrader. This is not accounted for in the simulation and may skew the lifetime analysis. Furthermore, it is difficult to simply quantify this effect with gamma-ray source measurements as the effect depends upon the emission point z (and thus the lifetime) of the nucleus.

The second suggestion would also improve the simulation's ability to accurately reconstruct all pertinent experimental parameters. The present implementation uses an isotropic angular distribution in the rest frame which is then Lorentz boosted into the laboratory frame. The boosted angular distribution integrated over θ is different for the forward and backward rings. More importantly, the relativistic boost is velocity-dependent and hence it differs for decays occurring upstream or downstream of the degrader. Therefore the photopeak intensity ratios are unique to each ring. The simulations fully reproduce this behavior with the assumption of an isotropic distribution in the rest frame. Experimental deviations from this assumption may impact the analysis, but a preliminary investigation found no effect on the result using various anisotropic distributions. A more detailed study may be prudent.

Finally, several experimental advances on the horizon will play an important role in improving lifetime measurements with the Köln/NSCL plunger. As discussed within Subsect. 2.3.2, preserving the ability to resolve the photopeaks from decays upstream and downstream of the plunger degrader is essential for a successful RDM lifetime measurement. The present resolution is limited by uncertainties in the Doppler reconstruction of gamma-ray energies in the laboratory frame from the spread of both the detection angles ($\Delta\theta$) and reaction residue velocities ($\Delta\beta$). As illustrated in Fig. B.1, the most dominant contribution to the energy resolution comes from this angular uncertainty. The advent of a new generation of gamma-ray detector arrays such as AGATA [121], GRETA [122], and the more immediate GRETINA [123] will usher in a new paradigm for gamma-ray spectroscopy where gamma-ray tracking [124] will provide an accurate determination of the first interaction point. The measured position resolution of GRETINA has been demonstrated to be roughly 2 mm [125] whereas a single SeGA segment is 1 cm wide. This improved position resolution translates directly to improved energy resolution of Doppler reconstructed energy spectra.

It should be noted that sub-segment resolution has already been demonstrated in principle for SeGA instrumented with the Digital Data Acquisition System (DDAS) [88]; Fig. 5.3 illustrates the effect. The synchronous capture of waveforms in all 32 segments of a SeGA detector provides information about the gamma-ray interaction position on an event-by-event basis. The caption of Fig. 5.3 provides more details. The decomposition of these signals to provide precise position information is non-trivial and beyond the scope of this work. Nonetheless, the figure illustrates that the improvement of SeGA angular resolution is possible with DDAS and may play an important role in future studies where GRETINA (or GRETA) and the associated digital electronics are unavailable.

Currently, the plunger degrader thickness is chosen to provide adequate separation between the two photopeaks. Thus the improvement in gamma-ray energy resolution afforded by gamma-ray tracking and waveform capturing will permit the use of thinner degraders. The most immediate consequence of this improvement is the ability to probe shorter lifetimes—thinner degraders equate to shorter transit times and thus more decays downstream of the degrader. A secondary benefit of thinner degrader foils will be the reduction of contaminant gamma-rays from the de-excitation of states produced by reactions on the degrader.

Aside from thinner degraders, another interesting prospect for future plunger lifetime measurements at NSCL involves the use of multiple degraders. The so-called "double plunger" is currently in the design phase [126] and will provide multiple configurations for different lifetime measurement requirements. In the simplest approach, a second degrader is added to provide a third photopeak corresponding to decays downstream of the second and final degrader. Thus a single plunger setting can provide two different distances; in principle data can be taken at more distances, though the photopeak intensity reduction from splitting two decay regions into three requires consideration. Another configuration utilizing one degrader

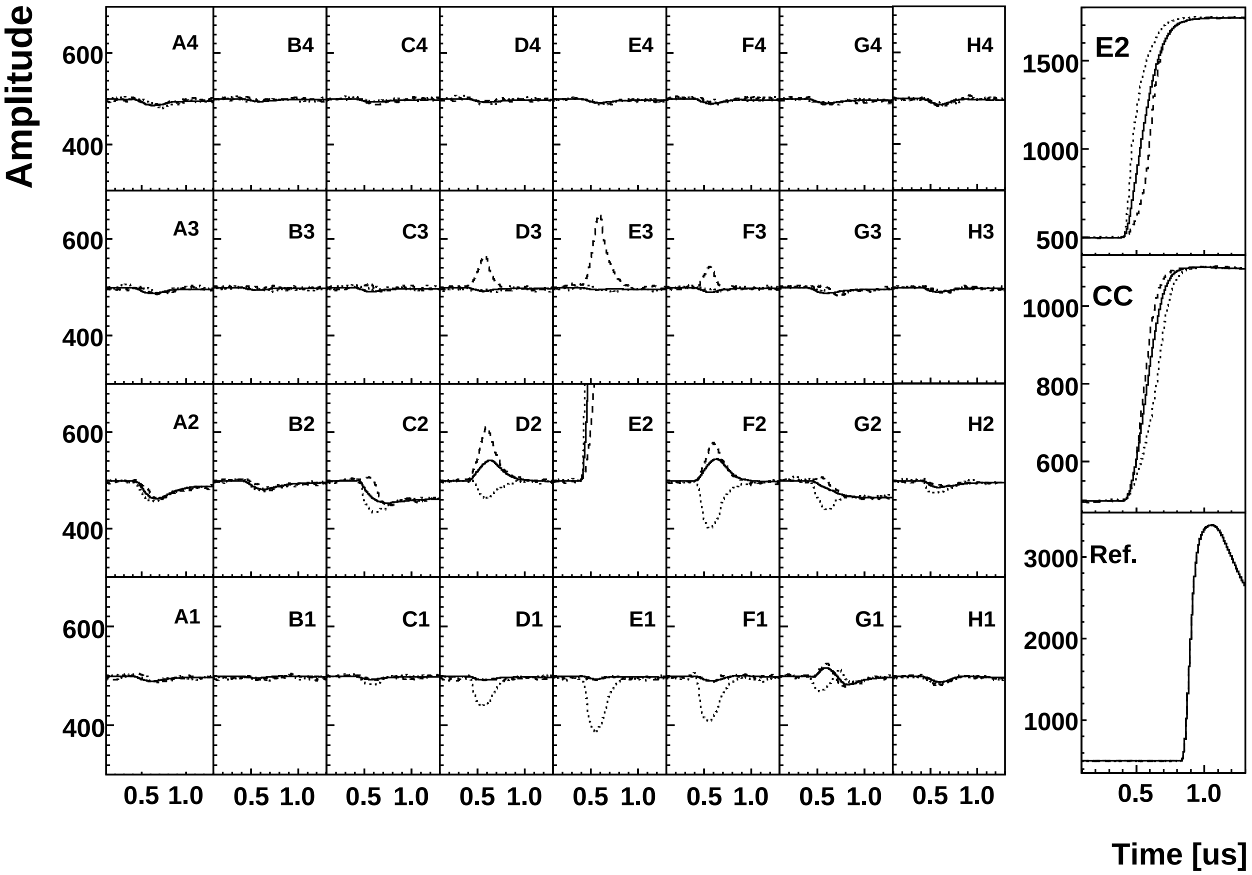

Figure 5.3: Digital waveforms for several events in all 32 channels of a single SeGA detector corresponding to the full absorption of a 1332 keV gamma-ray from ^{60}Co in a single segment (E2) in coincidence with a 1173 keV gamma-ray detected in a fast CsF scintillator. This scintillator was used as a timing reference ("Ref.", bottom right). The solid black signals are the average of many such signals and should be contrasted to two individual events (dashed and dotted lines). The observable rise time differences are taken as evidence of sub-segment position resolution. Figure from Ref. [88]

close to the production target ($\sim$ 1 mm) and another much further away ($\sim$ 1 cm) can simultaneously collect two sets of data in very different lifetime regimes. Note that the contaminant events from production of excited states on the multiple degraders will have to be characterized for both implementations.

Table 5.3: ^{19}Mg two-proton decay lifetime (picoseconds) as a function of R_p.

	^{17}Ne Production Mechanism Ratio									
	0.05	0.15	0.25	0.35	0.45	0.55	0.65	0.75	0.85	0.95
τ	0.35	0.39	0.46	0.49	0.60	0.76	0.96	1.35	2.44	7.26
$\Delta\tau$	0.09	0.09	0.12	0.14	0.15	0.18	0.22	0.31	0.54	–

5.2 ^{19}Mg Commentary

The ^{19}Mg mean two-proton decay lifetime study was presented in Ch. 4. The extracted lifetime depended strongly upon the ^{17}Ne production mechanism ratio R_p. This ratio was not well constrained by either the data or from previous studies. There was also a dependence, albeit a much weaker one, upon the target-detector reaction yield ratio R_σ. Hence the best-fit lifetime depended upon the combination of R_p and R_σ; the results were presented in Tab. 4.2.

As discussed within Subsect. 4.3.1, R_σ was well constrained between 3.03 and 3.43. The best-fit lifetime from the central value $R_\sigma = 3.23$ has been taken as the unique lifetime result at each R_p. The best-fit lifetimes corresponding to the upper and lower R_σ limits were taken as the main source of systematic uncertainty. Accurate simulated DSSD ΔE line-shapes required excellent agreement between the simulated and experimental d_{ta} spectra (as illustrated in Fig. 4.5). The contribution of small, but tolerable, variations in the simulated reaction residue momentum distribution to the systematic error was explored and found to contribute half as much as the uncertainties in R_σ. All other sources of systematic error were found to be negligible, including variations in the two-proton decay Q-value. The root sum of squares of these two systematic errors was adopted for the final results, which are presented in Tab. 5.3. There, the overall uncertainty is given as $\Delta\tau = \Delta\tau_{stat} + \Delta\tau_{syst}$.

It is prudent to compared these results with those of the ^{19}Mg lifetime measurement reported in Ref. [38]. This exercise is presented in the following subsection. There, the stark difference between the measurements shall be discussed. The present results indicate a lifetime one order of magnitude smaller than the literature value of $\tau = 5.8 \pm 2.2$ ps. In addition, the demonstrated sensitivity to picosecond lifetimes in this work validates the Köln/NSCL particle plunger technique for lifetime measurements of charged-particle emitters.

5.2.1 Comparison to Previous Work

The method used for the first measurement of the two-proton emitter ^{19}Mg is presented in detail in Ref. [38, 127, 128]. There, the energy and angles of the three-body decay remnants of ^{19}Mg were measured independently. The decay vertex was reconstructed from the deduced trajectories' point of closest approach. Plotting the observed decay vertices against the production target profile yielded a distribution from which the lifetime was determined.

The authors noted the indistinguishability between the vertex distribution from the non-resonant breakup $^{20}\mathrm{Mg} \rightarrow \mathrm{p} + \mathrm{p} + \mathrm{n} + {}^{17}\mathrm{Ne}$ and the prompt proton decay of ^{19}Mg excited states with lifetimes well below the experimental sensitivity. By comparing the observed ^{17}Ne-proton angular correlations to simulations, the contribution of these prompt events to the ground state $2p$ decay data was determined to be 25%. The quoted lifetime result was derived using this percentage. Factoring in the uncertainties of the shape of these background contributions yielded an upper limit contribution of 65%. A lifetime was given for this case and also the 0% lower limit case where no background contribution was considered.

Note that these prompt contribution percentages to the ^{17}Ne yield are entirely equivalent to the ^{17}Ne production mechanism ratio R_p introduced for the analysis presented in Eq. 4.1 of Ch. 4. Thus, their contribution to the decay vertex distribution of the delayed two-proton emission from the ^{19}Mg ground state is synonymous with the impact of the simulated R_p on the ΔE lineshape simulations. For this reason, the range of reasonable values for the ^{17}Ne production mechanism ratio was set to $0.15 \leq R_p \leq 0.85$ to fully encompass the findings reported in [38].

Table 5.4: Comparison of ^{19}Mg lifetime to the previous study [38] as a function of R_p. For ease of comparison, the literature value at $R_p = 0.00$ is approximated by $R_p = 0.05$. See text for details.

	^{17}Ne Production Mechanism Ratio		
	0.05	0.25	0.65
Current Work	0.35 ± 0.09	0.46 ± 0.12	0.96 ± 0.22
Ref. [38]	4.5 ± 1.5	5.8 ± 2.2	9^{+3}_{-6}

This fortuitous equivalence allows the two measurements to be compared on equal footing. Table 5.4 presents the lifetimes for three R_p values. There, the lifetime derived from the 0% prompt ^{17}Ne contribution scenario is used as an approximate value for comparison with the $R_p = 0.05$ result from the analysis of Ch. 4. The table demonstrates the results from the two measurements differ by one order of magnitude.

Figures 5.4 and 5.5 provide a direct contrast between the two measurements at $R_p = 0.25$. In both figures, the data for 0 mm ^{17}Ne particle-gated energy losses are plotted with statistical uncertainties against simulated lineshapes. The former is generated with the best-fit lifetime $\tau = 0.46$ ps from Tab. 5.4 and the latter with the literature reported lifetime $\tau = 5.8$ ps. Both simulations incorporated the exact same parameters to model the incoming ^{20}Mg secondary beam, knockout reaction kinematics, detector response, and background functions. Thus the only difference between the two, save for an overall scaling factor to normalize the simulated ^{17}Ne peak height to the data, is the input lifetimes. The discrepancy between the two results is clear; the presented data does not support such a long lifetime.

The demonstrated picosecond lifetime sensitivity to the ground state two-proton emission of ^{19}Mg indicates that lifetime measurements of exotic proton emitters with the Köln/NSCL particle plunger technique merit further consideration. This proof of concept measurement opens the door for future studies of nuclei beyond the proton dripline. The region surrounding the $N = Z$ *rp*-process waiting-point nuclei is of immediate interest, as the introduction given in Subsect. 1.4.2 indicated. In particular, the bridging of ^{68}Se by sequential one-proton

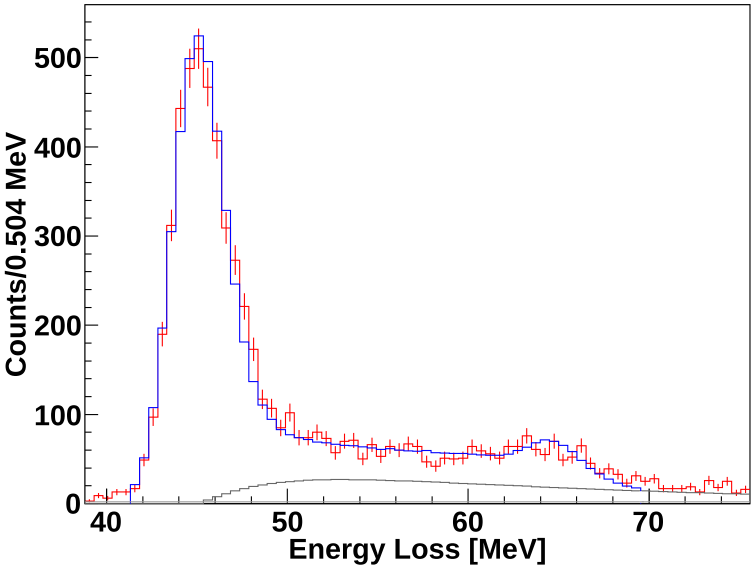

Figure 5.4: ^{17}Ne particle-gated silicon energy loss spectra at 0 mm with statistical uncertainties (red). The simulated lineshape (blue) was generated from the best-fit lifetime $\tau = 0.46$ ps from the lifetime scans with $R_p = 0.25$ and $R_\sigma = 3.23$.

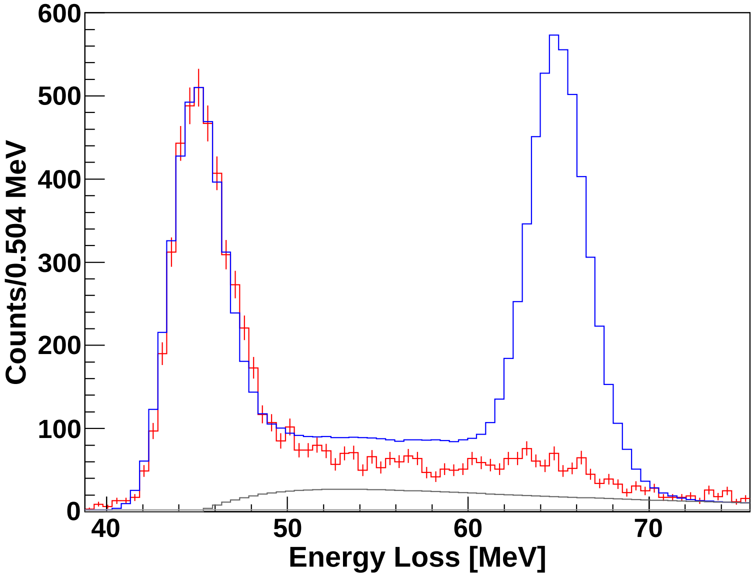

Figure 5.5: Same as in Fig. 5.4, but with the simulated lineshape generated with the lifetime $\tau = 5.8$ ps from Ref. [38].

captures as depicted in Fig. 1.3 depends sensitively upon the $1p$ separation energy of the proton unbound nucleus ^{69}Br via Eq. 1.32. A recent experiment determined the separation energy to be $S_p = -785$ keV and therefore ^{69}Br is sufficiently unbound such that the proton capture mechanism cannot bridge the ^{68}Se waiting point [58]. However, the analysis suffered from the lack of a measured one-proton decay lifetime for ^{69}Br. An upper limit of 24 ns has been set [57]; a more rigorous lifetime measurement for this nucleus (and others like it) can aid in experimental analysis and provide a vital check for accurate mass models.

5.2.2 Comments on Future Prospects

The successful proof of concept measurement was not without experimental difficulties that must be improved upon. Some suggestions, ranging from the very practical to the more complicated, are proffered below and may prove useful for future applications of the technique. This discussion is framed within the scope of the current work so that the terminology and context is familiar.

The significant contribution of reactions on the silicon DSSD to the ΔE lineshape was discussed in Subsect. 4.2.3. The simplest remedy to remove these contributions is gathering ^{17}Ne particle-gated lineshapes from detector-only data. This would provide a quantitative picture of the characteristic energy loss in the detector from the direct dissociation $^{20}\mathrm{Mg} \rightarrow \mathrm{p} + \mathrm{p} + \mathrm{n} + {}^{17}\mathrm{Ne}$ and the one neutron knockout and subsequent two-proton decay $^{19}\mathrm{Mg} \rightarrow \mathrm{p}+\mathrm{p}+{}^{17}\mathrm{Ne}$ processes. The detector contribution could then be subtracted from the data, but care must be taken to ensure the data can be properly normalized to account for fluctuating beam currents. The ΔE lineshape shift introduced by the difference in ^{20}Mg secondary beam energies with and without the target installed must also be accounted for.

The use of a thinner silicon DSSD would be advantageous, as it would mitigate the effect of contaminant reactions on the silicon and subsequently improve the ^{19}Mg peak-to-plateau intensity ratio. Furthermore, for short-lived nuclei a thinner detector would permit a greater

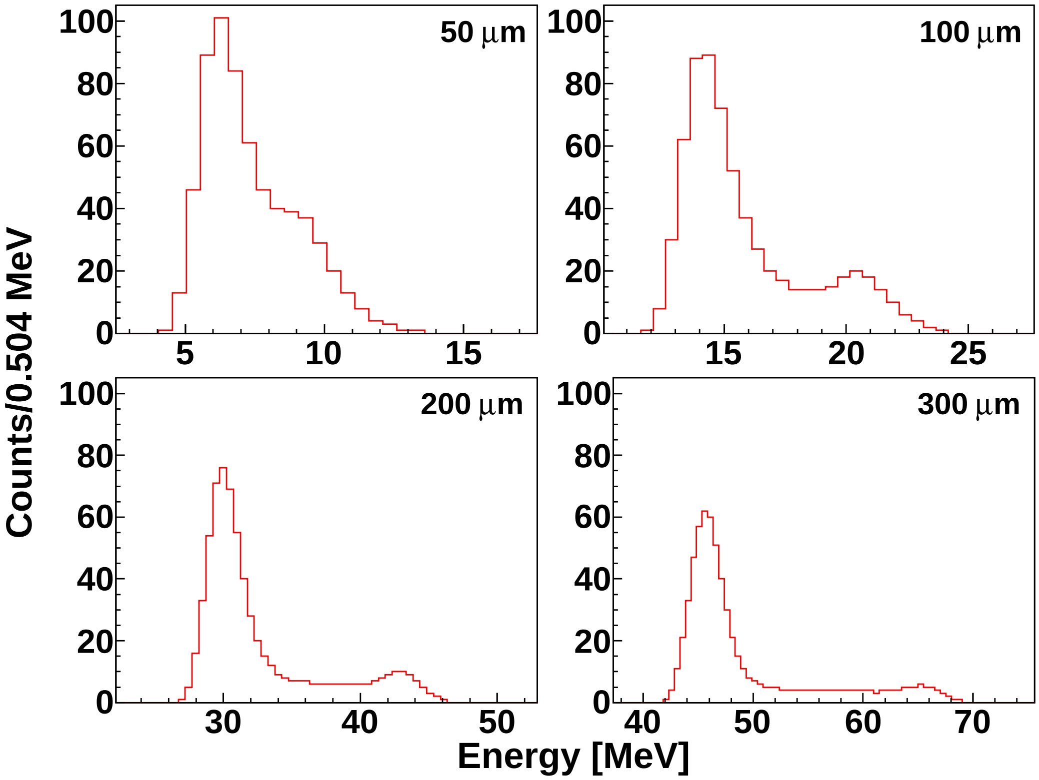

Figure 5.6: Simulated silicon detector energy loss profiles for four different detector thickness. The simulation parameters were taken from the experimental analysis with $R_\sigma = 3.23$, $R_p = 0.55$, and the corresponding best-fit lifetime $\tau = 0.76$ ps.

fraction of $1n$ knockout residues to fully traverse the detector before decaying. This would also improve the ^{19}Mg peak-to-plateau ratio and may open the possibility of investigating the ^{17}Ne/^{19}Mg energy loss peak intensity ratios at various target-detector distances. Figure 5.6 illustrates the energy loss lineshapes from four different detector thicknesses. Note the more prominent ^{19}Mg peak for detectors with thicknesses between 100 and 200 µm compared to the 300 µm detector used in the present work. Too thin of a detector is also undesirable; with smaller energy deposits the resolution between the ^{17}Ne and ^{19}Mg peaks is lost. The plots suggest an optimal detector thickness of approximately 150 µm.

Constraining the uncertainty in the ^{17}Ne production mechanism ratio is perhaps the most crucial task for future particle plunger studies. As discussed in Ch. 4 and Sect. 5.2, the inability to distinguish between ^{17}Ne reaction residues from the two-proton decay of ^{19}Mg or the breakup of ^{20}Mg in the target prevents the extraction of a single two-proton decay lifetime. Care should be taken during experimental planning to determine the optimal secondary beam reaction mechanism that minimizes such a contaminant production mechanism without compromising the production of the nucleus of interest. Along the proton dripline, proton knockout reactions may not be a viable alternative to the one-neutron knockout utilized in the present experiment; $2n$ and $1n1p$ knockouts should also be investigated. However, a cursory investigation with LISE++ using both Abration Ablation [107,108] and EPAX 2.15 [106] parameterizations reveals these two to be inferior to $1n$ knockout when both production rate and ^{17}Ne contaminant suppression are considered.

For proton decay studies along the dripline, it is likely that cross section measurements or reliable calculations will be lacking beforehand. Therefore the greatest improvement in constraining R_p will come from modifications to the particle plunger technique such that either the ratio can be determined alongside the ground state proton emission lifetime or the contaminant signals can be rejected. A possible implementation of the first modification type would be to utilize the particle plunger with a separate charged-particle array such that the angle between the ^{17}Ne decay residue and protons can be measured [126]. The High Resolution Array [129] at NSCL would be one choice to measure the protons from the decay, however the large scattering chamber would have to be modified to mount the particle plunger. The effort may prove worthwhile; measuring ^{17}Ne-p angular correlations can help to distinguish between ground state two-proton emission and prompt production of ^{17}Ne as demonstrated in [38].

A less elegant modification would entail the addition of a thin silicon veto detector installed immediately downstream of the secondary target. This could generate a veto, or anti-coincidence, flag in the analysis for events where ^{17}Ne emerged from the target. These rejected events would originate from the nonresonant breakup of ^{20}Mg, the prompt proton emission from excited state decays of ^{19}Mg, and ground state two-proton decays occurring within the target. The addition of a thin veto detector would further suppress the experimental sensitivity to very short lifetimes and also have to be accounted for in the simulations, although contaminant reactions would be minimal in such a thin detector. However, the loss of resolution between the ^{17}Ne peak and other ΔE features evident in thin detectors (see Fig. 5.6) would have to be addressed. The technical details are less complicated than the above modification; if the resolution issues can be overcome, the contribution of prompt ^{17}Ne contaminants would be eliminated.

Finally, the analysis of future particle-plunger measurements will likely incorporate similar Geant4 simulations. Including the DSSD dead layers into the simulation software should be a simple improvement to implement. The dead layer on both sides is comprised of the aluminum electrical contacts, plus the p^{+}-type junction contact on one side and the n^{+}-type ohmic contact on the other. The current simulation implementation neglected these layers, as it was estimated to be less than 1 μm on each side [130] and thus roughly only 0.5% of the total detector thickness. If thinner detectors are used, this contribution will increase. Simply decreasing the simulated detector width with respect to the manufacturer's specifications will not account for the dead layers; they represent regions where the beam can deposit energy or scatter. These experimental effects should be incorporated to improve the accuracy of simulated ΔE lineshapes.

Chapter 6

Conclusions

Lifetime measurements with the Köln/NSCL plunger are sensitive probes of the behavior and structure of exotic nuclei at the extremes of isospin. Picosecond-ordered decay processes are studied in a model independent fashion. The lifetime is derived from changes in gamma-ray energy spectra or charged-particle energy loss lineshapes elicited by micron-precision adjustments of the target-degrader (or detector) distance. The versatility of this Recoil Distance Method technique with intermediate energy radioactive beams and inverse kinematics has been demonstrated in this work.

The lifetime of the electromagnetic quadrupole $2_1^+ \to 0_{gs}^+$ transition in ^{18}C was measured. The state was populated by the one-proton knockout reaction of a ^{19}N secondary beam on the beryllium plunger target. The Doppler-shift corrected gamma-ray energy spectrum exhibited two photopeaks corresponding to de-excitations upstream or downstream of the tantalum plunger degrader. The lifetime was determined by fitting these lineshapes at five target-degrader distances with simulated spectra. From the lifetime, the reduced quadrupole transition strength $B(E2)$ was extracted, which provides a straightforward means to quantify the degree of collectivity in ^{18}C. The results agree well with a previous measurement [29] and the fractional uncertainty has been reduced by a factor of two. The excitation energy and $B(E2)$ calculated with the *ab initio* no-core shell model [15] exhibit excellent agreement with the data, providing an important test for *ab initio* calculations of heavier and more exotic nuclei utilizing the importance truncation [16] approach. In addition, a weak transition feeding the 2_1^+ state was observed and a conservative lifetime upper limit was measured. This represents the first quantitative lifetime information for a state above the first 2^+ for neutron-rich, even-even carbon isotopes.

A modified Köln/NSCL plunger was constructed with a thin silicon detector in place of the degrader. The lifetime of the exotic two-proton emitter ^{19}Mg was measured as a proof of concept of this device for lifetime measurements of charged-particle emitters beyond the proton dripline. States were populated by the one-neutron knockout reaction of a ^{20}Mg secondary beam on the carbon plunger target. A very short lifetime for the ground state two-proton radioactivity was deduced by fitting the energy loss signatures of ^{19}Mg and the two-proton decay residue ^{17}Ne in the silicon detector with simulated lineshapes. The contribution of contaminant ^{17}Ne from both the immediate breakup of ^{20}Mg and the prompt sequential one-proton emissions via an intermediary unbound ^{18}Na ground state could not be quantified. Thus the lifetime was determined as a function of this prompt ^{17}Ne contribution.

Regardless of the extent of this contaminant, the results indicate a lifetime one order of magnitude smaller than that of a previous measurement [38]. This work has demonstrated the potential of this new experimental technique, especially along the proton dripline where lifetime information provides important constraints on mass models and proton-capture rates invaluable for the accurate characterization of nucleosynthesis pathways.

APPENDICES

Appendix A

Electromagnetic Selection Rules

A.1 Parity Selection Rules

Knowledge of the character and multipolarity of an electromagnetic transition linking two nuclear states is paramount to interpreting the experimental results in terms of nuclear properties. For instance, without knowing the transition observed in the ^{18}C experiment was $E2$ in nature, the lifetime result cannot be interpreted as a gauge of nuclear quadrupole collectivity. ^{18}C has an even number of protons and neutrons. A general property of all such even-even nuclei is that the ground state is always 0^+ due to the pairing of nucleons in a particular l-orbital into spin up-spin down pairs. Furthermore, the first excited state is in all but a very few instances 2^+, as noted in Ref. [131]. Thus from systematics, the spins and parities J^π of the initial excited and final ground state in ^{18}C are known, and from this the character and multipolarity of the gamma ray transition can be deduced.

The conservation of parity for electromagnetic operators follows from the parity rules implicit in Eq. 1.4 and 1.5. The parity of a spherical harmonic $Y_{\lambda\mu}$ is $(-1)^\lambda$ and that of r^λ is $+1$. Therefore the total parity of an electric λ-pole is $+1 \cdot (-1)^\lambda = (-1)^\lambda$. For the magnetic λ-pole, $\mathbf{l}$ and $\mathbf{s}$ are axial vectors and thus have a parity of $+1$. The total parity is thus determined by the gradient vector (with a parity of -1) acting on $r^{\lambda}Y_{\lambda\mu}$ (with a parity of $(-1)^{\lambda}$) and is $-1 \cdot (-1)^{\lambda} = (-1)^{\lambda-1}$. The parity conservation selection rule can thus be stated as

$$\pi_i \pi_f = \begin{cases} (-1)^{\lambda-1} & \text{for M}\lambda \\ (-1)^{\lambda} & \text{for E}\lambda. \end{cases} \tag{A.1}$$

A.2 Angular Momentum Selection Rules

The angular momentum selection rules follow the triangle condition, where the possible multipolarities λ of the photon can be determined from the spins of the initial and final states according to

$$\left|J_i - J_f\right| \leq \lambda \leq J_i + J_f. \tag{A.2}$$

From Eq. A.2 it is apparent that the $2_1^+ \rightarrow 0_{gs}^+$ transition in ^{18}C proceeds with the emission of a $\lambda = 2$ photon that carries away two units of angular momentum. Furthermore, since $\pi_i \pi_f = +1$ and λ was determined to be even, the transition must be an electric quadrupole ($E2$) according to Eq. A.1.

As a brief aside, consider the case where the initial and final spins are such that several electromagnetic λ-poles could contribute. For example, the $\frac{3}{2}^+ \rightarrow \frac{1}{2}^+$ transition allows λ values of 1 and 2 while the change in parity is $\pi_i \pi_f = +1$. Thus the emitted radiation would be an admixture of $M1$ and $E2$ components; to determine which component dominates in order to relate the measured lifetime to the appropriate matrix element ($B(E2)$ or $B(M1)$), Weisskopf single-particle transition probability estimates ($B_W(E2)$ or $B_W(M1)$, for example) can be computed. The derivation of these estimates proceeds from the solution of the reduced matrix element of Eq. 1.8 in Ch. 1 utilizing some simplifying assumptions and is beyond the scope of this work. The results for electric and magnetic transitions are

$$B_W(E\lambda) = \frac{1.2^{2\lambda}}{4\pi}\left(\frac{3}{3+\lambda}\right)^2 A^{2\lambda/3}e^2fm^{2\lambda} \tag{A.3}$$

$$B_W(M\lambda) = \frac{10}{\pi}1.2^{(2\lambda-2)}\left(\frac{3}{3+\lambda}\right)^2 A^{(2\lambda-2)/3}(\mu_N/c)^2fm^{2\lambda-2}. \tag{A.4}$$

These equations can then be substituted into Eq. 1.7 and the transition probabilities can be compared. For instance, assuming $A = 100$ and $E = 1$ MeV, the transition probability ratio would be $T(M1) : T(E2) \approx 10^3$ and therefore the $M1$ contribution would be expected to dominate.

Calculations such as these using Weisskopf estimates provide a good starting point, but are too simple as they only take single-particle excitations into account. For collective nuclear states, the motion of many nucleons must be taken into account to describe the transition. In these cases, the $B_W(E2)$ can underestimate the experimentally determined $B(E2)$ by an order of magnitude or more.

Appendix B

Relativistic Considerations

B.1 Relativistic Kinematics Formulation

As noted in Ch. 3 and 4, the reaction residues emerged from the plunger target at the S800 target position with velocities $\beta = v/c \approx 0.4$. It is therefore necessary to account for time dilation and the relativistic Doppler effect in the analysis. Here, the equations required for the proper relativistic treatment are derived.

Consider the beam traveling along the z-axis with velocity $v = \beta c$. Let the position and time coordinates in the laboratory frame be represented by unprimed coordinates (ct, x, y, z) and those in the rest frame of the beam by primed coordinates (ct', x', y', z'). The four Lorentz transformation equations that relate the coordinates in the laboratory frame to those in the rest frame follow.

$$\begin{aligned} ct &= \gamma\left(ct' + \beta z'\right) \\ x &= x' \\ y &= y' \\ z &= \gamma\left(z' + \beta ct'\right) \end{aligned} \tag{B.1}$$

Here the relativistic factor γ is defined by

$$\gamma = \frac{1}{\sqrt{1-\beta^2}}. \tag{B.2}$$

It is convenient to utilize the concept of 4-vectors, $x_\alpha = (x_0, x_1, x_2, x_3)$.[1] The inner product is a Lorentz invariant 4-scalar; therefore it is the same in all inertial reference frames, and is given by

$$|x|^2 = x_\alpha x^\alpha = (x_0)^2 - (x_1)^2 - (x_2)^2 - (x_3)^2 = invariant. \tag{B.3}$$

Here, x_0 is the timelike component while $x_{1,2,3}$ are the spacelike components. For uniform motion along the z-axis, the components of the 4-vector x_α undergo the Lorentz transformation from one inertial frame to another in a similar manner as those in Eq. B.1.

$$\begin{aligned} x_0 &= \gamma\left(x_0' + \beta x_3'\right) \\ x_1 &= x_1' \\ x_2 &= x_2' \\ x_3 &= \gamma\left(x_3' + \beta x_0'\right) \end{aligned} \tag{B.4}$$

We can use the properties defined in Eq. B.3 and B.4 along with the universality of the speed of light in all reference frames to derive several useful relationships.

Consider the position of a beam particle in four dimensional Minkowski space,

$$r_\alpha = (ct, \vec{r}) = (ct, x, y, z). \tag{B.5}$$

---

[1] In the literature, there is a notational distinction between x_α and x^α as being covariant and contravariant 4-vectors, respectively. In this brief mathematical formulation all 4-vectors are contravariant, however the designation x_α is used for ease of reading.

Suppose this particle decays after an elapsed time in the laboratory frame $t_{12} = t_2 - t_1$ and a change in laboratory position of $\vec{r}_{12} = \sqrt{(x_2 - x_1)^2 + (y_2 - y_1)^2 + (z_2 - z_1)^2} = \sqrt{x_{12}^2 + y_{12}^2 + z_{12}^2}$. In the beam rest frame a different time interval elapses, t'_{12}, but there is no change in position such that $\vec{r'}_{12} = 0$. Since $r_\alpha r^\alpha$ is an invariant quantity, the relationship between the decay event coordinates in the laboratory and rest frames from Eq. B.3 is

$$c^2 t'^2_{12} = c^2 t_{12}^2 - x_{12}^2 - y_{12}^2 - z_{12}^2. \tag{B.6}$$

Dividing both sides of the equation by c^2 and taking the square root yields

$$t'_{12} = \sqrt{t_{12}^2 - \frac{1}{c^2}(x_{12}^2 + y_{12}^2 + z_{12}^2)} = t_{12}\sqrt{1 - \frac{1}{c^2}\left(\frac{x_{12}^2 + y_{12}^2 + z_{12}^2}{t_{12}^2}\right)}. \tag{B.7}$$

But the second term under the square root is simply the speed squared of the beam particle as measured in the laboratory frame and therefore with the help of Eq. B.2, the final result is

$$t'_{12} = t_{12}\sqrt{1 - \frac{v^2}{c^2}} = \frac{t_{12}}{\gamma}. \tag{B.8}$$

Thus the lifetime of a particle measured in the laboratory frame, $\tau_{lab} = t_{12}$, is related to the lifetime of the particle in the rest reference frame, $\tau_{rest} = t'_{12}$, by

$$\tau_{lab} = \gamma \tau_{rest}. \tag{B.9}$$

The Lorentz transformations of a generalized 4-vector in Eq. B.4 prove useful for determining the relationships between the gamma-ray energy and angle of emission as measured in the laboratory reference frame and those in the rest frame. Consider the 4-vector

$$k_\alpha = \left(\frac{\omega}{c}, \vec{k}\right) = \left(\frac{\omega}{c}, k_x, k_y, k_z\right) \tag{B.10}$$

where for a photon, the wave vector, $\vec{k}$, and frequency, $\omega = 2\pi\nu$, are related by

$$\omega = c\left|\vec{k}\right|. \tag{B.11}$$

The invariant inner product of the wave 4-vector is

$$k_\alpha k^\alpha = \frac{\omega^2}{c^2} - \vec{k}\cdot\vec{k} = \frac{\omega^2}{c^2} - k^2 = 0. \tag{B.12}$$

For a beam propagating along the z-axis, the k_z component of the wave vector and frequency ω in the laboratory frame are related to k'_z and ω' in the rest frame by Eq. B.4.

$$k_z = \gamma\left(k'_z + \beta\frac{\omega'}{c}\right) \tag{B.13}$$

$$\frac{\omega}{c} = \gamma\left(\frac{\omega'}{c} + \beta k'_z\right) \tag{B.14}$$

In addition, the k_z component of the wave vector in the laboratory frame is given by

$$k_z = \left|\vec{k}\right|\cos\theta = \frac{\omega}{c}\cos\theta, \tag{B.15}$$

where θ is the angle of photon propagation with respect to the z-axis. A similar expression can be written in the rest frame for the wave vector $\vec{k'}$ and angle of propagation θ'. With Eq. B.15 and its rest frame analog in hand, Eq. B.13 and B.14 can be rewritten.

$$k_z = \frac{\omega}{c}\cos\theta = \gamma\left(\left|\vec{k'}\right|\cos\theta' + \beta\frac{\omega'}{c}\right) = \gamma\frac{\omega'}{c}\left(\cos\theta' + \beta\right) \tag{B.16}$$

$$\frac{\omega}{c} = \gamma\left(\frac{\omega'}{c} + \beta\left|\vec{k'}\right|\cos\theta'\right) = \gamma\frac{\omega'}{c}(1 + \beta\cos\theta') \tag{B.17}$$

Rearranging the previous two equations yields

$$\frac{\omega}{\omega'} = \gamma\frac{\left(\cos\theta' + \beta\right)}{\cos\theta} \tag{B.18}$$

$$\frac{\omega}{\omega'} = \gamma(1 + \beta\cos\theta') \tag{B.19}$$

which when combined produce the relationship between the angle in the rest and laboratory reference frames,

$$\cos\theta' = \frac{\cos\theta - \beta}{1 - \beta\cos\theta}. \tag{B.20}$$

From this expression, the Lorentz boost of the solid angle from the rest frame to laboratory reference frame can be extracted. For uniform motion along the z-axis, the azimuthal angle is not boosted. Therefore from the expression for the solid angle

$$d\Omega = \sin\theta d\theta d\phi = -d(\cos\theta)d\phi, \tag{B.21}$$

the derivative with respect to $\cos\theta$ of Eq. B.20 is taken to yield the result

$$\frac{d\Omega'}{d\Omega} = \frac{d(\cos\theta')}{d(\cos\theta)} = \frac{1 - \beta^2}{(1 - \beta\cos\theta)^2}. \tag{B.22}$$

B.2 Doppler Reconstruction

The Doppler shift of gamma-ray energies proceeds from Eq. B.19. Replacing ω with the familiar relationship $\omega = E/\hbar$ and substituting Eq. B.20 for $\cos\theta'$ yields

$$\frac{E}{E'} = \gamma\left(1 + \beta\frac{\cos\theta - \beta}{1 - \beta\cos\theta}\right) = \frac{\sqrt{1 - \beta^2}}{1 - \beta\cos\theta} \tag{B.23}$$

where β is the beam velocity and θ is the laboratory angle of gamma-ray emission with respect to the beam velocity vector.

As an example from the ^{18}C analysis, consider a photon with energy $E' = 1585$ keV in the beam rest frame emitted from a reaction residue with velocity $\beta = 0.3565$ and at a laboratory angle of 30°. This photon can be detected in the forward ring of SeGA with energy

$$E = E' \frac{\sqrt{1-\beta^2}}{1-\beta\cos\theta} = (1585 \text{ keV}) \frac{\sqrt{1-0.3565^2}}{1-0.3565\cdot\cos 30^\circ} = 2142 \text{ keV}. \tag{B.24}$$

Similarly, if the photon is emitted at a laboratory angle of 140°, it can be detected in the backward ring with energy

$$E = E' \frac{\sqrt{1-\beta^2}}{1-\beta\cos\theta} = (1585 \text{ keV}) \frac{\sqrt{1-0.3565^2}}{1-0.3565\cdot\cos 140^\circ} = 1163 \text{ keV}. \tag{B.25}$$

Thus relativistic effects shift the measured gamma-ray energy by more than 25%.

The Doppler reconstruction of gamma rays detected at their shifted energies in the laboratory frame proceeds from the inverse of Eq. B.23,

$$E' = E \frac{1-\beta\cos\theta}{\sqrt{1-\beta^2}}. \tag{B.26}$$

Here, the unmeasured angle of gamma-ray emission from Eq. B.23 has been replaced with the laboratory angle θ of the SeGA segment in which the first gamma-ray interaction occurred (see Subsect. 2.3.1 for more details). This introduces an uncertainty in the angle for Doppler reconstruction, $\Delta\theta$, related to the finite opening angle of the segment. In addition, the incoming momentum spread of the secondary beam, the energy straggling in the plunger foils, and the one-proton knockout reaction all introduce a spread of reaction residue velocities, $\Delta\beta$, on an event-by-event basis. Since most decays occur after the reaction residues emerge from the plunger target, there are two narrow groupings of beam velocities at which the nuclei decay—corresponding to decays in vacuum either upstream or downstream from the plunger degrader—with centroid values of β_{fast} and β_{slow}. The values were obtained by first estimating the velocity from the magnetic rigidity of the S800 spectrometer in LISE++ (and for β_{fast}, then back tracking through the degrader) and then fine tuning the estimates to properly align the fast or slow components of the 1585 keV transition in the forward and backward rings of SeGA. Both $\Delta\beta$ and $\Delta\theta$ increase the photopeak full-width at half-maximum (FWHM) in the Doppler corrected gamma-ray energy spectrum.

The contribution from the uncertainties in the velocity and detection angles to the overall energy resolution can be quantified. An expression for the energy resolution of the Doppler reconstructed spectrum as a function of $\Delta\beta$, $\Delta\theta$, and ΔE is given by

$$\Delta E'^2 = \left(\frac{\partial E'}{\partial E}\right)^2 \Delta E^2 + \left(\frac{\partial E'}{\partial \beta}\right)^2 \Delta\beta^2 + \left(\frac{\partial E'}{\partial \theta}\right)^2 \Delta\theta^2. \tag{B.27}$$

The first term can be safely neglected as the contribution from the intrinsic resolution of germanium detectors (approximately 0.2% for a 1 MeV photon) is very small. Taking the appropriate partial derivatives of Eq. B.26 and rearranging terms yields

$$\left(\frac{\Delta E'}{E'}\right)^2 = \left(\frac{\beta - \cos\theta}{(1-\beta^2)(1-\beta\cos\theta)}\right)^2 \Delta\beta^2 + \left(\frac{\beta\sin\theta}{1-\beta\cos\theta}\right)^2 \Delta\theta^2. \tag{B.28}$$

Panel 1 of Fig. B.1 plots the resulting total gamma-ray energy resolution (blue) as well as the individual $\Delta\beta$ (black) and $\Delta\theta$ (red) components as a function of laboratory angle. An input beam velocity of $\beta = 0.361$ was taken from the plunger target-only ^{18}C experimental data. The experimental uncertainty in the velocity was estimated by the spread of β values that align the 1585 keV transition photopeak at each plunger distance to be 0.15%. To err on the side of caution, $\Delta\beta$ was set to twice this. $\Delta\theta$ was fixed to 2.46°; this corresponds to the angle subtended by a single backward ring segment at a distance of approximately 23.3 cm

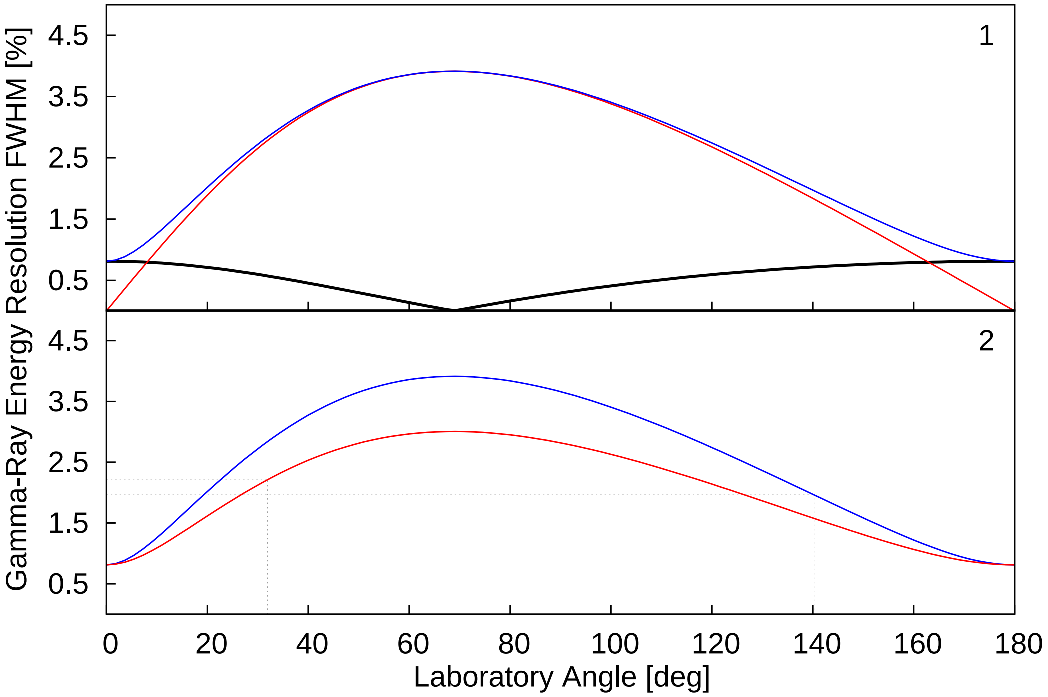

Figure B.1: Contributions to the total energy resolution FWHM in the Doppler reconstructed gamma-ray spectra as a function of laboratory angle. The negligible contribution from the intrinsic gamma-ray energy resolution of germanium is omitted. In Panel 1, the $\Delta\theta$ (red) and $\Delta\beta$ (black) components contribute to the total energy resolution (blue) via Eq. B.28. Panel 2 plots the total energy resolution from different $\Delta\theta$ contributions corresponding to the detector-target distances of the forward (red) and backward (blue) rings of SeGA. See text for details.

from the S800 target position. Panel 2 of Fig. B.1 compares the total gamma-ray energy resolution at two detector-target distances corresponding to the backward ring (23.3 cm and replotted in blue) and the forward ring (30.3 cm and plotted in red). Both curves have the same $\Delta\beta$ component, but the forward ring detectors are further from the target position; thus a single segment subtends an angle of 1.89° and $\Delta\theta$ is reduced.

The dashed traces in the bottom panel of Fig. B.1 at $\theta = 31.85°$ and $\theta = 140.25°$ (corresponding to the true SeGA ring angles as discussed within Subsect. 3.3.1) indicate that asymmetric placement of the rings with respect to the S800 target position results in a better energy resolution in the backward ring than the forward ring even though the opening angle of a single segment is larger in the backward ring. Using the estimates for $\Delta\theta$ and $\Delta\beta$ above, the energy resolution at FWHM in the forward and backward ring detectors are calculated to be 2.21% and 1.96%, respectively (*cf.* Subsect. 3.2.3).

The deviation of the measured gamma-ray energy from the true energy in the rest frame can also be quantified from Eq. B.27 with the first term instead corresponding to the uncertainty in the calibrated energy measurement of Doppler shifted gamma rays in the laboratory frame, ΔE. As before, this term can be safely neglected; the calibrated energies from ^{152}Eu and ^{226}Ra source data agree with the tabulated energies to better than 0.1%. Thus Eq. B.28 is used, but interpreted differently as $\Delta E'/E'$ is now taken to be the fractional uncertainty in the Doppler reconstructed gamma-ray energy as opposed to the energy resolution. Using $\Delta\theta$ and $\Delta\beta$ from above, the fractional uncertainties in the forward and backward rings are found to be 1.2% and 0.8%, respectively. The value of 1.2% has been adopted for quoting the uncertainty in Doppler reconstructed gamma-ray energies as the more conservative estimate.

Appendix C

Gamma-Ray Interactions with Matter

C.1 Interaction Mechanisms

There are three primary processes, hierarchically arranged by energy, by which a gamma ray interacts within a detector. For gamma-ray detection with high-purity germanium crystals, the end result of all three processes is a flow of charge carriers (electrons and holes) along an externally applied electric field that forms the output current pulse. The processes differ from one another in how the initial gamma-ray energy is transferred to the germanium semiconductor, promoting electrons from the valence band to the conduction band and creating electron-hole pairs. The three processes listed in order of importance as a function of increasing incident gamma-ray energy are: photoelectric absorption, Compton scattering, and pair production. To simplify the ensuing discussion, imagine all gamma-ray interactions occur in the center of a very large germanium detector such that all secondary photons are eventually detected. Hence, with the exception of electron binding energies, the total energy deposited in the detector is equal to the incident photon energy.[1]

---

[1] In reality, the finite detector size and/or interactions near the detector surface lead to gamma-ray spectrum features indicative of partial energy deposition, such as the continuum and edge of Compton scattering or the single and double escape peaks of pair production

C.1.1 Photoelectric Absorption

Photoelectric absorption is the process by which a low energy gamma ray (a few hundred keV) disappears in the vicinity of an atom. In its place, an atomic electron from a deeply bound orbital is ejected with energy

$$E_{e^-} = E_\gamma - E_b. \tag{C.1}$$

Here, the electron energy is slightly less than the initial photon energy by the binding energy of the electron's orbital shell. The kinetic energy of the ejected electron is then absorbed by the germanium detector by promoting valence electrons to the conduction band, resulting in a detectable current flow. The probability of photoelectric absorption is enhanced for absorber materials with high atomic numbers, as shown by the approximation adopted from Ref. [133]

$$P \propto \frac{Z^{4.5}}{E_\gamma^{3.5}}. \tag{C.2}$$

This probability decreases sharply as a function of increasing gamma-ray energy. The superiority of sodium iodide ($Z_I = 53$) over germanium ($Z_{Ge} = 32$) for the photoelectric absorption process is evident from this equation.[2]

In addition, the orbital shell vacancy of the photoelectron is quickly filled by another electron which radiates its excess energy via a characteristic X-ray. This X-ray usually undergoes photoelectric absorption as well, producing a second photoelectron such that, together with the original photoelectron, their summed kinetic energy closely approximates the incident

---

[132].

[2] For RDM lifetime measurements, the advantage of using germanium detectors rather than sodium iodide scintillators is their superior energy resolution for resolving the fast and slow photopeak components. With respect to the incident energy required to produce one information carrier—3 eV per electron-hole pair in Ge and 100 eV per photoelectron in NaI(Tl)—the statistical fluctuation of charge collection is greatly suppressed in high-purity germanium crystals.

gamma-ray energy. Note that this process of X-ray emission can continue iteratively or that instead of an X-ray, an Auger electron can be emitted.

C.1.2 Compton Scattering

For gamma-ray energies ranging from several hundred keV to several MeV, Compton scattering is the most probable interaction between a gamma ray and detector. For the presented spectroscopy of ^{18}C in Ch. 3, Compton scattering was the predominant effect. In this process, a gamma ray elastically scatters at an angle θ off an orbital electron in the detector and deposits a portion of its energy to the recoiling electron. Neglecting the electron binding energy and assuming the electron to be initially at rest with a rest mass energy of $m_0c^2 = 0.511$ MeV, the new photon energy, E'_γ, is given by

$$E'_\gamma = \frac{E_\gamma}{1 + \frac{E_\gamma}{m_0c^2}(1 - \cos(\theta))}. \tag{C.3}$$

The probability of Compton scattering increases with an increase in the number of available scattering electrons, but decreases with increasing incident gamma-ray energy according to the approximation [134]

$$P \propto \frac{Z}{E_\gamma}. \tag{C.4}$$

The Compton scattering process reduces the incident photon energy by transferring kinetic energy to the recoiling electron. This recoil electron then dissipates its energy in the germanium crystal lattice in the same manner as a photoelectron does. The scattered photon energy is either absorbed via photoelectric absorption or subsequent Compton scattering followed by photoelectric absorption.

C.1.3 Pair Production

Pair production can only occur in the Coulomb electric field of an atomic nucleus. In this process, the gamma ray disappears and in its place an electron-positron pair are produced. From energy considerations, the incident gamma-ray energy must be at minimum twice the rest mass of the electron, or 1.022 MeV. Pragmatically speaking, the probability for pair production is quite low until gamma-ray energies exceed several MeV. The gamma-ray energy in excess of 1.022 MeV is converted to the kinetic energy of the electron-positron pair. The electron loses its energy within the germanium crystal lattice as described for the photoelectric absorption process. The positron does as well; however as it slows, it eventually annihilates with an electron, producing a pair of 511 keV gamma rays. These gamma rays will either Compton scatter or undergo photoelectric absorption, and thus the full incident photon energy will be deposited within the detector. The probability of pair production increases dramatically with increasing gamma-ray energy and the square of the absorber atomic number.

C.2 Gamma-Ray Attenuation

Gamma-ray flux attenuation has a strong impact on the detection efficiency of an experimental setup. It occurs via absorption in experimental materials, such as the Köln/NSCL plunger target and degrader, the beam pipe, and the aluminum housing for the germanium crystals. The probability per unit length, σ, that a photon will be absorbed or scattered due to photoelectric absorption, Compton scattering, or pair production is simply the sum of the probability per unit length that any of those three processes will occur $(\sigma_{pe}, \sigma_{cs}, \sigma_{pp})$ and is given by

$$\sigma = \sigma_{pe} + \sigma_{cs} + \sigma_{pp}. \tag{C.5}$$

From the descriptions in Sect. C.1, the linear attenuation of gamma rays is clearly dependent upon the photon energy and the density of the absorbing material. It is therefore more common to characterize the probability of absorption per unit length by the mass attenuation coefficient, which is simply σ scaled by the absorber density ρ.

For a collimated beam of monoenergetic photons impinging upon an absorber en route to a detector, the rate of gamma-ray detection as a function of absorber thickness t, $N(t)$, will decrease exponentially according to

$$N(t) = N_0 e^{-\sigma t} = N_0 e^{-\frac{\sigma}{\rho}\rho t} \tag{C.6}$$

where N_0 is the gamma-ray detection rate in the absence of the absorber and the mass thickness, ρt, has been introduced. This is a convenient parameter; indeed materials used in the lab are often characterized by their mass thickness mg/cm^2.

Gamma ray attenuation is an important effect to consider in experiments where the integrated photopeak area is used to derive an experimental result such as a partial cross section. Hence, many tables and calculations exist that document the mass attenuation coefficient σ/ρ for pure elemental materials and common compounds over a wide range of photon energies (for example, Ref. [135] and references therein). Attenuation effects are also present in RDM lifetime measurements with the Köln/NSCL plunger. Since the analysis depends upon fitting the experimental photopeak intensity ratios with simulated lineshapes, it is imperative for the Geant4/ROOT simulation package to appropriately account for attenuation. This was verified by comparing the measured source photopeak efficiency curves to their simulated counterparts (see Fig. 2.12).

BIBLIOGRAPHY

BIBLIOGRAPHY

[1] B. A. Brown. The nuclear shell model towards the drip lines. *Prog. Part. Nucl. Phys.*, 47:517–599, 2001.

[2] M. Thoennessen. Reaching the limits of nuclear stability. *Rep. Prog. Phys.*, 67:1187–1232, 2004.

[3] Isotope Science Facility at Michigan State University: Upgrade of the NSCL rare isotope research capabilities. MSUCL-1345, November, 2006.

[4] P. D. Cottle and K. W. Kemper. Evolution of shell closures in neutron-rich $Z = 10-20$ nuclei. *Phys. Rev. C*, 66:061301, 2002.

[5] M. Stanoiu, D. Sohler, O. Sorlin, F. Azaiez, Zs. Dombrádi, B. A. Brown, M. Belleguic, C. Borcea, C. Bourgeois, Z. Dlouhy, Z. Elekes, Zs. Fülöp, S. Grévy, D. Guillemaud-Mueller, F. Ibrahim, A. Kerek, A. Krasznahorkay, M. Lewitowicz, S. M. Lukyanov, S. Mandal, J. Mrázek, F. Negoita, Yu.-E. Penionzhkevich, Zs. Podolyák, P. Roussel-Chomaz, M. G. Saint-Laurent, H. Savajols, G. Sletten, J. Timár, C. Timis, and A. Yamamoto. Disappearance of the $N = 14$ shell gap in the carbon isotopic chain. *Phys. Rev. C*, 78:034315, 2008.

[6] A. Ozawa, T. Kobayashi, T. Suzuki, K. Yoshida, and I. Tanihata. New Magic Number, $N = 16$, near the Neutron Drip Line. *Phys. Rev. Lett.*, 84:5493–5495, 2000.

[7] C. R. Hoffman, T. Baumann, D. Bazin, J. Brown, G. Christian, P. A. DeYoung, J. E. Finck, N. Frank, J. Hinnefeld, R. Howes, P. Mears, E. Mosby, S. Mosby, J. Reith, B. Rizzo, W. F. Rogers, G. Peaslee, W. A. Peters, A. Schiller, M. J. Scott, S. L. Tabor, M. Thoennessen, P. J. Voss, and T. Williams. Determination of the $N = 16$ Shell Closure at the Oxygen Drip Line. *Phys. Rev. Lett.*, 100:152502, 2008.

[8] R. B. Wiringa, V. G. J. Stoks, and R. Schiavilla. Accurate nucleon-nucleon potential with charge-independence breaking. *Phys. Rev. C*, 51:38–51, 1995.

[9] R. Machleidt. High-precision, charge-dependent Bonn nucleon-nucleon potential. *Phys. Rev. C*, 63:024001, 2001.

[10] E. Epelbaum, A. Nogga, W. Glöckle, H. Kamada, Ulf-G. Meißner, and H. Witała. Three-nucleon forces from chiral effective field theory. *Phys. Rev. C*, 66:064001, 2002.

[11] B. A. Brown and B. H. Wildenthal. Status of the Nuclear Shell Model. *Ann. Rev. of Nucl. Part. Sci.*, 38:29–66, 1988.

[12] P. Navrátil, J. P. Vary, and B. R. Barrett. Properties of ^{12}C in the *Ab Initio* Nuclear Shell Model. *Phys. Rev. Lett.*, 84:5728–5731, 2000.

[13] C. Forssén, J. P. Vary, E. Caurier, and P. Navrátil. Converging sequences in the *ab initio* no-core shell model. *Phys. Rev. C*, 77:024301, 2008.

[14] B. R. Barrett, B. Mihaila, S. C. Pieper, and R. B. Wiringa. *Ab Initio* Calculations of Light Nuclei. *Nucl. Phys. News*, 13:20–26, 2003.

[15] P. Navrátil. Private communication, 2011.

[16] R. Roth. Importance truncation for large-scale configuration interaction approaches. *Phys. Rev. C*, 79:064324, 2009.

[17] R. Roth and P. Navrátil. *Ab Initio* Study of ^{40}Ca with an Importance-Truncated No-Core Shell Model. *Phys. Rev. Lett.*, 99:092501, 2007.

[18] P. G. Hansen and J. A. Tostevin. Direct Reactions with Exotic Nuclei. *Annu. Rev. Nucl. Part. Sci.*, 53:219–261, 2003.

[19] J. A. Tostevin. Single-nucleon knockout reactions at fragmentation beam energies. *Nucl. Phys. A*, 682:320c–331c, 2001.

[20] A. Chester, P. Adrich, A. Becerril, D. Bazin, C. M. Campbell, J. M. Cook, D.-C. Dinca, W. F. Mueller, D. Miller, V. Moeller, R. P. Norris, M. Portillo, K. Starosta, A. Stolz, J. R. Terry, H. Zwahlen, C. Vaman, and A. Dewald. Application of the time-of-flight technique for lifetime measurements with relativistic beams of heavy nuclei. *Nucl. Instr. Meth. A*, 562:230–240, 2006.

[21] A. Dewald, K. Starosta, P. Petkov, M. Hackstein, W. Rother, P. Adrich, A. M. Amthor, T. Baumann, D. Bazin, M. Bowen, A. Chester, A. Dunomes, A. Gade, D. Galaviz, T. Glasmacher, T. Ginter, M. Hausmann, J. Jolie, B. Melon, D. Miller, V. Moeller, R. P. Norris, T. Pissulla, M. Portillo, Y. Shimbara, A. Stolz, C. Vaman, P. Voss, and D. Weisshaar. Collectivity of neutron-rich palladium isotopes and the valence proton symmetry. *Phys. Rev. C*, 78:051302, 2008.

[22] W. Rother, A. Dewald, H. Iwasaki, S. M. Lenzi, K. Starosta, D. Bazin, T. Baugher, B. A. Brown, H. L. Crawford, C. Fransen, A. Gade, T. N. Ginter, T. Glasmacher, G. F. Grinyer, M. Hackstein, G. Ilie, J. Jolie, S. McDaniel, D. Miller, P. Petkov, Th. Pissulla, A. Ratkiewicz, C. A. Ur, P. Voss, K. A. Walsh, D. Weisshaar, and K.-O. Zell. Enhanced Quadrupole Collectivity at $N = 40$: The Case of Neutron-Rich Fe Isotopes. *Phys. Rev. Lett.*, 106:022502, 2011.

[23] A. Gade and T. Glasmacher. In-beam nuclear spectroscopy of bound states with fast exotic ion beams. *Prog. Part. Nucl. Phys.*, 60:161–224, 2008.

[24] Aage Bohr and Ben R. Mottelson. *Nuclear Structure. Volume II. Nuclear Deformations.*, chapter 4. W. A. Benjamin, Inc., 1975.

[25] Jouni Suhonen. *From Nucleons to Nucleus: Concepts of Microscopic Nuclear Theory*, chapter 6. Springer, 1^{st} edition, 2007.

[26] S. Raman, C. W. Nestor Jr., and P. Tikkanen. Transition Probability from the Ground to the First-Excited 2^+ State of Even-Even Nuclides. *Atomic Data and Nuclear Data Tables*, 78:1–128, 2001.

[27] S. Raman, C. H. Malarkey, W. T. Milner, C. W. Nestor, and P. H. Stelson. Transition Probability, $B(E2)\uparrow$, from the Ground to the First-Excited 2^+ State of Even-Even Nuclides. *Atomic Data and Nuclear Data Tables*, 36:1–96, 1987.

[28] M. Wiedeking, P. Fallon, A. O. Macchiavelli, J. Gibelin, M. S. Basunia, R. M. Clark, M. Cromaz, M.-A. Deleplanque, S. Gros, H. B. Jeppesen, P. T. Lake, I.-Y. Lee, L. G. Moretto, J. Pavan, L. Phair, E. Rodriguez-Vietiez, L. A. Bernstein, D. L. Bleuel, J. T. Burke, S. R. Lesher, B. F. Lyles, and N. D. Scielzo. Lifetime Measurement of the First Excited 2^+ State in ^{16}C. *Phys. Rev. Lett.*, 100:152501, 2008.

[29] H. J. Ong, N. Imai, D. Suzuki, H. Iwasaki, H. Sakurai, T. K. Onishi, M. K. Suzuki, S. Ota, S. Takeuchi, T. Nakao, Y. Togano, Y. Kondo, N. Aoi, H. Baba, S. Bishop, Y. Ichikawa, M. Ishihara, T. Kubo, K. Kurita, T. Motobayashi, T. Nakamura, T. Okumura, and Y. Yanagisawa. Lifetime measurements of first excited states in ^{16,18}C. *Phys. Rev. C*, 78:014308, 2008.

[30] V. I. Goldansky. On Neutron-Deficient Isotopes of Light Nuclei and the Phenomena of Proton and Two-Proton Radioactivity. *Nucl. Phys.*, 19:482–495, 1960.

[31] B. J. Cole. Systematics of proton and diproton separation energies for light nuclei. *Phys. Rev. C*, 56:1866–1871, 1997.

[32] B. A. Brown, R. R. C. Clement, H. Schatz, A. Volya, and W. A. Richter. Proton drip-line calculations and the *rp* process. *Phys. Rev. C*, 65:045802, 2002.

[33] W. E. Ormand. Mapping the proton drip line up to $A = 70$. *Phys. Rev. C*, 55:2407–2417, 1997.

[34] M. Pfützner, E. Badura, C. Bingham, B. Blank, M. Chartier, H. Geissel, J. Giovinazzo, L. V. Grigorenko, R. Grzywacz, M. Hellström, Z. Janas, J. Kurcewicz, A. S. Lalleman, C. Mazzocchi, I. Mukha, G. Müzenberg, C. Plettner, E. Roeckl, K. P. Rykaczewski adn K. Schmidt, R. S. Simon, M. Stanoiu, and J.-C. Thomas. First evidence for the two-proton decay of ^{45}Fe. *Eur. Phys. J. A*, 14:279–285, 2002.

[35] J. Giovinazzo, B. Blank, M. Chartier, S. Czajkowski, A. Fleury, M. J. Lopez Jimenez, M. S. Pravikoff, J.-C. Thomas, F. de Oliveira Santos, M. Lewitowicz, V. Maslov, M. Stanoiu, R. Grzywacz, M. Pfützner, C. Borcea, and B. A. Brown. Two-Proton Radioactivity of ^{45}Fe. *Phys. Rev. Lett.*, 89:102501, 2002.

[36] K. Miernik, W. Dominik, Z. Janas, M. Pfützner, L Grigorenko, C. R. Bingham, H. Czyrkowski, M. Ćwiok, I. G. Darby, R. Dąbrowski, T. Ginter, R. Grzywacz, M. Karny adn A. Korgul, W. Kuśmierz, S. N. Liddick, M. Rajabali, K. Rykaczewski, and A. Stolz. Two-Proton Correlations in the Decay of ^{45}Fe. *Phys. Rev. Lett.*, 99:192501, 2007.

[37] B. Blank, A. Bey, G. Canchel, C. Dossat, A. Fleury, J.Giovinazzo, I. Matea, N. Adimi, F. De Oliveira, I. Stefan, G. Georgiev, S. Grévy, J. C. Thomas, C. Borcea, D. Cortina, M. Caamano, M. Stanoiu, F. Aksouh, B. A. Brown, F. C. Barker, and W. A. Richter. First Observation of ^{54}Zn and its Decay by Two-Proton Emission. *Phys. Rev. Lett.*, 94:232501, 2005.

[38] I. Mukha, K. Sümmerer, L. Acosta, M. A. G. Alvarez, E. Casarejos, A. Chatillon, D. Corina-Gil, J. Espino, A. Fomichev, J. E. García-Ramos, H. Geissel, J. Gómez-Camacho, L. Grigorenko, J. Hoffmann, O. Kiselev, A. Korsheninnikov, N. Kurz, Yu. Litvinov, I. Martel, C. Nociforo, W. Ott, M. Pfützner, C. Rodríguez-Tajes, E. Roeckl, M. Stanoiu, H. Weick, and P. J. Woods. Observation of Two-Proton Radioactivity of ^{19}Mg by Tracking the Decay Products. *Phys. Rev. Lett.*, 99:182501, 2007.

[39] L. V. Grigorenko, I. G. Mukha, and M. V. Zhukov. Prospective candidates for the two-proton decay studies I: structure and Coulomb energies of ^{17}Ne and ^{19}Mg. *Nucl. Phys. A*, 713:372–389, 2003.

[40] L. V. Grigorenko and M. V. Zhukov. Two-proton radioactivity and three-body decay. II. Exploratory studies of lifetimes and correlations. *Phys. Rev. C*, 68:054005, 2003.

[41] G. J. KeKelis, M. S. Zisman, D. K. Scott, R. Jahn, D. J. Vieira, Joseph Cerny, and F. Ajzenberg-Selove. Masses of the unbound nuclei ^{16}Ne, ^{15}F, and ^{12}O. *Phys. Rev. C*, 17:1929–1938, 1978.

[42] S. E. Woosley, A. Heger, and T. A. Weaver. The evolution and explosion of massive stars. *Rev. Mod. Phys.*, 74:1015–1071, 2002.

[43] Christian Iliadis. *Nuclear Physics of Stars*. Wiley-VCH Verlag GmbH & Co., 1st edition, 2007.

[44] E. M. Burbidge, G. R. Burbidge, W. A. Fowler, and F. Hoyle. Synthesis of the Elements in Stars. *Rev. Mod. Phys.*, 29:547–654, 1957.

[45] J. L. Fisker, R. D. Hoffman, and J. Pruet. On the Orgin of the Lightest Molybdenum Isotopes. *Astrophys. J.*, 690:135–139, 2008.

[46] C. Travaglio, R. Gallino, E. Arnone, J. Cowan, F. Jordan, and C. Sneden. Galactic Evolution of Sr, Y, and Zr: A Multiplicity of Nucleosynthetic Processes. *Astrophys. J.*, 601:864–884, 2004.

[47] C. Fröhlich, G. Martínez-Pinedo, M. Liebendörfer, F.-K. Thielemann, E. Bravo adn W.R. Hix, K. Langanke, and N. T. Zinner. Neutrino-Induced Nucleosynthesis of A $>$ 64 Nuclei: The νp Process. *Phys. Rev. Lett.*, 96:142502, 2006.

[48] R. K. Wallace and S. E. Woosley. Explosive Hydrogen Burning. *Astrophys. J. Suppl.*, 45:389–420, 1981.

[49] H. Schatz, A. Aprahamian, J. Görres, M. Wiescher, T. Rauscher, J. F. Rembges, F.-K. Thielemann, B. Pfeiffer, P. Möller, K.-L. Kratz, H. Herndl, B. A. Brown, and H. Rebel. rp-Process Nucleosynthesis at Extreme Temperature and Density Conditions. *Phys. Rep.*, 294:167–263, 1998.

[50] J. Görres, M. Wiescher, and F.-K. Thielemann. Bridging the waiting points: The role of two-proton capture reactions in the *rp* process. *Phys. Rev. C*, 51:392–400, 1995.

[51] H. Schatz, A. Aprahamian, V. Barnard, L. Bildsten, A. Cumming, M. Ouellette, T. Rauscher, F.-K. Thielemann, and M. Wiescher. End Point of the *rp* Process on Accreting Neutron Stars. *Phys. Rev. Lett.*, 86:3471–3474, 2001.

[52] J. Pruet, S. E. Woosley, R. Buras, H.-T. Janka, and R. D. Hoffman. Nucleosynthesis in the Hot Convective Bubble in Core-Collapse Supernovae. *Astrophys. J.*, 623:325–336, 2005.

[53] H. Schatz. The importance of nuclear masses in the astrophysical rp-process. *Int. J. Mass Spectrom.*, 251:293–299, 2006.

[54] Christian Iliadis. *Nuclear Physics of Stars*, chapter 3, page 162. Wiley-VCH Verlag GmbH & Co., 1^{st} edition, 2007.

[55] J. Savory, P. Schury, C. Bachelet, M. Block, G. Bollen, M. Facina, C. M. Folden, C. Guénaut, E. Kwan, A. A. Kwiatkowski, D. J. Morrissey, G. K. Pang, A. Prinke, R. Ringle, H. Schatz, S. Schwarz, and C. S. Sumithrarachchi. *rp* Process and Masses of $N \approx Z \approx 34$ Nuclides. *Phys. Rev. Lett.*, 102:132501, 2009.

[56] C. Weber, V.-V. Elomaa, R. Ferrer, C. Fröhlich, D. Ackermann, J. Äystö, G. Audi, L. Batist, K. Blaum, M. Block, A. Chaudhuri, M. Dworschak, S. Eliseev, T. Eronen, U. Hager, J. Hakala, F. Herfurth, F. P. Heßberger, G. Hofmann, A. Jokinen, A. Kankainen, H.-J. Kluge, K. Langanke, A. Martín, G. Martínez-Pinedo, M. Mazzocco, I. D. Moore, J. B. Neumayr, Yu. N. Novikov, H. Penttilä, W. R. Plaß, A. V. Popov, S. Rahaman, T. Rauscher, C. Rauth, J. Rissanen, D. Rodríguez, A. Saastamoinen, C. Scheidenberger, L. Schweikhard, D. M. Seliverstov, T. Sonoda, F.-K. Thielemann, P. G. Thirolf, and G. K. Vorobjev. Mass measurements in the vicinity of

the *rp*-process and the νp-process paths with the Penning trap facilities JYFLTRAP and SHIPTRAP. *Phys. Rev. C*, 78:054310, 2008.

[57] R. Pfaff, D. J. Morrissey, W. Benenson, M. Fauerbach, M. Hellström, C. F. Powell, B. M. Sherrill, M. Steiner, and J. A. Winger. Fragmentation of ^{78}Kr projectiles. *Phys. Rev. C*, 53:1753–1758, 1996.

[58] A. M. Rogers et al. Ground-state proton decay of ^{69}Br and implications for the ^{68}Se astrophysical rapid proton-capture process waiting point. *Phys. Rev. Lett.* Paper accepted for publication.

[59] W. Nazarewicz, J. Dobaczewski, T. R. Werner, J. A. Maruhn, P.-G. Reinhard, K. Rutz, C. R. Chinn, A. S. Umar, and M. R. Strayer. Structure of proton drip-line nuclei around doubly magic ^{48}Ni. *Phys. Rev. C*, 53:740–751, 1996.

[60] L. V. Grigorenko, R. C. Johnson, I. G. Mukha, I. J. Thompson, and M. V. Zhukov. Theory of Two-Proton Radioactivity with Application to ^{19}Mg and ^{48}Ni. *Phys. Rev. Lett.*, 85:22–25, 2000.

[61] P. J. Woods and C. N. Davids. Nuclei Beyond the Proton Drip-Line. *Annu. Rev. Nucl. Part. Sci.*, 47:541–590, 1997.

[62] I. Mukha and E. Roeckl and L. Batist and A. Blazhev and J. Döring and H. Grawe and L. Grigorenko and M. Huyse and Z. Janas and R. Kirchner and M. La Commara and C. Mazzocchi and S. L. Tabor and P. Van Duppen. Proton-proton correlations observed in two-proton radioactivity of ^{94}Ag. *Nature*, 439:298–302, 2006.

[63] M. A. Famiano, T. Liu, W. G. Lynch, M. Mocko, A. M. Rogers, M. B. Tsang, M. S. Wallace, R. J. Charity, S. Komarov, D. G. Sarantites, L. G. Sobotka, and G. Verde. Neutron and Proton Transverse Emission Ratio Measurements and the Density Dependence of the Asymmetry Term of the Nuclear Equation of State. *Phys. Rev. Lett.*, 97:052701, 2006.

[64] T. Baumann, A. M. Amthor, D. Bazin, B. A. Brown, C. M. Folden III, A. Gade, T. N. Ginter, M. Hausmann, M. Matoš, D. J. Morrissey, M. Portillo, A. Schiller, B. M. Sherrill, A. Stolz, O. B. Tarasov, and M. Thoennessen. Discovery of ^{40}Mg and ^{42}Al suggests neutron drip-line slant towards heavier isotopes. *Nature*, 449:1022–1024, 2007.

[65] H. Geissel, G. Münzenberg, and K. Riisager. Secondary Exotic Nuclear Beams. *Annu. Rev. Nucl. Part. Sci.*, 45:163–203, 1995.

[66] W. F. Mueller, J. A. Church, T. Glasmacher, D. Gutknecht, G. Hackman, P. G. Hansen, Z. Hu, K. L. Miller, and P. Quirin. Thirty-two fold segmented germanium detectors to identify γ-rays from intermediate-energy exotic beams. *Nucl. Instr. Meth. A*, 466:492–498, 2001.

[67] D. J. Morrissey. The COUPLED CYCLOTRON PROJECT at the NSCL. *Nucl. Phys. A*, 616:45c–55c, 1997.

[68] S. Gammino, G. Ciavola, T. Antaya, and K. Harrison. Volume scaling and magnetic field scaling on SC-ECRIS at MSU-NSCL. *Rev. Sci. Instrum.*, 67:155–160, 1996.

[69] H. Koivisto, D. Cole, A. Fredell, C. Lyneis, P. Miller, J. Moskalik, B. Nurnberger, and J. Ottarson. In *Proceedings of the Workshop on the Production of Intense Beams of Highly Charged Ions*, volume 72, page 83, 2000.

[70] P. A. Zavodszky, B. Arend, D. Cole, J. DeKamp, G. Machicoane, F. Marti, P. Miller, J. Moskalik, J. Ottarson, J. Vincent, and A. Zeller. Design of SuSI- Superconducting Source for Ions at NSCL/MSU- I. The Magnet System. In M. Leitner, editor, *Electron Cyclotron Resonance Ion Sources- 16th International Workshop on ECR Ion Sources*, pages 131–135, 2005.

[71] P. A. Zavodszky, B. Arend, D. Cole, J. DeKamp, G. Machicoane, F. Marti, P. Miller, J. Moskalik, J. Ottarson, J. Vincent, and A. Zeller. Design of SuSI- superconducting source for ions at NSCL/MSU- II. The conventional parts. *Nucl. Instr. Meth. B*, 241:959–964, 2005.

[72] D. J. Morrissey, B. M. Sherrill, M. Steiner, A. Stolz, and I. Wiedenhover. Commissioning the A1900 projectile fragment separator. *Nucl. Instr. Meth. B*, 204:90–96, 2003.

[73] J. P. Dufour, R. Del Moral, H. Emmermann, F. Hubert, D. Jean, C. Poinot, M. S. Pravikoff, A. Fleury, H. Delagrange, and K.-H. Schmidt. Projectile fragments isotopic separation: Application to the lise spectrometer at GANIL. *Nucl. Instr. Meth. A*, 248:267–281, 1986.

[74] Glenn F. Knoll. *Radiation Detection and Measurement*, chapter 2, page 31. John Wiley & Sons, Inc., 3$^{\text{rd}}$ edition, 1999.

[75] A. Dewald, B. Melon, O. Möller, J. Jolie, C. Fransen, K. Jessen, K.-O. Zell, and K. Starosta. A Plunger Apparatus for Relativistic Radioactive Beams. *GSI Scientific Report 2005*, page 38, 2006.

[76] D. Bazin, J. A. Caggiano, B. M. Sherrill, J. Yurkon, and A. Zeller. The S800 spectrograph. *Nucl. Instr. Meth. B*, 204:629–633, 2003.

[77] R. Krücken. Precision Lifetime Measurements Using the Recoil Distance Method. *J. Res. Natl. Inst. Stand. Technol.*, 105:53–60, 2000.

[78] K. Starosta, A. Dewald, A. Dunomes, P. Adrich, A. M. Amthor, T. Baumann, D. Bazin, M. Bowen, B. A. Brown, A. Chester, A. Gade, D. Galaviz, T. Glasmacher, T. Ginter,

M. Hausmann, M. Horoi, J. Jolie, B. Melon, D. Miller, V. Moeller, R. P. Norris, T. Pissulla, M. Portillo, W. Rother, Y. Shimbara, A. Stolz, C. Vaman, P. Voss, D. Weisshaar, and V. Zelevinsky. Shape and Structure of $N = Z$ ^{64}Ge: Electromagnetic Transition Rates from the Application of the Recoil Distance Method to a Knockout Reaction. *Phys. Rev. Lett.*, 99:042503, 2007.

[79] M. Petri, P. Fallon, A. O. Macchiavelli, S. Paschalis, K. Starosta, T. Baugher, D. Bazin, L. Cartegni, R. M. Clark, H. L. Crawford, M. Cromaz, A. Dewald, A. Gade, G. F. Grinyer, S. Gros, M. Hackstein, H. B. Jeppesen, I. Y. Lee, S. McDaniel, D. Miller, M. M. Rajabali, A. Ratkiewicz, W. Rother, P. Voss, K. A. Walsh, D. Weisshaar, M. Wiedeking, and B. A. Brown. Lifetime Measurement of the 2_1^+ state in ^{20}C. Manuscript submitted for publication.

[80] P. F. Hinrichsen, D. W. Hetherington, S. C. Gujrathi, and L. Cliche. Heavy-ion energy resolution of SSB detectors. *Nucl. Instr. Meth. B*, 45:275–280, 1990.

[81] E. D. Klema, J. X. Saladin, J. G. Alessi, and H. W. Schmitt. Energy Resolution of Silicon Surface-Barrier Detectors for Alpha Particles, Oxygen Ions, and Fission Fragments. *Nucl. Instr. Meth.*, 178:383–393, 1980.

[82] J. Yurkon, D. Bazin, W. Benenson, D. J. Morrissey, B. M. Sherrill, D. Swan, and R. Swanson. Focal plane detector for the S800 high-resolution spectrometer. *Nucl. Instr. Meth. A*, 422:291–295, 1999.

[83] M. Berz, K. Joh, J. A. Nolen, B. M. Sherrill, and A. F. Zeller. Reconstructive correction of aberrations in nuclear particle spectrographs. *Phys. Rev. C*, 47:537–544, 1993.

[84] O. Wieland, F. Camera, B. Million, A. Bracco, and J. van der Marel. Pulse distributions and tracking in segmented detectors. *Nucl. Instr. Meth. A*, 487:441–449, 2002.

[85] J. R. Terry. *Probing Single-Particle Structure Near the Island of Inversion by Direct Neutron Knockout from Intermediate-Energy Beams of* ^{26,28}*Ne and* ^{30,32}*Mg.* PhD thesis, Michigan State University, 2006.

[86] D. Miller. *Intermediate-Energy Proton Knockout to Probe Single-Particle Structure and Nuclear Spin Alignment in the "Island of Inversion" Isotopes* ^{31,33}*Mg.* PhD thesis, Michigan State University, 2009.

[87] J. B. Stoker. *β-Decay Half-Life of the* rp-*Process Waiting-Point Nuclide* ^{84}*Mo.* PhD thesis, Michigan State University, 2009.

[88] K. Starosta, C. Vaman, D. Miller, P. Voss, D. Bazin, T. Glasmacher, H. Crawford, P. Mantica, H. Tan, W. Hennig, M. Walby, A. Fallu-Labruyere, J. Harris, D. Breus, P. Grudberg, and W. K. Warburton. Digital Data Acquisition System for experiments with segmented detectors at National Superconducting Cyclotron Laboratory. *Nucl. Instr. Meth. A*, 610:700–709, 2009.

[89] International Atomic Energy Agency. IAEA Gamma-ray Decay Data. http://www-nds.iaea.org/xgamma_standards/genergies1.htm.

[90] H. Tan, W. Hennig, M. Walby, A. Fallu-Labruyere, J. Harris, D. Breus, P. Grudberg, W. K. Warburton, C. Vaman, T. Glasmacher, P. Mantica, D. Miller, K. Starosta, and P. Voss. Digital Data Acquisition Modules for Instrumenting Large Segmented Germanium Detector Arrays. In *IEEE Nuclear Science Symposium Conference Record*, pages 3196–3200, 2008.

[91] R. Brun and F. Rademakers. ROOT- An object oriented data analysis framework. *Nucl. Instr. Meth. A*, 389:81–86, 1997.

[92] D. Radford. Radware homepage. http://radware.phy.ornl.gov/main.html.

[93] S. Agostinelli, J. Allison, K. Amako, J. Apostolakis, H. Araujo, P. Arce, M. Asai, D. Axen, S. Banerjee, G. Barrand, et al. GEANT4- a simulation toolkit. *Nucl. Instr. Meth. A*, 506:250–303, 2003.

[94] P. Adrich, D. Enderich, D. Miller, V. Moeller, R. P. Norris, K. Starosta, C. Vaman, P. Voss, and A. Dewald. A simulation tool for the Recoil Distance Method lifetime measurements at NSCL. *Nucl. Instr. Meth. A*, 598:454–464, 2009.

[95] O. B. Tarasov and D. Bazin. LISE++: Radioactive beam production with in-flight separators. *Nucl. Instr. Meth. B*, 266:4657–4664, 2008.

[96] M. Stanoiu, F. Azaiez, Zs. Dombrádi, O. Sorlin, B. A. Brown, M. Belleguic, D. Sohler, M. G. Saint Laurent, Y. E. Penionzhkevich, G. Sletten, C. Borcea, C. Bourgeois, A. Bracco, J. M. Daugas, Z. Dlouhý, C. Donzaud, Zs. Fülöp, D. Guillemaud-Mueller, S. Grévy, F. Ibrahim, A. Kerek, A. Krasznahorkay, M. Lewitowicz, S. Lukyanov, P. Mayet, S. Mandal, W. Mittig, J. Mrázek, F. Negoita, F. De Oliveira-Santos, Zs. Podolyák, F. Pougheon, P. Roussel-Chomaz, H. Savajols, Y. Sobolev, C. Stodel, J. Timár, and A. Yamamoto. Disappearance of the $N = 14$ shell gap in the carbon isotopic chain. *Nucl. Phys. A*, 746:135c–139c, 2004.

[97] L. K. Fifield, J. L. Durell, M. A. C. Hotchkis, J. R. Leigh, T. R. Ophel, and D. C. Weisser. The Mass of ^{18}C From a Heavy Ion Double-Charge-Exchange Reaction. *Nucl. Phys. A*, 385:505–515, 1982.

[98] Philip R. Bevington and D. Keith Robinson. *Data Reduction and Error Analysis for the Physical Sciences*, chapter 8, page 146. McGraw-Hill Higher Education, 3$^{\text{rd}}$ edition, 2003.

[99] E. Steinbauer, P. Bauer, M. Geretschläger, G. Bortels, J. P. Biersack, and P. Burger. Energy resolution of silicon detectors: approaching the physical limit. *Nucl. Instr. Meth. B*, 85:642–649, 1994.

[100] T. Maisch, R. Günzler, M. Weiser, S. Kalbitzer, W. Welser, and J. Kemmer. Ion-Implanted Si pn-Junction Detectors with Ultrathin Windows. *Nucl. Instr. Meth. A*, 288:19–23, 1990.

[101] J. C. Overley and H. W. Lefevre. Precision in Neon Ion Energy Loss Measurements With a Silicon Surface Barrier Detector. *Nucl. Instr. Meth. B*, 10/11:237–240, 1985.

[102] W. T. Milner. Oak Ridge National Laboratory DAMM Help File. http://www.phy.anl.gov/gammasphere/doc/damm.txt.

[103] G. Bortels and P. Collaers. Analytical function for fitting peaks in alpha-particle spectra from Si detectors. *Int. J. Radiat. Appl. Instrum. Part A*, 38(10):831–837, 1987.

[104] W. Benenson, A. Guichard, E. Kashy, D. Mueller, H. Nann, and L. W. Robinson. Mass Measurements of ^{19}Na and ^{23}Al Using the (^{3}He, ^{8}Li)Reaction. *Phys. Lett. B*, 58:46–48, 1975.

[105] F. de Oliveira Santos, P. Himpe, M. Lewitowicz, I. Stefan, N. Smirnova, N. L. Achouri, J. C. Angélique, C. Angulo, L. Axelsson, D. Baiborodin, F. Becker, M. Bellegui, E. Berthoumieux, B. Blank, C. Borcea, A. Cassimi, J. M. Daugas, G. de France, F. Dembinski, C. E. Demonchy, Z. Dlouhy, P. Dolégiéviez, C. Donzaud, G. Georgiev, L. Giot, S. Grévy, D. Guillemaud Mueller, V. Lapoux, E. Liénard, M. J. Lopez Jimenez, K. Markenroth, I. Matea, W. Mittig, F. Negoita, G. Neyens, N. Orr, F. Pougheon, P. Roussel Chomaz, M. G. Saint Laurent, F. Sarazin, H. Savajols, M. Sawicka, O. Sorlin, M. Stanoiu, C. Stodel, G. Thiamova, D. Verney, and A. C. C. Villari. Study of ^{19}Na at SPIRAL. *Eur. Phys. J. A*, 24:237–247, 2005.

[106] K. Sümmerer and B. Blank. Modified empirical parametrization of fragmentation cross sections. *Phys. Rev. C*, 61:034607, 2000.

[107] O. B. Tarasov and D. Bazin. Development of the program LISE: application to fusion-evaporation. *Nucl. Instr. Meth. B*, 204:174–178, 2003.

[108] J.-J. Gaimard and K.-H. Schmidt. A reexamination of the abrasion-ablation model for the description of the nuclear fragmentation reaction. *Nucl. Phys. A*, 531:709–745, 1991.

[109] J. Tostevin. Private communication, 2010.

[110] D. Miller, P. Adrich, B. A. Brown, V. Moeller, A. Ratkiewicz, W. Rother, K. Starosta, J. A. Tostevin, C. Vaman, and P. Voss. Intermediate energy proton knockout to the “island of inversion” isotope ^{31}Mg. *Phys. Rev. C*, 79:054306, 2009.

[111] E. K. Warburton and B. A. Brown. Effective interactions for the $0p1sd$ nuclear shell-model space. *Phys. Rev. C*, 46:923–944, 1992.

[112] D. P. Balamuth, J. M. Lind, K. C. Young, and R. W. Zurmühle. Angular correlation study of levels in ^{16}C. *Nucl. Phys. A*, 290:65–71, 1977.

[113] Y. Kanada-En'yo. Deformation of C isotopes. *Phys. Rev. C*, 71:014310, 2005.

[114] Aage Bohr and Ben R. Mottelson. *Nuclear Structure. Volume II. Nuclear Deformations*, chapter 3. W. A. Benjamin, Inc., 1975.

[115] T. Nakamura, N. Fukuda, T. Kobayashi, N. Aoi, H. Iwasaki, T. Kubo, A. Mengoni, M. Notani, H. Otsu, H. Sakurai, S. Shimoura, T. Teranishi, Y. X. Watanabe, K. Yoneda, and M. Ishihara. Coulomb Dissociation of ^{19}C and its Halo Structure. *Phys. Rev. Lett.*, 83:1112–1115, 1999.

[116] D. Bazin, B. A. Brown, J. Brown, M. Fauerbach, M. Hellström, S. E. Hirzebruch, J. H. Kelley, R. A. Kryger, D. J. Morrissey, R. Pfaff, C. F. Powell, B. M. Sherrill, and M. Thoennessen. One-Neutron Halo of ^{19}C. *Phys. Rev. Lett.*, 74:3569–3572, 1995.

[117] Takaharu Otsuka, Toshio Suzuki, Rintaro Fujimoto, Hubert Grawe, and Yoshinori Akaishi. Evolution of Nuclear Shells due to the Tensor Force. *Phys. Rev. Lett.*, 95:232502, 2005.

[118] H. Sagawa, X. R. Zhou, X. Z. Zhang, and Toshio Suzuki. Deformations and electromagnetic moments in carbon and neon isotopes. *Phys. Rev. C*, 70:054316, 2004.

[119] E. Caurier, G. Martínez-Pinedo, F. Nowacki, A. Poves, and A. P. Zuker. The shell model as a unified view of nuclear structure. *Rev. Mod. Phys.*, 77:427–488, 2005.

[120] P. Doleschall. Influence of the short range nonlocal nucleon-nucleon interaction on the elastic $n - d$ scattering: Below 30 MeV. *Phys. Rev. C*, 69:054001, 2004.

[121] J. Simpson, J. Nyberg, W. Korten, et al. AGATA: Advanced Gamma Tracking Array Technical Design Report. 2008.

[122] I.-Y. Lee, J. T. Anderson, J. Bercovitz, A. Biocca, J. Comins, M. Cromaz, M. Descovich, D. Doering, P. Fallon, J. M. Joseph, C. Larsen, C. Lionberger, T. Loew, A. O. Macchiavelli, J. Pavan, D. Peterson, D. Radford, B. A. Savnik, C. Timossi, S. Virostek, H. Yaver, , and S. Zimmermann. The Future of Gamma-Ray Spectroscopy: GRETA, The Gamma-Ray Energy Tracking Array. Contribution to the NSAC Long-Range Plan, 2006.

[123] D. Weisshaar. GRETINA Service Level Description. NSCL, 2011.

[124] I. Y. Lee. Gamma-ray tracking detectors. *Nucl. Instr. Meth. A*, 422:195, 1999.

[125] M. Descovich, I. Y. Lee, P. Fallon, M. Cromaz, A. O. Macchiavelli, D. C. Radford, K. Vetter, R. M. Clark, M. A. Deleplanque, F. S. Stephens, and D. Ward. In-beam measurement of the position resolution of a highly segmented coaxial germanium detector. *Nucl. Instr. Meth. A*, 553:535–542, 2005.

[126] H. Iwasaki. Private communication, 2011.

[127] I. Mukha, L. Grigorenko, K. Sümmerer, L. Acosta, M. A. G. Alvarez, E. Casarejos, A. Chatillon, D. Cortina-Gil, J. M. Espino, A. Fomichev, J. E. García-Ramos, H. Geissel, J. Gómez-Camacho, J. Hofmann, O. Kiselev, A. Korsheninnikov, N. Kurz, Yu. Litvinov, I. Martel, C. Nociforo, W. Ott, M. Pfützner, C. Rodríguez-Tajes, E. Roeckl, M. Stanoiu, H. Weick, and P. J. Woods. Proton-proton correlations observed in two-proton decay of ^{19}Mg and ^{16}Ne. *Phys. Rev. C*, 77:061303, 2008.

[128] I. Mukha, K. Sümmerer, L. Acosta, M. A. G. Alvarez, E. Casarejos, A. Chatillon, D. Cortina-Gil, I. A. Egorova, J. M. Espino, A. Fomichev, J. E. García-Ramos, H. Geissel, J. Gómez-Camacho, L. Grigorenko, J. Hofmann, O. Kiselev, A. Korsheninnikov, N. Kurz, Yu. A. Litvinov, E. Litvinova, I. Martel, C. Nociforo, W. Ott, M. Pfützner, C. Rodríguez-Tajes, E. Roeckl, M. Stanoiu, N. K. Timofeyuk, H. Weick, and P. J. Woods. Spectroscopy of proton-unbound nuclei by tracking their decay products in-flight: One- and two- proton decays of ^{15}F, ^{16}Ne, and ^{19}Na. *Phys. Rev. C*, 82:054315, 2010.

[129] M.S. Wallace, M.A. Famiano, M.-J. van Goethem, A.M. Rogers, W.G. Lynch, J. Clifford, F. Delaunay, J. Lee, S. Labostov, M. Mocko, L. Morris, A. Moroni, B.E. Nett, D.J. Oostdyk, R. Krishnasamy, M.B. Tsang, R.T. de Souza, S. Hudan, L.G. Sobotka, R.J. Charity, J. Elson, and G.L. Engel. The high resolution array (HiRA) for rare isotope beam experiments. *Nucl. Instr. Meth. A*, 583:302–312, 2007.

[130] S. Wilburn, Micron Semiconductor Ltd. Private communication, 2010.

[131] Kenneth S. Krane. *Introductory Nuclear Physics*, chapter 5, page 136. John Wiley & Sons, Inc., 1st edition, 1987.

[132] Kenneth S. Krane. *Introductory Nuclear Physics*, chapter 7, pages 220–222. John Wiley & Sons, Inc., 1st edition, 1987.

[133] Glenn F. Knoll. *Radiation Detection and Measurement*, chapter 2, page 49. John Wiley & Sons, Inc., 3rd edition, 1999.

[134] Christian Iliadis. *Nuclear Physics of Stars*, chapter 4, page 239. Wiley-VCH Verlag GmbH & Co., 1st edition, 2007.

[135] S. M. Seltzer. Calculation of Photon Mass Energy-Transfer and Mass Energy-Absorption Coefficients. *Radiat. Res.*, 136:147–170, 1993.